Hydroelastic Analysis of a Multi-Module Very Large Floating Structure

MSc Thesis

D.C.M.Y. (Dorette) Regout

Faculty of Civil Engineering and Geosciences

October 2021

TU Delft Delft University of Technology

blue21

Department of Hydraulic Engineering October 22, 2021

Master Thesis

Hydroelastic Analysis of a Multi-Module Very Large Floating Structure

written by

D.C.M.Y. Regout

in fulfillment of the requirements for the degree of

Master of Science

Department of Hydraulic Engineering
Faculty of Civil Engineering and Geosciences
Delft University of Technology

to be defended publicly on Friday October 29, 2021 at 15:45 PM.

Student number:	4400011	
Thesis committee:	Dr. ir. J.O. Colomés Gené	TU Delft, chair
	Dr. ir. K.N. van Dalen	TU Delft
	Dr. ir. R.J. Labeur	TU Delft
	Dr. ir. A. Antonini	TU Delft
	Dr. ir. R.P.F. Gomes	Blue21

An electronic version of this thesis is available at `http://repository.tudelft.nl/`.

October 22, 2021

TU Delft Delft University of Technology

blue21

Abstract

Due to the increasing population growth and the impacts of climate change, many of the world's largest cities are now facing great challenges regarding land scarcity and flood risk, as they are built close to water and coastal regions. To cope with these global problems, floating urbanization may provide a viable solution and the attention to this concept has therefore grown considerably in the last decades. Previous (experimental) studies on preliminary designs of multi-module Very Large Floating Structures (VLFSs) demonstrated that these systems contain strong hydrodynamic and mechanical coupling. This implies that there is a significant relation between the response of the system, the stiffness of the modules and connections, and the incident wave lengths, indicating that the VLFS response can be altered by adjusting the material properties and its dimensions.

When looking at the Fluid-Structure Interaction (FSI) of these systems, considerations regarding hydroelasticity play an important role. This is due to the coupled effects of the wave dynamics and the structural deformations, in combination with the potentially large horizontal dimensions. To improve the design of a VLFS, the motion response and the structural performance has to be analysed, where minimal vertical displacements are desired, while the maximum occurring bending moments are limited. Therefore, the aim of the study is to investigate the influence of various module and connection stiffness on the behaviour of the system, with the view to obtain more insight in the complex relation between the hydroelastic response and internal loads, when the system is subject to regular waves.

To this end, a hydroelastic analysis of a multi-module VLFS is performed, where the problem is analysed in the frequency domain. Accordingly, the fluid-structure interaction is described by a 2D model, where the VLFS is represented by four floating beams interconnected with rotational springs. The fluid is modelled as an ideal fluid, for which the linear wave theory is applied. The floating beams are modelled by the Euler-Bernoulli beam theory. The finite element method is used to solve the governing equations of the fluid motion and the motion of the beams, where the model is built using the FE library Gridap, written in the Julia programming language. Ultimately, results are obtained regarding the vertical displacements and moment distributions along the structure, for different combinations of the beam/connection stiffness (i.e. flexible, semi-rigid and rigid), and different wavelengths. Moreover, the maximum vertical displacement and maximum bending moment are computed for the varying combinations of the two stiffness quantities, visualized by means of contour plots.

The numerical results show that for increasing rotational connection stiffness, the VLFS approaches the response of a continuous system. The maximum displacement is reduced by increasing the bending stiffness of the modules, but this will increase the bending moments simultaneously. Depending on the material properties and the incident wave length, the structural behaviour shifts from rigid modules to a more continuous system. Since some cases even result in a combination of both rigid and flexible behaviour in the structure, excluding elasticity from the analysis may lead to inaccurate results.
Because the influence of different combinations of the two stiffness quantities on the hydroelastic response is non-linear, obtaining information by means of the contour plots will give valuable insight in the most optimal combinations with regard to the stiffness quantities, and the trade-off between minimal displacements and maximum bending moments that occur.

As the numerical model is highly adaptable and copes well for different input parameters, the results can also be obtained for more complex (wave) conditions, such as irregular waves, or including seabed topography. The model creates therefore an opportunity to easily analyse a large variety of model setups, in a relatively short amount of time.

Preface

This thesis marks the final assessment in the fulfillment of my master degree in Hydraulic Engineering. As a student at the TU Delft, I was able to combine my love for physics, and mathematics together with a creative approach in thinking about new ways how to give form to the future. This has encouraged me to really think about the type of engineer I want to become and to figure out in which field I want to be involved throughout my career. As a result, I developed a strong interest in the dynamics of fluid-structure interactions and I felt lucky that I had a change to graduate on this subject.

Of course, this graduation project would not have been possible without the help of a lot of people. First of all, I would like to thank my chair, Oriol Colomés, for his ongoing enthusiasm, helpfulness, and patience in teaching me all the magic of computational modelling and Gridap. Working together made me more and more passionate about all the new things I could learn, which kept me motivated throughout the project. Furthermore, I would like to thank the other committee members: Rui Gomes for his valuable assistance and positive feedback, and Karel van Dalen for his expertise and great way of transferring knowledge. His lectures during my bachelor were the first to spark my enthusiasm for dynamics of systems, where they have laid a good foundation for the competencies needed in further dynamics courses and for this thesis.

Thank you, Alessandro Antonini, for your time to replace Robert Jan Labeur as a committee member at the last moment. Unfortunately, Robert Jan had to step back as chair in the final month, but he has been of great supervision for the majority of the project. Our shared enthusiasm and interest in the subject (and jazz music) set off a great collaboration from the start and gave me the confidence that I was able to successfully complete this assessment. My entire committee has always been very supportive and involved. This created an environment for me where I felt comfortable reaching out to them if I had any questions or struggles. I therefore enjoyed the whole project, as this guidance encouraged me to step out of my comfort zone and challenge myself because I never felt like I was on my own.

I also want to thank William Otto from MARIN, who took the time to brainstorm with me about the subject. His experimental expertise on the topic was of great assistance in helping me to formulate the appropriate research approach.

I would like to finish this acknowledgment by giving a special shout-out to my friends and family. Their unconditional love and support, as they coped with all my ups and downs during the past 11 months and throughout my college career, have helped me overcome insecurities and grow on a personal level, allowing me to get the most out of my years as a student.

I hope you will enjoy reading with thesis!

Dorette Regout
The Hague, October 2021

Table of Content

List of Figures

List of Tables

List of Abbreviations

1D	One-Dimensional
2D	Two-Dimensional
3D	Three-Dimensional
BC	Boundary Condition
BEM	Boundary Element Method
CG	Continuous Galerkin approach
DG	Discontinuous Galerkin approach
DoF	Degree of Freedom
EoM	Equation of Motion
FDM	Finite Difference Method
FE	Finite Element
FEM	Finite Element Method
FSI	Fluid-Structure Interaction
IC	Interface Condition
MARIN	Maritime Research Institute Netherlands
MFS	Modular Floating Structure
PDE	Partial Differential Equation
PFS	Pontoon-like Floating Structure
VLFS	Very Large Floating Structure

List of Symbols

α	wavelength-to-beam-length ratio
α_f	fluid stability parameter
α_{b1}	mass of structure over water density
α_{b2}	bending stiffness of structure over water density
β	connection location parameter
β_h	general stability parameter
η	water surface elevation
η^*	reference surface elevation of undisturbed wave
η_{inc}	surface elevation of incident wave
Γ_b	boundary at the seabed
$\Gamma_{-\infty}$	vertical boundary on the left side of fluid domain
γ_1	bending stiffness parameter
Γ_∞	vertical boundary on the right side of fluid domain
Γ_{fs}	boundary at the free surface
Γ_L	boundary on the left side of numerical domain
γ_m	order stability parameter
Γ_R	boundary on the right side of numerical domain
Γ_{str}	boundary at the fluid-structure interface
$\hat{u}_i$	displacement at node i of finite element
λ	incident wave length
Λ_j	interior facets at connections
Λ_{str}	interior facets of structure
μ_0	damping factor
μ_1	damping coefficient
μ_2	damping coefficient
∇	Nabla operator
$\nabla^2 = \Delta$	Laplace operator
Ω	fluid domain

ω	incident wave frequency
ω_0	natural frequency
ϕ	flow velocity potential
ϕ^*	reference flow velocity potential of undisturbed wave
ϕ_{inc}	flow velocity potential of incident wave
π	pi
ρ_b	mass density of the structure
ρ_w	water density
$\vec{n}$	normal unit vector
ξ	rotational stiffness parameter
A_w	wave amplitude
d	water depth
E	Young's modulus
EI	bending stiffness of the structure
g	gravitational constant
H	wave height
h	length finite element
h_b	height of the structure
I	second moment of inertia
i	imaginary number
k	wave number
k_r	rotational stiffness of the connection
L	length of the structure
l	length fluid domain ext. damping zones
L_d	length of the damping zone
M	bending moment
p	water pressure
T	wave period
t	time
u_x	flow velocity in x-direction
u_z	flow velocity in z-direction
w	vertical displacement of the structure
x	x-coordinate
x_d	x-coordinate start damping zone
z	z-coordinate

1 Introduction to Floating Cities & Very Large Floating Structures

As most of the world's largest urban areas are built close to water and coastal regions, many of these cities are facing great challenges regarding flood risk, together with increasing land scarcity due to fast growing populations and urbanisation. Due to the effects of global warming, the mean sea level is rising and - even when taking immediate action - it is evident that for many cities, islands, and coastal areas around the world this will have severe consequences. In order to cope with these global problems, new technologies have therefore been introduced in recent decades to provide solutions to land scarcity and flood risks.

Land reclamation techniques are currently the most widely used application to artificially create new land. However, these techniques can have large negative impacts on the (local) environment and biodiversity [1]. Furthermore, its construction is limited to only shallow water depths and requires huge amounts of sand and other building materials. When using mainly land reclamation to deal with these global issues, ultimately, solving one scarcity problem by creating another does not seem to provide a sustainable solution for the future [2]. That is why attention to the concept of floating cities has grown enormously, where it recently has been adopted by the United Nations as a viable alternative to land reclamation during the 2019 Climate Change Roundtable [3].

1.1 Realisation of Floating Cities

Parties involved in the research and development of floating cities strongly advocate the important opportunities that floating urbanization can offer in the future. When current cities are expanded even further on land, this in turn comes at the expense of land that is also needed for other activities such as agriculture. On the contrary, with floating urbanization, the availability of land will actually increase and can therefore really offer a solution to the problem of land scarcity, instead of just relocating it [2].

Another big advantage of floating cities is related to its floating behaviour and modular characteristics. Consequently, this new form of urban areas is highly adaptable which will reduce the probability of flood risk and therefore will serve as a great solution with respect to problems related to climate change and sea-level rise.

In addition to providing new living space and offering a solution against flood risk, the development of floating cities also allows to completely rethink the way cities are built. Considering these cities as blank pages, it will offer the opportunity to revise all urban activities and processes like means of transportation, waste water treatment, energy generation, and food production. Through designs based on cyclic resource flows and implementing nature-based solutions, these new infrastructures can contribute in the transition towards more circular and sustainable economies. Examples of these applications are synergistic systems, such as aquaponics, that are carried out in recent proposals for floating city designs; to breed fish or produce biofuels, algae and seaweed farms are used, which adsorb CO_2 and other nutrients from waste water flows, while simultaneously reduce wave energy in their function as breakwaters [2].

Figure 1.1: Impression floating city by Oceanix [4]

Obviously, the realization of floating cities involves a wide variety of complex issues. In addition to aspects such as environmental effects and socio-economic issues, it also requires more insight into new technologies. Yet, from a historic point of view, the concept of living on water is not new and floating structures have been used in the field of offshore engineering for quite some time. Several studies have therefore looked at the feasibility of floating cities as a possible application of Very Large Floating Structures (VLFSs), in which they refer to realized projects such as the 'Mega-Float' floating runway in Tokyo Bay, Japan [5][6][7]. Hence, the established knowledge and research regarding these existing offshore structures provide a good starting point for the structural design of floating cities.

While the specific design of a VLFS highly depends on its operational function and location, it can generally be divided into a 'dry' component (e.g. buildings) and a 'floating' component (e.g. platforms). These are referred to as the superstructure and the substructure, respectively. For the substructure, there are two different applications that are commonly used; semi-submersible structures are floating structures that for a large part also protrude above the water, while pontoon-like structures consist of large flat platforms that float directly on the water surface. These pontoon-like structures are characterized by large horizontal dimensions compared to their relatively small drafts. Often in literature, pontoon-like floating structures (PFSs) or modular floating structures (MFSs) are mainly considered for the construction of floating cities.

As floating cities appear to be a viable solution to land scarcity and flood risk, experimental studies have been conducted on conceptual designs regarding the modular floating substructure. Accordingly, various possible shapes and configurations of the platforms were examined, together with their behaviour under certain wave conditions. One of these studies were conducted at the Maritime Research Institute Netherlands, also known as *MARIN*, where they analysed the motion behaviour of a floating island, using the configuration as shown in figure 1.2a.

In 2017, another research project called *SPACE@SEA* was set up to look into the design for floating cities. The project consisted of 17 European partners (including the Dutch company *Blue21* and *MARIN*) and was funded by the *EU Horizon 2020* research and innovation program. To develop "a standardised and cost efficient modular island with low ecological impact", they focused on the research and design of a multi-functional, generic floater, consisting of similarly shaped, floating pontoons [8]. After three years, the configuration for a multi-functional floating island was demonstrated, as shown in figure 1.2b. During the project, studies were conducted regarding a variety of subjects such as the functional and technical requirements, regulations, and installation. The *SPACE@SEA* project focused on four specific applications of the island, namely: aquaculture, transport and logistics, energy production and maintenance, and living [8].

(a) Configuration by MARIN [9]

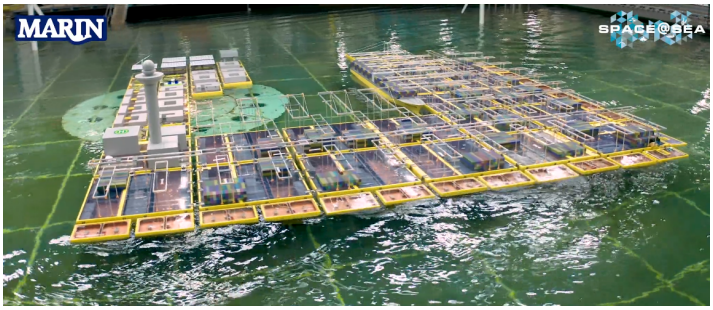

(b) Configuration by SPACE@SEA project [10]

Figure 1.2: Test model configurations used by MARIN and SPACE@SEA project

While the aforementioned advantages show great potential and the development of floating urbanization is making strides forward, many challenges still need to be solved. Considering first design configurations for the substructure of a multi-module floating island, studies demonstrated that these systems contain strong hydrodynamic and mechanical coupling [9][11]. These are valuable observations as it implies that the VLFS response can be significantly influenced by optimizing the structure design. One of the problems that arise regarding the design are unfeasible high forces in the connections. It is possible to reduce forces through design optimization using the coupling phenomenon just described; because the stress results are related to the design configuration and the motion response.

Therefore, better understanding in the underlining relation between structural aspects of a VLFS - such as the stiffness of the different components - and the hydrodynamics is desired to obtain optimal designs for floating cities. Consequently, the importance of accurate methods to analyse the hydroelastic behaviour of these structures plays a significant role; resulting in an increasing demand for the development of numerical models and tools regarding this research area.

1.2 Problem Statement: Hydroelastic Behaviour of VLFSs

With the growing interest in floating structures over the past decades, several theories and numerical models have been developed to describe the response of VLFSs to waves, and to investigate which aspects are decisive in this analysis. When looking at the so-called Fluid-Structure Interaction (FSI) of these systems, considerations regarding hydroelasticity play an important role. This is due to the coupled effects of the wave dynamics and the structural deformations, in combination with the potentially large horizontal dimensions of a VLFS.
According to different theories regarding the hydroelastic response analysis, a VLFS model can be approached as a continuous or discrete system. Both approaches were studied by Ertekin et al. [12], who looked at efficient methods for the hydroelastic analysis of VLFS, referring to them as "Rigid module, flexible connector (RMFC) method", and "Elastic module, flexible connector (EMFC) method". Recently, this was also done by Sun et al. [13], who developed a numerical method to study the hydroelastic behaviour of a hinged structure with two modules, taking into account both rigid and flexible modules.

To improve the design of a VLFS, the motion response and the structural performance has to be analysed. However, to perform a response analysis, the selected model is depended on the decision whether the structure is defined as a continuous or discrete system, which in turn depends on the design. For a VLFS with dimensions up to several kilometers, it is more obvious to model the structure as a continuous system, since large deformations may occur. Yet, for VLFSs consisting of multiple smaller platforms, it is questionable how relevant it is to account for deflections of each module, with respect to the global displacements of the system. Ding et al. [14] determined in their analysis that the RMFC model is appropriate regarding preliminary designs of a smaller multi-module VLFS. On the other hand, Kim

et al. [15] showed the opposite and emphasized that, depending on the arrangement of the modules, assumptions regarding infinite module stiffness can have a significant effect on the response of the structure, even in the case of smaller modules.

As the experimental studies at *MARIN* showed, the connections also have an effect on the response of a floating island with multiple modules [11] [9]. Therefore, the discussion on appropriate assumptions for the material properties involves not only the stiffness of the platforms, but the stiffness of the connections too. Comparing their results to a study obtained by Fu et al. [16], Gao et al. [17] conducted a study in which they looked at a VLFS model consisting of two flexible platforms, with different types of connections. In their research they considered hinge connected modules, semi-rigid connected modules, and a continuous system. For wave conditions with small wavelengths and a not too large angle of incidence, they illustrated that the hinge connector resulted in the greatest reduction of hydroelastic response for the two platforms, while for larger wavelengths this is more the case for a rigid connection. In an effort to minimize the hydroelastic response of a floating structure consisting of two flexible beams, Riyansyah et al. [18] looked at an optimization of the connection design. They considered the relation between the effect of varying rotational stiffness and the location of a connection on the response of the system. For a given wavelength, they stated that indeed minimal compliance occurs when the location and rotational stiffness are optimized. However, several combinations between these variables are possible to obtain minimal hydroelastic response.

Finally, the results of all the aforementioned studies clearly show that the response of a VLFS is also highly dependent on the characteristics of the incident waves. The influence of the wavelength on the response of the structure is mainly reflected in the ratio between the wavelength and the length of the VLFS. This wavelength-to-structure ratio is therefore an important factor in the degree of influence that varying material properties will have on the hydroelastic response of the system.

1.3 Research Approach & Thesis Outline

The problem statement as described above shows that there is a strong relation between the response of the system, the stiffness of the modules and connections, and the incident wave length. In general, by increasing the overall stiffness of a structure, the system can deflect less easy. However, this will significantly increase the resulting stresses in the structure, which in turn can have a negative impact on its structural performance. Moreover, increasing the bending stiffness changes the characteristics of the system (e.g. its mass and its natural frequency), which can result in a larger hydroelastic response of a floating structure [18]. Clearly, there is a fine balance between the permissible displacements of a VLFS and the resulting stresses, in which the stiffness of the structure and the wave length play an important role.

Although there are several studies (such as those discussed previously) that already have looked into these aspects, to the author's best knowledge, the hydroelastic response has not been studied where the stiffness of the modules is plotted against the stiffness of connections for a wider range of values. Previous studies have only looked at the effect on the response of the VLFS by varying the stiffness of one of the structural components individually. However, as discussed earlier, experimental observations show strong coupling effects within the system. This means that the response can be very different for specific combinations of the material properties of the separated structural elements. It is therefore a valuable objective to also analyse the effects for a range of different module/connection stiffness combinations. This provides more insight on how these stiffness variables relate to each other in terms of their influence on the response of the system, i.e. the maximum displacements and bending moments. In addition, by analysing the response of the VLFS model for varying stiffness it is also possible to obtain insight into the combination of these material properties for which the system is more likely to behave as a continuous system or as rigid modules. Ultimately, understanding this relation can provide profitable information in the optimization of a VLFS design.

1.3.1 Research question & scope

To obtain better understanding in the underlining relation between the hydrodynamic and structural aspects with regard to the hydroelastic behaviour of a VLFS, the following research question will be investigated:

> ***How does the bending stiffness of the modules and the rotational stiffness of the connections relate to each other in terms of their influence on the response of a multi-module VLFS, and what is their effect on the vertical displacement and the bending moment of the system, considering different wave lengths?***

Accordingly, the following sub-topics will be part of the research scope:
(how these sub-topics are presented in this thesis is explained in more detail in the next subsection)

- mathematical formulation of a (multi-module) VLFS model
- numerical methods for solving the analytical problem and the introduction to FEM
- developing a FEM model using *Gridap*
- model validation and selecting model input parameters
- post-processing and analysing results

1.3.2 Research approach & methodology

The approach to this research question includes a hydroelastic response analysis of a multi-module VLFS, while looking at the effect of varying stiffness of the modules and the connections. Therefore, a two dimensional FSI model is set up to analyse the behaviour of the considered structure. First, the physical problem is described analytically, for which credible assumptions are considered regarding the problem definition. As a result, the fluid-structure interaction is mathematically described by a coupled system of partial differential equations (PDEs). To solve this system of equations, the finite element method (FEM) is applied, where the FE-package *Gridap* [19] is used to set up and solve the numerical model, written in *Julia* programming language [20]. The model will be validated by comparing the obtained results to previous studies which used a similar problem definition.

Ultimately, results can be obtained regarding the vertical displacements and moment distributions along the structure. Moreover, the maximum vertical displacement and maximum bending moment related to varying combinations of the stiffness are calculated and visualized by means of contour plots. It is discussed that the wavelength-to-structure ratio also has a strong influence on the response. The (maximum) vertical displacement and the bending moment are therefore analysed for different wavelengths.

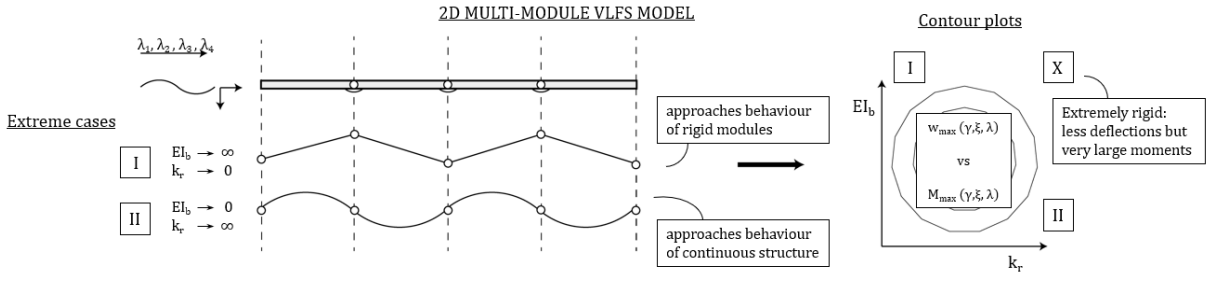

Figure 1.3: Visual overview of research approach

Based on these results, conclusions can be drawn regarding the effect of different combinations of the material properties on the vertical displacement and bending moment, for different wavelength-to-structure ratios. In addition, this also provides insight into the conditions for which a VLFS is more likely to behave as a continuous or a discrete system, according to the aspects considered in this thesis.

1.3.3 General outline of the thesis

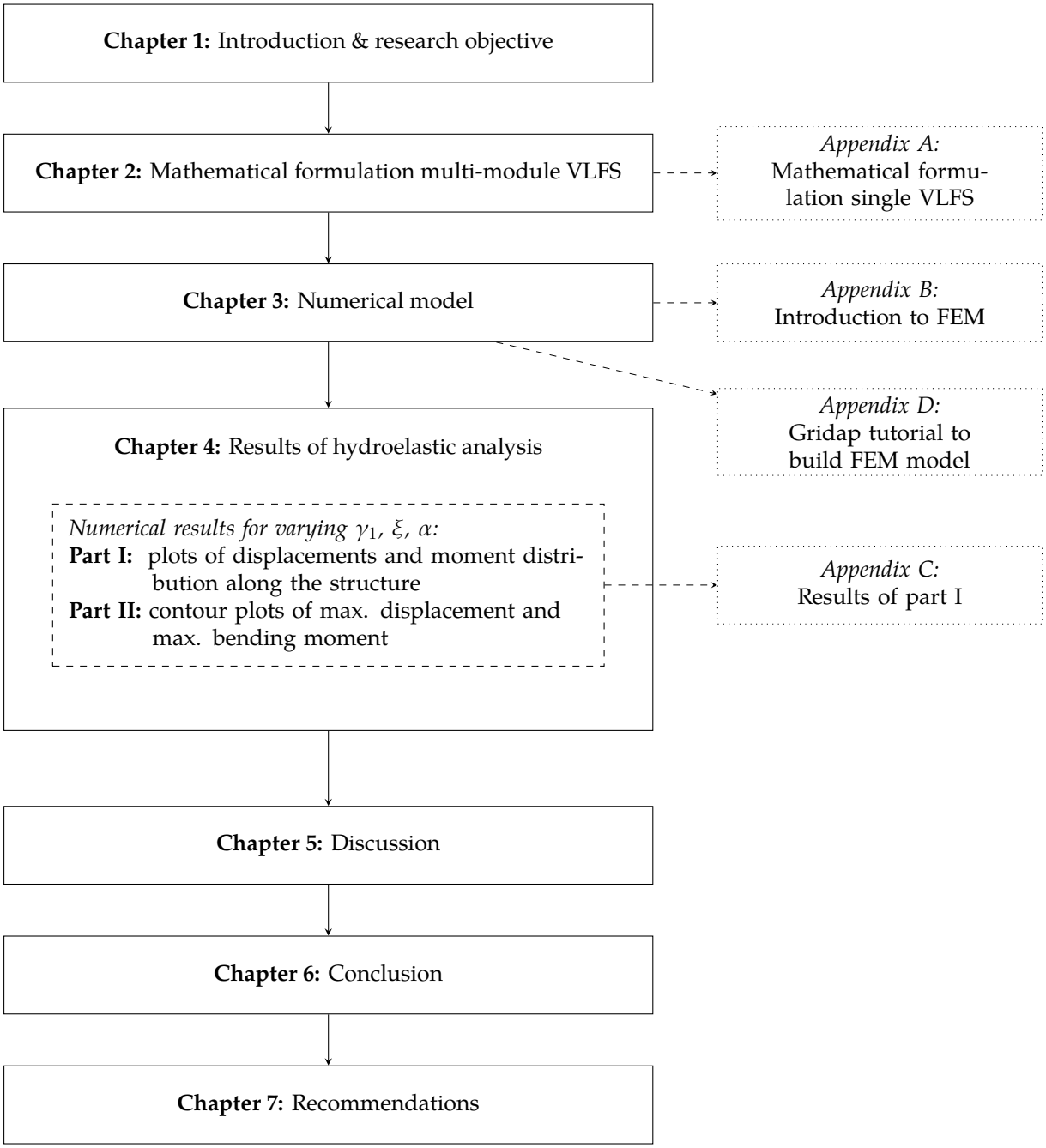

2
Analytical Formulation of Multi-Module VLFS Model

The aim of this research is to obtain more insight in the relation between the stiffness of the modules and the connections, and how this relation affects the vertical displacement and bending moments of a multi-module VLFS. To this end, a hydroelastic response analysis is performed. The physical problem is represented by a schematized model that considers the coupling between the fluid and the structure; also known as Fluid-Structure Interaction (FSI).

As discussed in subsection 1.2, the VLFS can be modeled as a discrete or continuous system. Considering the research objective, it is important to include possible variations in flexibility into the model, such that the stiffness of the different components can vary between lower and higher values (i.e flexible and rigid). As a starting point, the elasticity of the system is therefore determined to be continuously distributed along the structure and so the coupled system is represented analytically by a continuous model.

The multi-module VLFS discussed in this thesis consists of four floating platforms, interconnected through rotational springs. The floating platforms are schematized by four one-dimensional beams, for which the Euler-Bernoulli beam theory is applied. The water is represented by a two-dimensional fluid domain. The mathematical formulations and underlying assumptions related to a single Euler-Bernoulli floating beam model are discussed in detail in appendix A. The governing equations and assumptions for this single beam model form the basis for the model of the multi-module VLFS. Therefore, the analytical formulation is described in a similar way as discussed in appendix A. First, the problem definition is drawn up and defined by several assumptions, which will determine the frame of reference for which the system is solved. Subsequently, the mathematical formulation of the system is derived, including the governing equations, with the related boundary and interface conditions. As a result, the complete statement of the problem is described by a system of partial differential equations (PDEs), expressed in the frequency domain. In the last section, two different methods are briefly discussed to solve the defined problem.

2.1 Problem Definition: Multi-Module VLFS

As shown in figure 2.1, the multi-module VLFS is represented by four floating one-dimensional beams, based on the Euler-Bernoulli theory, interconnected by rotational springs. The structure is located on a two-dimensional fluid domain, where the whole system is defined in a Cartesian (x,z-)coordinate system. The beams will only perform small displacements in vertical direction and it is assumed that the system is linear.

The structural elements are considered to be homogeneous, where the bending stiffness, the mass density, the height, and the length of each beam are denoted as EI, ρ_b , h_b, and βL, respectively. The mass of the structure and the bending stiffness are related to each other; when considering the second moment of inertia for a rectangular cross-section, $I = \frac{1}{12} b h^3$, the mass is proportional to the beam height to the power of one, and the bending stiffness to the power of three. As shown in figure 2.1, the pa-

rameter γ_1 is therefore introduced, to account for this dependence when varying the bending stiffness. Furthermore, the beams are connected to each other by means of rotational springs. For each spring, the rotational stiffness is indicated as k_r, where k_r is generally defined as the bending stiffness over the length, multiplied by the rotational stiffness parameter ξ.

Regarding the fluid domain, it is assumed that the water is inviscid, incompressible, and has irrotational flow. Similar to the single-beam model (see section A.1), the same arguments apply with respect to these assumptions. The fluid domain has a constant depth, d, and a constant density, ρ_w. The domain is defined by vertical boundaries, $\Gamma_{\pm\infty}$, the bottom surface, Γ_b, the free water surface, Γ_{fs}, and the interface between the beams and the fluid, Γ_{str}.

Looking at the wave excitation for this model, the structure is subject to small, single frequency, head waves with a wavelength λ, where the incident wavelength is related to the total length of the structure, by means of the parameter α. Consequently, the linear (Airy) wave theory is assumed to be valid, provided that the beams are always in contact with the fluid [18]. Based on the linear wave theory, the wave frequency ω and the incident wave length λ are related through the dispersion relation as defined in section A.1.

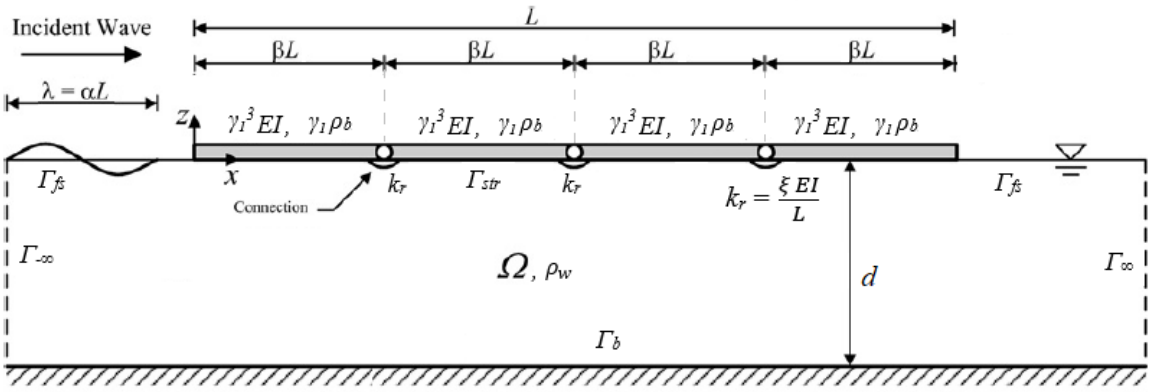

Figure 2.1: 2D multi-module VLFS model

2.2 Mathematical Formulation in the Frequency Domain

The excitation of the waves changes the water pressure and the elevation at the water surface, causing vertical displacements of the floating beams. This interaction between the motion of the water and the displacement of the structure is mathematically described by equations that depend on space and time. To solve these partial differential equations, boundary and interface conditions are required. Therefore, the resulting system of PDEs includes the following components:

- equation of motion (EoM) of the fluid
- equation of motion (EoM) of the VLFS
- boundary conditions (BCs) for the fluid domain
- interface conditions (ICs) for fluid-structure interface
- boundary conditions (BCs) for the structural domain

2.2.1 Governing equations and conditions

As mentioned, this model is subject to the same assumptions and wave conditions as the single beam model described in appendix A.2. This allows the EoM and BCs to be derived in a similar manner. The applied equations are therefore only briefly explained in this chapter, where the derivations are explained in more detail in the appendix A.2.

Based on the assumptions, it is more convenient to solve the system of PDEs in the frequency domain. In section A.3 the transformation from the time domain to the frequency domain is discussed, by using the Fourier transform pair:

$$\tilde{G}(\omega) = \int_{-\infty}^{\infty} g(t)\, e^{-i\omega t}\, dt \qquad \text{and} \qquad g(t) = \frac{1}{2\pi} \int_{-\infty}^{\infty} \tilde{G}(\omega)\, e^{i\omega t}\, d\omega \tag{2.1}$$

Due to the linearity of the system, this approach may be applied and each quantity in the time domain is rewritten in its respective term in the frequency domain. Hence, all equations for this model are expressed in terms of their space dependence in the frequency domain, where all quantities are complex-valued and are frequency dependent [21]. Consequently, the solution to the problem will be solved considering the steady-state solution.

For convenience, the space and frequency dependence has been omitted from the arguments below

Equation of motion of the fluid

Based on the aforementioned assumptions with respect to the fluid characteristics, the motion of the fluid can be described in terms of the velocity potential ϕ, which satisfies the Laplace equation in the fluid domain. Hence, both the Laplace equation and the expression for the water pressure are defined as follows:

$$\nabla^2 \phi = 0 \qquad \text{in} \quad \Omega \tag{2.2}$$

$$\begin{aligned} -i\omega\phi + \frac{p}{\rho_w} + gz &= 0 \qquad \text{in} \quad \Omega \\ \rightarrow \quad p &= -\rho_w g z + i\omega\rho_w \phi \end{aligned} \tag{2.3}$$

With water density ρ_w, gravitational constant g, vertical coordinate z, imaginary number i, and the frequency ω.

Equation of motion of the VLFS

According to the Euler-Bernoulli beam theory, the equation of motion for floating structure is described as follows:

$$-\omega^2 \rho_b h_b w + EI \frac{\partial^4 w}{\partial x^4} = p\,\big|_{\Gamma_{str}} \qquad \text{on} \quad \Gamma_{str} \tag{2.4}$$

Where w is the displacement of the structure in z-direction and p is the pressure at the water surface acting on the bottom of the VLFS, i.e. the interface of the structure and the fluid. Similar to the single beam model, for the flexible floating beam system as presented here, the effects of structural damping in the system can be neglected [18].

Boundary conditions fluid domain

As shown in figure 2.1, the fluid domain is bounded by the seabed, Γ_b, the water surface, which is divided into Γ_{fs} and Γ_{str}, and the vertical boundaries, described as $\Gamma_{-\infty}$ and $\Gamma_{+\infty}$. For each boundary, the following conditions are defined:

Seabed
At the seabed no water is allowed to flow through the bottom. Therefore, the spatial derivative of the potential ϕ, normal to the seabed is equal to zero:

$$\vec{n} \cdot \nabla\phi = 0 \qquad \text{on} \quad \Gamma_b \tag{2.5}$$

Vertical boundaries
The waves propagate from x = -∞ to x= +∞, requiring no reflections at the vertical boundaries. Therefore, the Sommerfeld radiation conditions should be satisfied at $\Gamma_{-\infty}$ and $\Gamma_{+\infty}$ [17]:

$$\vec{n} \cdot \nabla\phi = ik\phi \qquad \text{on} \quad \Gamma_{+\infty} \tag{2.6}$$
$$\vec{n} \cdot \nabla\phi = -ik\phi \qquad \text{on} \quad \Gamma_{-\infty} \tag{2.7}$$

Free surface
At the surface, the water should satisfy both a kinematic and a dynamic boundary condition, where the function η is introduced to describe the surface elevation of the water[1]. With regard to the kinematic boundary condition at the free surface, Γ_{fs}, the water particle velocity in normal direction to the surface should be equal to the velocity of the surface elevation [22]. Regarding the dynamic condition, the water pressure at the surface (see eq 2.3) should be equal to the atmospheric pressure, i.e. equal to zero:

$$\text{kinematic:} \qquad \vec{n} \cdot \nabla\phi = -i\omega\eta \qquad \text{on} \quad \Gamma_{fs} \tag{2.8}$$
$$\text{dynamic:} \qquad -i\omega\phi + g\eta = 0 \qquad \text{on} \quad \Gamma_{fs} \tag{2.9}$$

Fluid-structure interface
Also at the fluid-structure interface both a kinematic and a dynamic condition is defined, based on the assumption that the structure is always in contact with the water surface. Accordingly, for the kinematic condition, the elevation of the water surface is equal to the displacement of the floating beams. Considering the dynamic boundary condition, the water pressure at the surface acts as a distributed load at the bottom of the structure. Hence, the expression for the water pressure (see eq. 2.3) is substituted in the EoM of the VLFS (see eq. 2.2):

$$\text{kinematic:} \qquad -i\omega w = -i\omega\eta \quad \rightarrow \quad -i\omega w = \vec{n} \cdot \nabla\phi \qquad \text{on} \quad \Gamma_{str} \tag{2.10}$$
$$\text{dynamic:} \qquad -\omega^2\rho_b h_b w + EI\frac{\partial^4 w}{\partial x^4} = \rho_w i\omega\phi - \rho_w g\eta \qquad \text{on} \quad \Gamma_{str} \tag{2.11}$$

Boundary conditions structural domain

With regard to the boundary conditions of the structure, the moments and shear forces at its free ends should be equal to zero. Consequently, at $x = 0$ and $x = L$, the following four dynamic BCs must be satisfied:

$$\left.\frac{\partial^2 w}{\partial x^2}\right|_{x=0} = \left.\frac{\partial^3 w}{\partial x^3}\right|_{x=0} = 0 \qquad \text{on} \quad \Gamma_{str} \tag{2.12}$$
$$\left.\frac{\partial^2 w}{\partial x^2}\right|_{x=L} = \left.\frac{\partial^3 w}{\partial x^3}\right|_{x=L} = 0 \qquad \text{on} \quad \Gamma_{str} \tag{2.13}$$

[1] i.e. the elevation in water surface, measured relative to the mean water level, caused by waves that are only subject to gravity

The beams are interconnected through rotational springs, hence, some additional interface conditions are defined at the connections. At each connection point, $x = x_j$ on Γ_{str}, both the kinematic conditions (i.e. continuity in displacement and rotation) and the dynamic boundary conditions (i.e. force equilibrium) are determined accordingly:

$$w\big|_{x_j^-} = w\big|_{x_j^+} \tag{2.14}$$

$$\frac{\partial w}{\partial x}\Big|_{x_j^-} = \frac{\partial w}{\partial x}\Big|_{x_j^+} \tag{2.15}$$

$$EI\frac{\partial^2 w}{\partial x^2}\Big|_{x_j^-} = EI\frac{\partial^2 w}{\partial x^2}\Big|_{x_j^+} = k_r\left(\frac{\partial w}{\partial x}\Big|_{x_j^-} - \frac{\partial w}{\partial x}\Big|_{x_j^+}\right) \tag{2.16}$$

$$EI\frac{\partial^3 w}{\partial x^3}\Big|_{x_j^-} = EI\frac{\partial^3 w}{\partial x^3}\Big|_{x_j^+} \tag{2.17}$$

To conclude, the motion of the fluid is described by the Laplace equation within the fluid domain, where the equation of motion for the structure is substituted as a complex boundary condition for the fluid-structure interface. Together with the other boundary conditions as defined above, this results in a well-posed problem, which can now be solved.

2.3 Solution Methods for Solving FSI Problems

In general, the stated problem can be solved using two different methods:

1. *Numerical methods*
2. *Semi-analytical methods*

The numerical methods (i.e. Finite Element Models (FEM) or Finite Differences (FD)) involve computational models which discretize the domain (FE) or substitute the differentials with finite differences [21]. The semi-analytical methods are based on the responses of the system which are expressed in terms of a summation of fluid and structural modes. A commonly used semi-analytical approach is the so-called modal decomposition method, where the motions of the structure and the fluid are described by a summation of functions.

The system of PDEs is dependent on several variables, making it complex to solve such a model analytically. In addition, the velocity potential at the surface, and vertical boundaries of the fluid must satisfy a condition that includes the argument of the unknown parameter itself, which requires iterative calculations to describe the behaviour of the water. The formulated problem is therefore considered to be too complex to solve (semi-)analytically. Hence, the FSI problem will be analysed by means of a numerical model, using the Finite Element Method.

3 Numerical Model of Multi-Module VLFS

In the previous chapter, the physical problem of a multi-module VLFS was schematized, where the mathematical formulation resulted in a coupled system of PDEs. To solve PDEs, the Finite Element Method (FEM) is often used because it provides efficient computational implementation. Developing a generic numerical model also serves further design purposes as it offers the possibility to easily simulate the response of the system for different inputs parameters with respect to e.g. material properties, shapes, and configurations. Therefore a 2D FEM model is built, where the model is written in the *Julia* programming language, using the FE-library *Gridap*. The computational implementation of Gridap and the problem description with respect to the numerical domain are discussed in section 3.1.

An introduction to FEM is discussed in appendix B, where the general steps for the implementation of the method are explained in more detail. An important part in the FEM approach is the derivation of the 'weak form' of the PDEs and the spatial discretization. Hence, these aspects are discussed in section 3.2. A tutorial is included in appendix D, which contains complete instructions to set up the FEM model and to solve the FSI problem with Gridap.
Finally, the model is validated using results from a study by Riyansyah et al. [18], who looked at the hydroelastic behaviour of a VLFS model consisting of two floating beams, interconnected by a rotational spring.

3.1 FEM Model Set-up using Gridap

The FEM model is developed using the library Gridap; which is a "new Finite Element (FE) framework, exclusively written in the Julia programming language, for the numerical simulation of a wide range of mathematical models governed by partial differential equations" [19]. Julia is an open source programming language which combines the performance of compiled languages like C/C++, with the productivity of scripting languages such as Python and it is therefore one of the fastest languages at the moment, while providing a high-level user front-end [20].
Accordingly, Gridap has been implemented in Julia to provide a high-performing, accessible framework for working with FE libraries in order to solve complex PDE systems, both linear and non-linear. Due to its indicative application programming interface, models in Gridap can be coded in a very compact way, where the equations can be written with a syntax very close to the mathematical formulation.

Therefore, the FE package Gridap is used to develop the 2D numerical model, based on the general application of FEM as discussed in appendix B. Founded on the analytical formulation from the previous chapter, the numerical model is set up, for which the numerical domain and the associated boundary conditions are specified in the subsection below.

3.1.1 2D FSI model

The domain as implemented in the FEM model is illustrated in figure 3.1. Based on the analytical problem definition depicted in figure 2.1, the numerical model is defined by the 2D fluid domain, Ω, which is bounded by the bottom, Γ_b, the free water surface, Γ_{fs}, the vertical boundaries, $\Gamma_{L,R}$, and the fluid-structure interface, Γ_{str}. In the model, the incident waves propagate from left to right. In addition to the analytical formulation, the numerical model has additional 'sub-domains' that act as damping zones to satisfy the radiation conditions at the vertical boundaries. The implementation of these damping zones is explained in more depth in subsection 3.1.2.

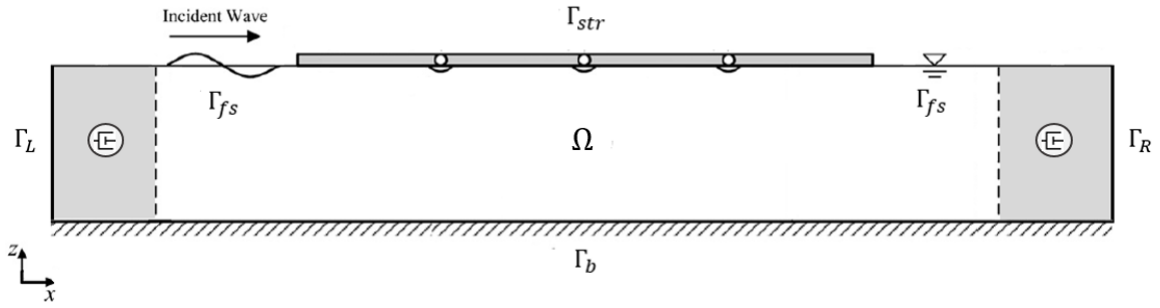

Figure 3.1: 2D numerical FSI model

According to the mathematical formulation discussed in section 2.2, the problem is defined by the Laplace equation within the domain:

$$\nabla^2\phi = 0 \qquad \text{in} \quad \Omega \tag{3.1}$$

with the conditions at the bottom and the vertical boundaries,

$$\vec{n}\cdot\nabla\phi = 0 \qquad \text{on} \quad \Gamma_b \tag{3.2}$$
$$\vec{n}\cdot\nabla\phi = 0 \qquad \text{on} \quad \Gamma_R \tag{3.3}$$
$$\vec{n}\cdot\nabla\phi = \vec{n}\cdot\nabla\phi_{\text{inc}} \qquad \text{on} \quad \Gamma_L \tag{3.4}$$

and the conditions at the free surface and the fluid-structure interface,

$$-i\omega\eta - \frac{\partial\phi}{\partial z} + \mu_1(\eta - \eta_{\text{inc}}) + \frac{\mu_2}{g}(\phi - \phi_{\text{inc}}) = 0 \qquad \text{on} \quad \Gamma_{fs} \tag{3.5}$$
$$-i\omega\phi + g\eta = 0 \qquad \text{on} \quad \Gamma_{fs} \tag{3.6}$$
$$-i\omega\eta - \frac{\partial\phi}{\partial z} = 0 \qquad \text{on} \quad \Gamma_{str} \tag{3.7}$$
$$-\omega^2\alpha_{b1}\eta + \alpha_{b2}\frac{\partial^4\eta}{\partial x^4} - i\omega\phi + g\eta = 0 \qquad \text{on} \quad \Gamma_{str} \tag{3.8}$$

where $\alpha_{b1} = \frac{\rho_b h_b}{\rho_w}$, and $\alpha_{b2} = \frac{EI}{\rho_w}$

Looking at equations 2.12 to 2.17, additional conditions have also been defined at the free ends of the structure and at the connections. How these conditions are implemented in the numerical model is explained in section 3.2.

Remark. *The equation of motion for the structure is substituted as a complex boundary condition of the fluid domain, at the interface between fluid and structure. For computational convenience, the vertical displacement of the structure - previously indicated with w - is therefore rewritten in terms of the surface elevation η. Moreover, due to the damping zones, the kinematic BC for the free surface contains some additional terms, while the BCs for the vertical boundaries are adjusted (see subsection 3.1.2).*

According to the linear wave theory, the potential of the incident wave ϕ_{inc} for perpendicular waves and considering water of finite depth, is written in the following form [23]

$$\phi_{\text{inc}} = \frac{gA_w}{i\omega} \frac{\cosh k(z+d)}{\cosh kd} \mathrm{e}^{ikx} \tag{3.9}$$

Where A_w is the wave amplitude of the incident wave. As mentioned earlier, the incident wave number k, the wave frequency ω, and the incident wavelength λ, are related through the dispersion relation as defined in section A.1.

Consequently, the expressions for the surface elevation of the incident wave η_{inc} and the velocity of the fluid in x-direction over the boundary Γ_L are formulated as follows:

$$\frac{\partial \phi_{\text{inc}}}{\partial z} = -i\omega\eta_{\text{inc}} \qquad \rightarrow \qquad \eta_{\text{inc}} = \frac{gA_w k}{\omega^2} \frac{\sinh k(z+d)}{\cosh kd} \mathrm{e}^{ikx} \tag{3.10}$$

$$\vec{n} \cdot \nabla \phi_{\text{inc}}\big|_{\Gamma_L} \qquad \rightarrow \qquad \frac{\partial \phi_{\text{inc}}}{\partial x} = \frac{gA_w k}{\omega} \frac{\cosh k(z+d)}{\cosh kd} \mathrm{e}^{ikx} \tag{3.11}$$

3.1.2 Damping zone

As defined by equation 2.6, the radiation conditions should hold for $x \rightarrow \pm\infty$. This condition requires for the waves to fully propagate away from the system and should not reflect at the vertical boundaries. In other words, towards the vertical boundaries, the wave energy dissipates from the system. Therefore two damping zones, at both the inlet and the outlet, are constructed in the model; to assure energy dissipation at $\Gamma_{L,R}$ such that the BCs for $x \rightarrow \pm\infty$ are satisfied. As a result, the BC at Γ_L is now determined by the predefined expression for the incident wave, ϕ_{inc}, while the BC at Γ_R is set to zero.

The implementation of these damping zones is based on the results of experimental studies conducted by Kim et al. [24], who performed a numerical analysis of various artificial damping schemes for a three-dimensional numerical wave tank. In their paper, Kim et al. compared five different damping methods at the end of the computational domain by introducing a variety of additional terms for the free surface boundary conditions in the damping zone. They applied two damping coefficients, μ_1 and μ_2, to either the kinematic BC, the dynamic BC or combinations of both. Moreover, four different ramp functions were investigated to induce a gradual change of the damping magnitude in order to avoid abrupt changes of free-surface conditions near the entrance of the damping zone [24].

Based on their findings, method 4 is used for the numerical model; where the damping coefficients μ_1 and μ_2 are solely applied to the kinematic boundary condition of the free surface. This results in the following adjustments for the kinematic BC at Γ_{fs}:

$$\text{damping zone at outlet: } -i\omega\eta - \frac{\partial \phi}{\partial z} + \mu_1\eta + \frac{\mu_2}{g}\phi = 0 \tag{3.12}$$

$$\text{damping zone at inlet: } -i\omega\eta - \frac{\partial \phi}{\partial z} + \mu_1(\eta - \eta^*) + \frac{\mu_2}{g}(\phi - \phi^*) = 0 \tag{3.13}$$

Where η^* and ϕ^* (defined by the incident wave expression) are the reference values when the computational domain is not disturbed by any structure during the wave propagation [24]. Ultimately, equation 3.13 is used to provide the full expression for the free surface BC including the additional terms for the damping zones at both sides, where the ramp functions for the coefficients are defined such that they return the correct value for $\mu_{1,2}$ for each of the associated damping zones.

Considering method 4, Kim et al. derived the following relation between the damping coefficients:

$$\mu_2(x) = -\frac{\mu_1(x)^2}{4} \tag{3.14}$$

Subsequently, a gradual change of the damping magnitude along the damping zone is obtained using 'ramp shape 1' (see figure 3.2), for which Kim et al. proposed the following ramp function:

$$\mu_1(x) = \mu_0 \left[1 - \cos \left\{ \frac{\pi}{2} \left(\frac{x - x_d}{L_d} \right) \right\} \right] \tag{3.15}$$

Where L_d and $x - x_d$ are the total length and the local length of the respective damping zone. The input value, μ_0, is selected on a trial and error basis, depending on the wave characteristics [24].

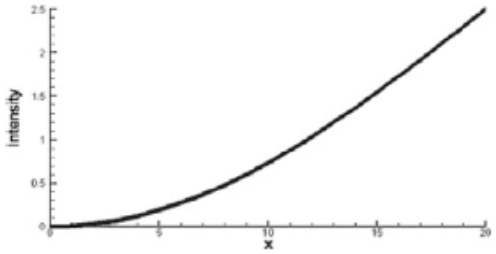

Figure 3.2: Ramp shape - damping zone [24]

3.2 Weak Form & Spatial Discretization

In a FEM model, the continuous domain is divided into smaller finite elements, where it is assumed that the unknown displacements for the entire domain are determined by calculating the displacements in the nodes of these predefined elements. Subsequently, the interpolation between these nodal points is described by so-called shape functions, which are associated to the predefined elements. A general introduction to FEM is discussed in more detail in appendix B. It is pointed out here that in order to apply the method, the governing equations must be cast in the weak form, where an example the weak form has been derived for the Laplace equation. Once the weak formulation for the system is derived, the approximated solution to the system is formulated by means of the spatial discretization, using a Continuous Galerkin / Discontinuous Galerkin (CG/DG) approach.

3.2.1 Derivation of the weak form

Elaborating on the example as discussed in subsection B.2, here, the Laplace equation is multiplied with weight function w and integrated over the domain Ω. The equation is then integrated by parts, where the kinematic conditions are substituted in the expression. Similarly, the equation for the dynamic boundary conditions is multiplied with weight function v and integrated over the boundary.

As a result, $\mathcal{V}$ and $\mathcal{V}_\Gamma$ are defined as the functional spaces for the domain Ω, and boundary Γ, in order to find the solution for $[\phi, \eta] \in \mathcal{V} \times \mathcal{V}_\Gamma$ such that

$$B([\phi, \eta], [w, v]) = l([w, v]) \qquad \forall\, [w, v] \in \mathcal{V} \times \mathcal{V}_\Gamma \tag{3.16}$$

Where the bilinear form is given by

$$\begin{aligned} B([\phi, \eta], [w, v]) = & \int_\Omega \left(\nabla w \cdot \nabla \phi \right) d\Omega \quad + \\ & \int_\Gamma \left(g\, v\, \eta - i\omega\, v\, \phi + i\omega\, w\, \eta - \mu_1\, w\, \eta - \frac{\mu_2}{g}\, w\, \phi \right) d\Gamma_{fs} \quad + \\ & \int_\Gamma \left((-\omega^2 \alpha_{b1} + g)\, v\, \eta + \alpha_{b2}\, \Delta v \cdot \Delta \eta - i\omega\, v\, \phi + i\omega\, w\, \eta \right) d\Gamma_{str} \end{aligned} \tag{3.17}$$

and the linear form is given by

$$l([w,v]) = \int_\Gamma \Big(w\,\nabla\phi_{in} \Big)\, d\Gamma_L - \int_\Gamma \Big(\mu_1\, w\,\eta_{in} + \frac{\mu_2}{g}\, w\,\phi_{in} \Big)\, d\Gamma_{fs} \tag{3.18}$$

Alternatively, the bilinear and linear form can be rewritten in a more concise way:

$$\begin{aligned} B([\phi,\eta],[w,v]) =& \big(\nabla\phi, \nabla w \big)_\Omega \quad + \\ & \big(g\eta - i\omega\phi, v \big)_{\Gamma_{fs}} + \big(i\omega\eta - \mu_1\eta - \frac{\mu_2}{g}\phi, w \big)_{\Gamma_{fs}} \quad + \\ & \big((-\omega^2\alpha_{b1} + g)\eta - i\omega\phi, v \big)_{\Gamma_{str}} + \big(\alpha_{b2}\Delta\eta, \Delta v \big)_{\Gamma_{str}} + \big(i\omega\eta, w \big)_{\Gamma_{str}} \end{aligned} \tag{3.19}$$

$$l([w,v]) = \big(\nabla\phi_{in}, w \big)_{\Gamma_L} - \big(\mu_1\eta_{in} + \frac{\mu_2}{g}\phi_{in}, w \big)_{\Gamma_{fs}}$$

Boundary conditions at the free ends of the structure

The boundary conditions at the free ends of the structure (see eq 2.12 and 2.13) are indirectly substituted in the bilinear form. In deriving the weak formulation, equation 3.8 is multiplied by the weight function v and integrated over its associated boundary, i.e. the boundary Γ_{str}. Subsequently, the second term of equation 3.8 is then integrated by parts twice, which results in:

$$\int_\Gamma \Big(\alpha_{b2}\, v \cdot \Delta^2\eta \Big)\, d\Gamma_{str} = \int_\Gamma \Big(\alpha_{b2}\, \Delta v \cdot \Delta\eta \Big)\, d\Gamma_{str} + \underbrace{\alpha_{b2}\, \nabla v \cdot \Delta\eta}_{\equiv M}\Big|_0^L + \underbrace{\alpha_{b2}\, v\nabla(\Delta\eta)}_{\equiv V}\Big|_0^L \tag{3.20}$$

Considering the BCs, the moments and shear forces are equal zero at the free ends ($x = 0$ and $x = L$). Therefore, the last two terms will disappear from the expression, leaving only the first term in the bilinear form.

3.2.2 Spatial discretization - CG/DG approach

According to the Galerkin method, as discussed in appendix B.3, an approximation to the exact solution can be described by the sum of known shape functions and the displacements at the nodes of the respective elements. Hence, for the potential flow this would result in:

$$\phi_h = \sum_{i=1}^{n} N_i \hat{\phi}_i \tag{3.21}$$

Therefore, the continuous domain is discretized by means of a FE mesh. The discretized domain is defined by Ω_h and the discrete boundary facets associated with the FE mesh are described by $\Gamma_{b,h}$, $\Gamma_{L,h}$, $\Gamma_{R,h}$, $\Gamma_{fs,h}$, and $\Gamma_{str,h}$. In addition, a set of interior facets of the elements is defined, where the interior between the facets of $\Gamma_{str,h}$ are defined by $\Lambda_{str,h}$.

There are two important considerations regarding the bilinear form to ensure that the problem can be solved and that the solution is unique. The first one is continuity. The bilinear form in equation 3.17 contains both first, and second order derivatives. The finite element spaces therefore require continuous gradients between elements, i.e. C^1 continuity across elements. This can be achieved by selecting types of finite elements, e.g. Hermite elements, which ensure this continuity condition.
However, Colomés et al. [25] proposed an alternative formulation based on a Continuous Galerkin /

Discontinuous Galerkin (CG/DG) approach for fourth order operators, where the discrete functions are continuous at the element nodes, but the gradient is discontinuous. Therefore, linear Lagrangian elements can be applied, while continuity of the gradient over adjacent elements is weakly enforced by means of an interior penalty approach.

Regarding this interior penalty approach, the jump, and mean value operators are introduced. The general formulation of these operators suggests that for a given function $v \in \mathcal{V}$ (restricted to the interior facets)

$$[v\, n] \doteq v^+ n^+ + v^- n^-, \tag{3.22}$$

$$\{\nabla v\} \doteq \frac{\nabla v^+ + \nabla v^-}{2}, \tag{3.23}$$

with v^+, and v^- being restrictions to the cells that share a generic interior facet, and n^+, and n^- are the facet outward unit normals from either of the respective element [26].

Secondly, coercivity should be guaranteed in order for the numerical system to be stable. To this end, Akkerman et al. [27] proposed a monolithic weak formulation, that includes additional terms to the weight function v, regarding the conditions at the free surface. This results in a bilinear form where the free surface condition contains an extra term $\alpha_f w$ added to the weight function v, multiplied by a constant β_h. The approach to ensure coercivity by applying these additional terms is further explained in subsection 3.2.3.

Hence, the stabilization terms are included in the bilinear formulation according to the CG/DG approach proposed by Colomés et al. [25]; in order to find the approximated solution for $[\phi_h, \eta_h] \in \hat{\mathcal{V}}_h \times \hat{\mathcal{V}}_{\Gamma,h}$ such that

$$\hat{B}_h([\phi_h, \eta_h], [w_h, v_h]) = l_h([w_h, v_h]) \qquad \forall\, [w_h, v_h] \in \hat{\mathcal{V}}_h \times \hat{\mathcal{V}}_{\Gamma,h} \tag{3.24}$$

Where the bilinear form is given by

$$\begin{aligned}
\hat{B}_h([\phi, \eta_h], [w_h, v_h]) = {} & \left(\nabla\phi_h, \nabla w_h\right)_{\Omega,h} + \\
& \beta_h\Big(\left((g\eta_h - i\omega\phi_h), (v_h + \alpha_f w_h)\right)_{\Gamma_{fs,h}} + \left(i\omega\eta_h - \mu_1\eta_h - \frac{\mu_2}{g}\phi_h, w_h\right)_{\Gamma_{fs,h}} + \\
& \Big(\left((-\omega^2\alpha_{b1} + g)\eta_h - i\omega\phi_h\right), v_h\Big)\Gamma_{str,h} + \left(i\omega\eta_h, w_h\right)_{\Gamma_{str,h}} + \\
& \left(\alpha_{b2}\Delta\eta_h, \Delta v_h\right)_{\Gamma_{str,h}} - \\
& \alpha_{b2}\Big(\left(\{\Delta\eta_h\}, [\nabla v_h \cdot \vec{n}_\Lambda]\right) + \left([\nabla\eta_h \cdot \vec{n}_\Lambda], \{\Delta v_h\}\right)\Big)_{\Lambda_{str,h}} + \\
& \frac{\gamma_m}{h}\Big(\left([\nabla\eta_h \cdot \vec{n}_\Lambda], [\nabla v_h \cdot \vec{n}_\Lambda]\right)\Big)_{\Lambda_{str,h}}
\end{aligned} \tag{3.25}$$

and the linear form is given by

$$l_h([w_h, v_h]) = \left(\nabla\phi_{in,h}\,, w_h\right)_{\Gamma_{L,h}} - \Big(\left(\mu_1\eta_{in,h} + \frac{\mu_2}{g}\phi_{in,h}\right), w_h\Big)_{\Gamma_{fs,h}}$$

Interface conditions at the connections

The interface conditions at the connections are defined in equations 2.14 to 2.17. Between adjacent beams continuity must be satisfied regarding the displacement, rotation, shear force, and bending moment,

where the latter is determined by the difference in gradient of the displacements over the connection, multiplied by the rotational stiffness of the spring. The approach to weakly force conditions between adjacent elements by means of an extra term in the bilinear form is also used to impose the interface condition regarding the bending moment at the connections. To this end, an additional set of interior facets is introduced, which represent the interior facets of adjacent elements at the locations of the connections, denoted by Λ_j. Subsequently, the interface condition regarding the moments at the connections, are weakly forced through an additional term in the bilinear form.

Including the interface conditions at the connections, the complete bilinear form is given by

$$\begin{aligned}\hat{B}_h([\phi,\eta_h],[w_h,v_h]) = \quad & \big(\nabla\phi_h,\nabla w_h\big)_{\Omega,h} \quad + \\ & \beta_h\big((g\eta_h - i\omega\phi_h),(v_h+\alpha_f w_h)\big)_{\Gamma_{fs,h}} \; + \; \big(i\omega\eta_h - \mu_1\eta_h - \frac{\mu_2}{g}\phi_h, w_h\big)_{\Gamma_{fs,h}} \quad + \\ & \Big(\big((-\omega^2\alpha_{b1}+g)\eta_h - i\omega\phi_h\big), v_h\Big)\Gamma_{str,h} \; + \; \big(i\omega\eta_h, w_h\big)_{\Gamma_{str,h}} \quad + \\ & \big(\alpha_{b2}\Delta\eta_h, \Delta v_h\big)_{\Gamma_{str,h}} \quad - \\ & \alpha_{b2}\Big(\big(\{\Delta\eta_h\},[\nabla v_h\cdot\vec{n}_\Lambda]\big) + \big([\nabla\eta_h\cdot\vec{n}_\Lambda],\{\Delta v_h\}\big)\Big)_{\Lambda_{str,h}} \quad + \\ & \frac{\gamma_m}{h}\Big(\big([\nabla\eta_h\cdot\vec{n}_\Lambda],[\nabla v_h\cdot\vec{n}_\Lambda]\big)\Big)_{\Lambda_{str,h}} \quad + \\ & \frac{k_r}{\rho_w}\Big(\big([\nabla\eta_h\cdot\vec{n}_{\Lambda_j}],[\nabla v_h\cdot\vec{n}_{\Lambda_j}]\big)\Big)_{\Lambda_{j,h}}\end{aligned} \tag{3.26}$$

Ultimately, the full numerical domain and FE spaces are constructed with Gridap; where linear Lagrangian FEs are used as reference elements (see section B.3 and B.4). To find a solution for the 2D model, the bilinear form as stated above is then solved, where the last row of equation 3.26 weakly forces the conditions at the connections and the third, and second last row weakly forces continuity of the surface elevation gradients between structural elements. The tutorial in appendix D provides the complete instructions to set up the FEM model and to solve the FSI problem with Gridap.

3.2.3 Coercivity

As mentioned earlier, to obtain a solvable problem, the bilinear form should be coercive to avoid numerical instabilities. The formal definition states that a bilinear form is coercive (on a Hilbert space $\mathcal{V}$) if there exists a constant $0 < \gamma < \infty$ such that

$$\gamma\,||u||_{\mathcal{V}}||u||_{\mathcal{V}} \leq |b([u,u])| \tag{3.27}$$

For the full domain to be coercive, coercivity at the free surface should to be guaranteed. Accordingly, Akkerman et al. [27] introduced the monolithic weak formulation regarding a 2D fluid domain, which contains additional terms to the weight function v for the free surface condition such that:

$$B([\phi,\eta][w,v]) = \big(\nabla\phi,\nabla w\big)_\Omega \; + \; \beta_h\big((g\eta - i\omega\phi),(v+\alpha_f w)\big)_{\Gamma_{fs}} \; + \; \big(i\omega\eta, w\big)_{\Gamma_{fs}} \tag{3.28}$$

Remark. *In the bilinear form as described above, the terms for the conditions at the fluid-structure interface (Γ_{str}, Λ_{str} and Λ_j) and the damping zones are left out for convenience.*

Considering the formal definition of a coercive system, next, the weight functions w and v are substituted in the altered bilinear form to replace the expressions for ϕ and η such that:

$$\begin{aligned} B([w,v][w,v]) =& \big(\nabla w, \nabla w\big)_\Omega + \beta_h\big((gv - i\omega w),(v + \alpha_f w)\big)_{\Gamma_{fs}} + \big(i\omega v, w\big)_{\Gamma_{fs}} \\ =& \underbrace{||\nabla w||^2_\Omega}_{\geq 0} + \underbrace{g\beta_h||v||^2_{\Gamma_{fs}}}_{\geq 0} + \beta_h g\alpha_f(v,w)_{\Gamma_{fs}} - \beta_h i\omega(v,w)_{\Gamma_{fs}} - \\ & \underbrace{\beta_h i\omega\alpha_f||\nabla w||^2_{\Gamma_{fs}}}_{\geq 0} + i\omega(v,w)_{\Gamma_{fs}} \end{aligned} \tag{3.29}$$

This results in a bilinear form which contains expressions of the weight functions in terms of the corresponding norms and the innerproducts over the domain and the free surface. Regarding the innerproducts, the following should apply to obtain the expression for α_f for which the system is coercive:

$$(v,w)_{\Gamma_{fs}}\Big[\beta_h g\alpha_f - \beta_h i\omega + i\omega\Big] = 0 \qquad \rightarrow \qquad \alpha_f = \frac{-i\omega}{\beta_h g}\big[1 - \beta_h\big]$$

Using this expression for α_f, the value for β_h can be obtained, such that the statement of equation 3.27 is satisfied and coercivity on the free surface has been proven. Accordingly, the model is determined to be stable for $\beta_h = 0.5$ [27].

3.3 Model Validation

The validation of the model is assessed by reproducing results obtained by Riyansyah et al. [18], who in turn compared the outcome of their computations with the results obtained by Khabakhpasheva and Korobkin [28]. The set up of the model introduced by Riyansyah et al. [18] is illustrated in figure 3.3, where the input conditions of the numerical models used by both of the aforementioned researchers are presented in Table 3.1.

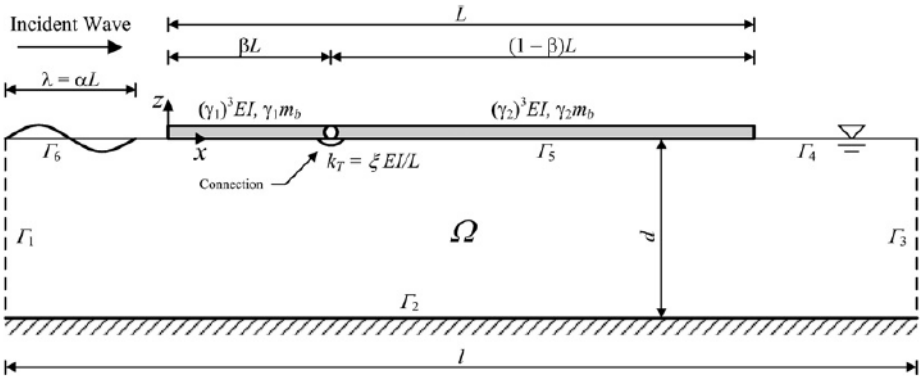

Figure 3.3: Numerical model of Riyansyah et al. [18]

Looking at the numerical simulations performed in both studies, the normalized deflection was obtained over the length of a system consisting of two floating beams, with the front beam having greater bending stiffness than the rear beam. Subsequently, the results were computed for two types of connections, namely a simple hinge and a rigid connection.

Table 3.1: Input numerical model of Khabakhpasheva and Korobkin [28], used by Riyansyah et al. [18]

Parameter	Symbol	Magnitude
Total length of the beam	L	12.5 m
Mass density of beam system	m_b	8.36 kg/m
Flexural rigidity	EI_1, EI_2	47 100 Nm, 471 Nm
Beam 1 flexural rigidity parameter	γ_1	1
Beam 2 flexural rigidity parameter	γ_2	1
Connection location parameter	β	0.20
Connection rotational stiffness parameter	ξ	0 and 625
Fluid domain length	l	25 m
Water depth	d	1.1 m
Wavelength-to-beam length ratio	α	0.249

As shown in figures 3.4a and 3.4b, the results obtained by the model built using *Gridap* (see lower figures), seem to agree well with the results produced by Riyansyah et al.[18], and Khabakhpasheva and Korobkin [28] (see upper figures).

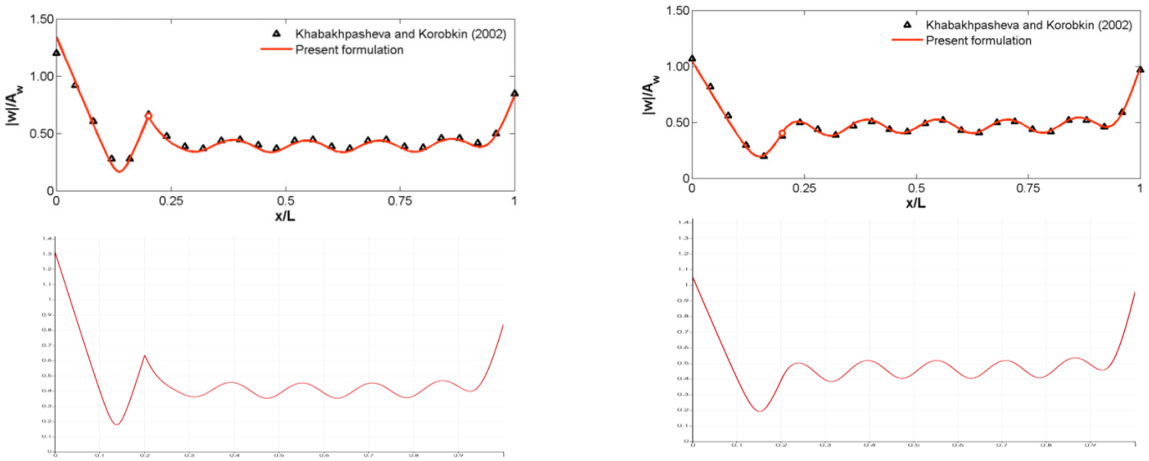

(a) hinge, $\xi = 0$

(b) semi rigid, $\xi = 625$

Figure 3.4: Test runs - replication of results by Riyansyah et al. [18]

4
Results of Hydroelastic Analysis

In this chapter, the results of the hydroelastic analysis are discussed. First, to get a global overview of the effects of varying the bending stiffness of the beams and the rotational stiffness in the connections, the vertical displacements and bending moments are computed over the total length of the VLFS. The variations in the bending stiffness and the rotational stiffness are defined by different values of the parameters γ_1 and ξ, respectively. Accordingly, the normalized vertical displacement amplitude and the bending moment distribution are obtained for nine different combinations of the two stiffness quantities. These effects are discussed in section 4.2, based on the results shown in appendix C. In this part of the analysis, three different type of modules (i.e. flexible, semi-rigid, and rigid) and three types of rotational springs (i.e hinge, semi-rigid, and rigid) are considered, where the results are obtained for four different wavelength-to-beam length ratios.

The first part of the analysis shows that by altering the bending stiffness and rotational stiffness, the vertical displacement can be reduced. However, this may have a negative effect on the maximum bending moment. To gain more insight into this trade-off between minimizing the displacement and the bending moments, contour plots have therefore been plotted in section 4.3; this visualizes the maximum displacement and the maximum moments, taking into account a range of values for both stiffness quantities.

4.1 Input Parameters

To perform the hydroelastic analysis, the incident wave conditions need to be determined, together with some initial values for the material properties of the structure. For the analysis considering the normalized displacement and moments distributions along the structure, the input parameters are summarized in table 4.1. The input parameters used in the analysis regarding the maximum displacements and maximum moments are summarized in table 4.2.

With respect to the input parameters of the structure, the beams are considered to have a height of 2m. The initial value of the Young's modulus is set to 12 GN/m^2, with a corresponding density of 250 kg/m^2 unit per width. As mentioned in section 2.1, the proportionally between the mass and the bending stiffness is included through the bending stiffness parameter γ_1, where the mass is defined by $\gamma_1 \rho_b h_b$ and the bending stiffness by $\gamma_1^3 EI$. Moreover, the rotational stiffness of the springs is defined by $\xi EI/L$. Accordingly, to analyse the effects of varying the bending stiffness, different values of bending stiffness parameter γ_1 are considered; Similarly, the analyses are performed for different values for the rotational stiffness parameter ξ.

4.1.1 Incident wave conditions

As discussed in chapter 2, the model is based on the linear wave theory. Therefore, relatively mild wave conditions will be considered for the incident wave. Moreover, it is assumed that VLFS is subject to monochromatic waves. These conditions correspond to swell waves, which typically have a wave period around 10 seconds [22]. Figure 4.1 shows a graph which indicates the regions of validity for

different wave theories. Hence, the hydroelastic analysis is performed using the following wave conditions, while assuming a wave period T = 10 seconds and considering the relations as defined in figure 4.1:

wave height: H = 1.25 m wave period: T = 10 s water depth: d = 30 m

With these values for the incident wave period and the water depth, the incident wave length is calculated, using the wave dispersion relation:

$$\omega = \frac{2\pi}{T} \quad \rightarrow \quad \lambda = \frac{gT^2}{2\pi} \tanh \frac{2\pi d}{\lambda} = \frac{9.81 \cdot 10^2}{2\pi} \tanh \frac{2\pi \cdot 30}{\lambda} \approx 140\,\text{m}$$

It was already mentioned in section 1.2 that the response of the system is influenced by the ratio between incident wave length and the length of the structure, which is defined by the parameter α. Hence, the analysis will be performed for different values of α, by varying the length of the structure.

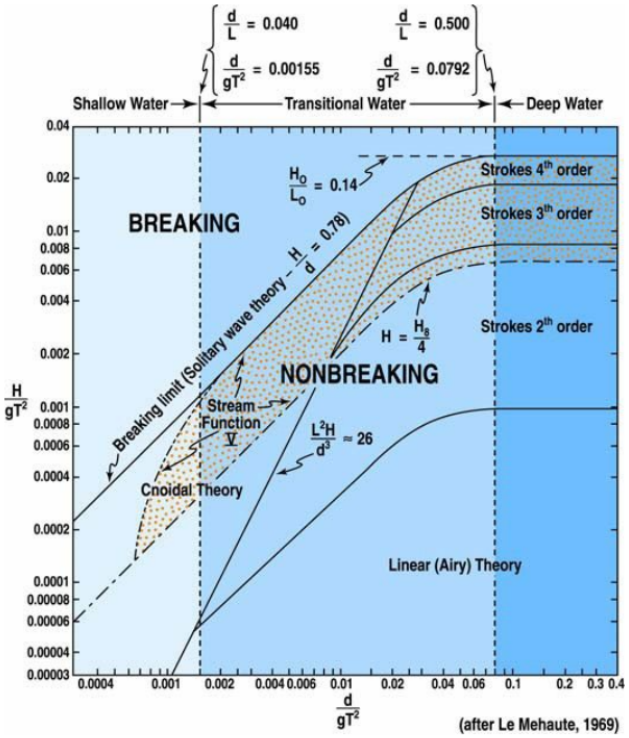

Figure 4.1: Indication for the validity of wave theories [29]

4.2 Numerical Results: Displacements & Moments along Structure

To get a global overview of the hydroelastic response to different values of the stiffness parameters and wavelength-to-beam-length ratios, first, the normalized vertical displacement and moment distribution are plotted over the length of the structure; using the input parameters as summarized in table 4.1.

In appendix C, figures C.1, C.3, C.5, and C.7 show the numerical results of the normalized vertical displacement amplitude along the structure, for four different values of the wavelength-to-beam-length ratio α. For each value of α, the figure contains nine sub-figures, showing the results for nine different combinations of γ_1, i.e. the bending stiffness of the beam elements, and ξ, i.e. the rotational stiffness of the connections. In each row the three different values of γ_1 increase from the right sub-figure to the

left one, while for each column the three different values of ξ increase from the top sub-figure to the bottom one. The moment distributions along the structure are presented in a similar way in figures C.2, C.4, C.6, and C.8, for the same combinations of values for γ_1, and ξ.

Table 4.1: Input parameters model - numerical results along the structure

Parameter	Symbol	Magnitude
Total length of the structure	L	300 m, 500 m, 1000 m, 2000 m
Height of the structure	h_b	2 m
Density of beam system	ρ_b	250 kg/m^3
Young's modulus	E	12 GN/m^2
Bending stiffness parameter	γ_1	0.2, 1.0, 2.0
Connection location parameter	β	0.25
Connection rotational stiffness parameter	ξ	0, 6, 650
Fluid domain length (ext. damping zones)	l	2 x L
Water depth	d	30 m
Wave amplitude	A_w	0.75 m
Wavelength-to-beam length ratio	α	0.47, 0.28, 0.14, 0.07

4.2.1 Effects on normalized vertical displacement

The effects on the normalized vertical displacement amplitude are discussed here for each variable. Overall, the maximum displacements are located at the free ends for the majority of the structures, where the results show that the relation between the system's response and the varying material properties is non-linear.

Effects of varying rotational stiffness
The hydroelastic response of the interconnected structure approaches the response of a continuous structure when the rotational stiffness of the connections increases. This effect is clearly visible in all figures C.1, C.3, C.5, and C.7, when the top row of sub-figures is compared with the bottom row; in the sub-figures for $\xi = 650$, the locations of the connections are difficult to trace.

In general, when the rotational stiffness decreases, the normalized vertical displacement around the connections increases. This can be seen in the sub-figures for $\xi = 6$ and $\xi = 0$, showing clear spikes at the connection points. For any value of α, it appears that there is no significant difference in the normalized displacement for flexible modules ($\gamma_1 = 0.2$), when combined with hinges or semi-rigid connections. However, figures C.3g, C.5g, and C.7g show that the use of rigid connections does affect the response of flexible modules for the three smallest values of α; although the average value of the normalized displacement remains the same, the rigid connections (in addition to a decrease in the vertical response at the connection points) also cause a decrease in the fluctuations of the normalized vertical displacement over the entire structure. This effect is strongest for the structure with $\alpha = 0.28$ (see figure 4.2), where the rigid connections result in an almost constant value for the normalized displacement amplitude over the entire length.

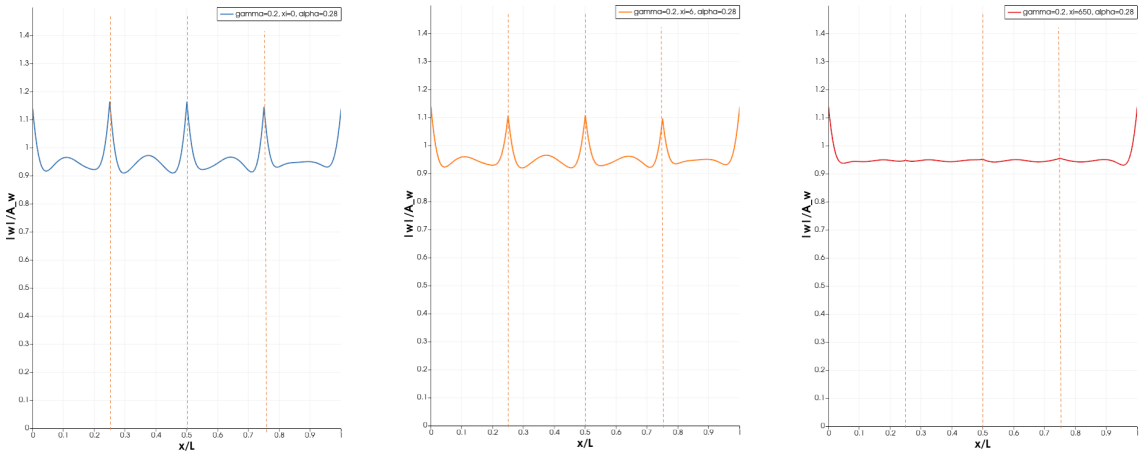

(a) $\gamma_1 = 0.2$, $\xi = 0$ (b) $\gamma_1 = 0.2$, $\xi = 6$ (c) $\gamma_1 = 0.2$, $\xi = 650$

Figure 4.2: Effect of different type of connections on flexible structures ($\alpha = 0.28$)

Effects of varying bending stiffness
Regarding the stiffness of the modules, it can be seen that increasing the bending stiffness reduces the normalized vertical displacement along the structure. Moreover, for the stiffest modules, combined with hinges or semi-rigid connections, the response tends to gradually decrease towards the downstream side. Yet, the maximum normalized displacements at upstream free ends are often larger for (semi-)rigid modules with hinged connections, compared to flexible ones. The structures with flexible modules tend to follow the natural harmonic shape of the incoming wave and clearly show the response associated with a continuous structure.

Although the maximum vertical response along the structure is generally reduced by increasing the stiffness, the gradient of the vertical displacement becomes larger, where this effect is strongest for stiffer modules with hinged connections. An example of this effect caused by increasing the bending stiffness is given in figure 4.3, for a structure with hinged connections and a wavelength-to-beam-length ratio of $\alpha = 0.14$.

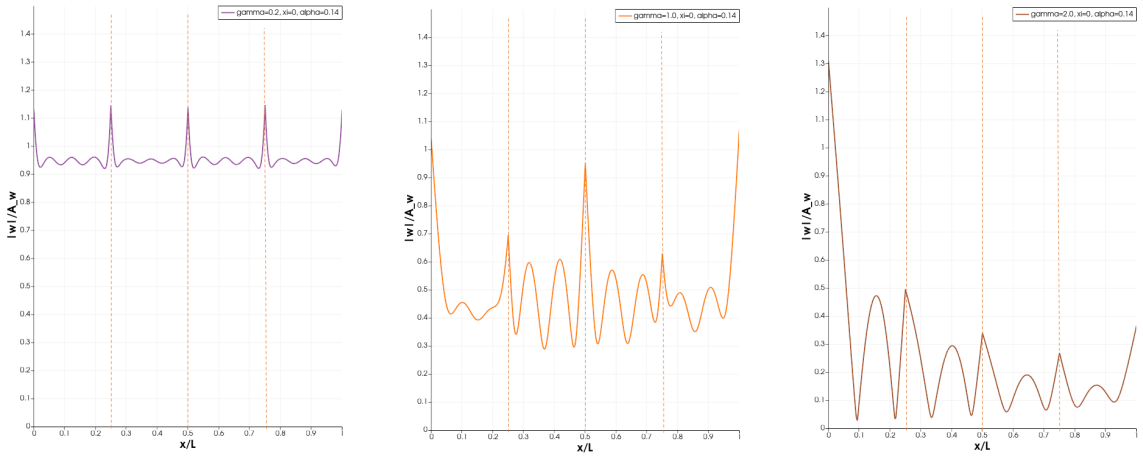

(a) $\gamma_1 = 0.2$, $\xi = 0$ (b) $\gamma_1 = 1.0$, $\xi = 0$ (c) $\gamma_1 = 2.0$, $\xi = 0$

Figure 4.3: Effect of increasing beam stiffness for structure with hinge connections ($\alpha = 0.14$)

Effects of varying wavelength-to-beam-length ratio
As the length of the modules increases, the value for α becomes smaller, resulting in a more oscillating response along the structure. It can be seen that the local deflections along the structure therefore become more significant.

Whether the (semi-)rigid structures react more as rigid modules or as a continuous system is - in addition to the type of connections - also influenced by the ratio between the wavelength and the length of the structure. Looking at the largest value for α, the wave length is approximately 2 times larger than the length of an individual beam element. The results regarding this ratio show that the beams behave more as rigid modules, especially for the stiffer structures with a lower rotational stiffness. The same holds for $\alpha = 0.28$, where the incoming wave is approximately the length of an individual beam. However, when the wave length becomes smaller than the length of an individual beam (i.e. lower two values of α), the response shows more oscillating behaviour along the structure, also for structures with a high bending stiffness. An example of this change in the type of response is illustrated in figure 4.4, for a structure with high bending stiffness and semi-rigid connections.

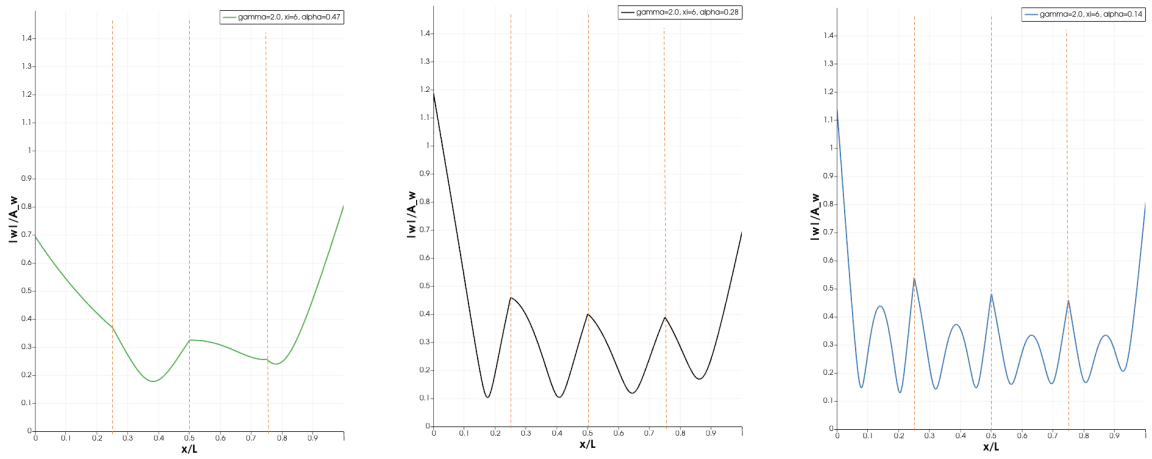

(a) $\alpha = 0.47$ (b) $\alpha = 0.28$ (c) $\alpha = 0.14$

Figure 4.4: Effect of wavelength-to-beam-length ratio ($\gamma_1 = 2.0$, $\xi = 6$)

4.2.2 Effects on bending moment

The moment distributions along the structure are presented in figures C.2, C.4, C.6, and C.8. For the design of VLFSs, it is important to consider the maximum bending moment. As mentioned in section 1.3, there is a trade-off between the minimum vertical displacement and the maximum moments that occur. Equation 2.16 shows that the moment is defined as the second derivative of the displacement multiplied by the bending stiffness. Therefore, increasing the bending stiffness evidently increases the moments in the structure, which is visible in all the results shown in appendix C. Yet, it appears that for larger values of α, the increase in bending moment between semi-flexible and rigid modules with hinged connections is minimal.

Regardless of the wavelength-to-beam-length ratio or the rotational stiffness of the connections, it can be seen that there is no difference in the maximum moments for the flexible modules. The only effect that the rotational stiffness has on the moment distribution is that for the structures with hinges, the moments at the connections converge to zero.

For both the semi-flexible and rigid modules, it appears that increasing rotational stiffness of the

connections reduces the maximum bending moment, when looking at the results for $\alpha = 0.14$ and $\alpha = 0.07$. This effect is larger for higher bending stiffness. On the contrary, increasing the rotational stiffness leads to an increase in the maximum bending moment, for the structures subject to the larger wavelength-to-beam length ratios.

4.3 Numerical Results: Maximum Displacements & Moments

The results presented in appendix C give a good impression of the behaviour of the VLFS for the different combinations of stiffness and wavelength ratios and they show the strong coupling between the different variables and the response of the structure. However, an unambiguous distinction is difficult to make regarding the most effective contribution of each individual variable.
Therefore, the maximum normalized vertical displacement and maximum moment are represented by contour plots, plotting the bending stiffness against the rotational stiffness. To visualize how the bending stiffness of the structure and the rotational stiffness of the connections relate to each other in terms of their influence on the response of a multi-module VLFS.

The input parameters used for this part of the analysis are summarized in table 4.2. The results are obtained for values in which the two stiffness variables range from flexible to rigid. Accordingly, values for the bending stiffness parameter vary from $\gamma_1 \in [0.1, 3.0]$, while for the rotational stiffness parameter values are considered for $\xi \in [0.001, 650]$.

The results from the previous section showed that the largest shift in structure behaviour occurred at the transition from wavelengths longer than the length of an individual beam to wavelengths shorter than a single beam. Therefore, the results are obtained with respect to $\alpha = 0.28$ and $\alpha = 0.14$ in this part of the analysis, when considering the effects of varying wavelength-to-beam length ratios.

Table 4.2: Input parameters model - numerical results contour plots

Parameter	Symbol	Magnitude
Total length of the structure	L	500 m, 1000 m
Height of the structure	h_b	2 m
Density of beam system	ρ_b	250 kg/m^3
Young's modulus	E	12 GN/m^2
Bending stiffness parameter range	γ_1	0.1 - 3.0
Connection location parameter	β	0.25
Connection rotational stiffness parameter range	ξ	0.001 - 650
Fluid domain length (ext. damping zones)	l	2 x L
Water depth	d	30 m
Wave amplitude	A_w	0.75 m
Wavelength-to-beam length ratio	α	0.28, 0.14

4.3.1 Contour plots - maximum normalized vertical displacement

For both values of α, the results in figures 4.5 and 4.6 show that when ξ is greater than 130, applying a higher rotational stiffness has no further effect on the maximum vertical displacement.
For structures with rigid connections it is clear that the largest displacements are found for (semi-)flexible modules where the largest displacements appear for $\gamma_1 \approx 0.65$. Although the results for $\xi > 130$ show that increasing the beam stiffness generally reduces the maximum displacement, this trend is not consistent. For $\xi > 130$, the minimum normalized displacement is found at $\gamma_1 \approx 2.5$ for $\alpha = 0.28$, and $\gamma_1 \approx 2.8$ for $\alpha = 0.14$. However, in both cases, a higher value for the bending stiffness does not further lead to a reduction of the maximum displacement.

The non-linear relation between the response of the system and the different stiffness quantities becomes very clear when zooming in on the results for $\xi < 15$. Looking at the left contour plot of figure 4.5, for a value of $\xi \approx 1.5$ the minimum displacement is found in combination with a bending stiffness of $\gamma_1 \approx 1.5$, while for the same value of ξ the largest displacement occurs when the bending stiffness is increased to $\gamma_1 \approx 2.8$.
The same effect occurs when analysing the relation from the other axis. Now looking from left to right, the plot shows that for the value of $\gamma_1 \approx 2.8$, combined with $\xi \approx 1.5$ would result in the maximum normalized displacements, while for the same γ_1, increasing ξ leads to a minimum value of normalized displacement.

Also, the difference in the results for the two wavelength-to-structure ratios is greater for $\xi < 15$. For $\alpha = 0.28$, the combination of $\xi \approx 1.5$ with very high values of γ_1 result in maximum displacements, while this is the opposite for $\alpha = 0.14$, where a structure with flexible modules (i.e. $\gamma_1 \approx 0.7$) will cause the largest maximum displacements.

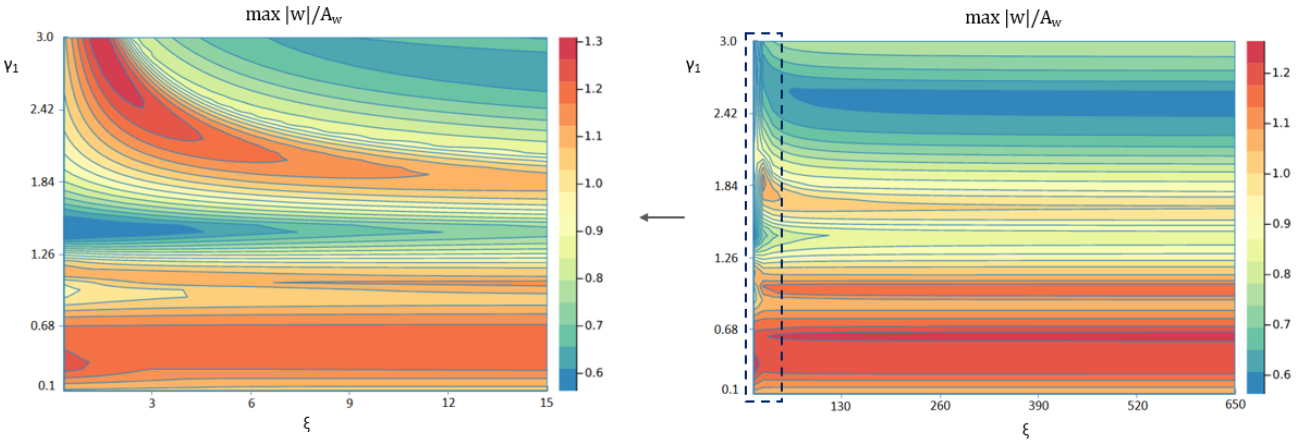

Figure 4.5: Contour plot - maximum normalized displacement ($\alpha = 0.28$)

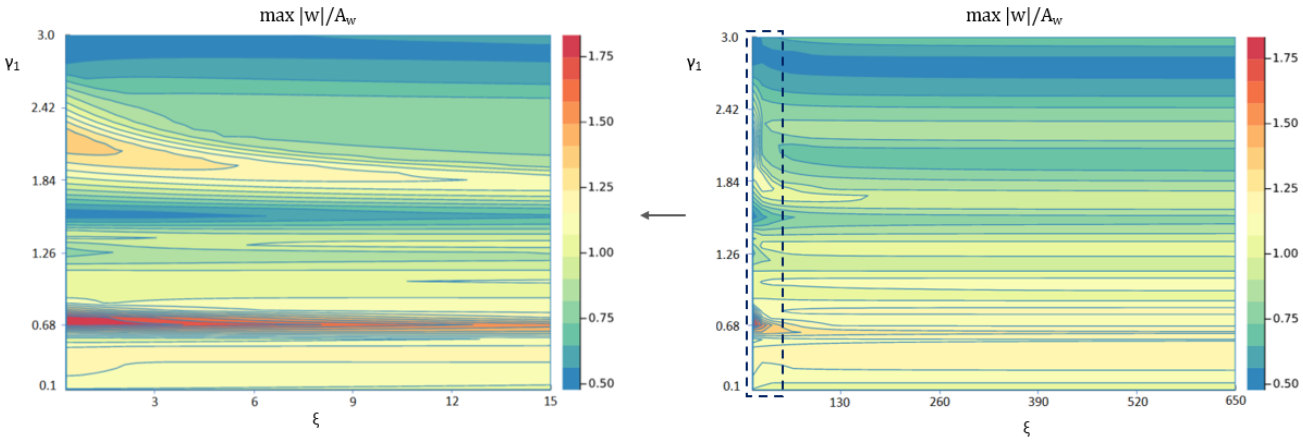

Figure 4.6: Contour plot - maximum normalized displacement ($\alpha = 0.14$)

4.3.2 Contour plots - maximum bending moment

Regarding the maximum bending moments, the contour plots in the figures 4.8 and 4.7 show a more steady increasing trend. Similar to the results discussed in the previous section, it can be seen that for

higher values of the bending stiffness the maximum displacement will be reduced, but at the expense of the maximum bending moment.

Overall, the impact of increasing the rotational stiffness seems already negligible values of $\xi > 65$. However, for $\alpha = 0.14$, increasing the stiffness of the connections, may have some reducing effects on the maximum bending moments for stiff(er) modules. Furthermore, there are some interesting observations to point out when comparing the maximum bending moments for $\xi < 15$, with those results of the vertical displacements. For $\alpha = 0.28$ the smallest maximum displacements appear to be in the range of $\gamma_1 \in [2.5, 3.0]$ with $\xi \in [6, 15]$, or in the range of $\gamma_1 \in [1.3, 1.6]$ with $\xi \in [0.001, 3.0]$. However, where the first range of variables is indeed associated with the highest values for the maximum bending moment in the contour plot, the maximum bending moment is relatively low for the range of semi-rigid modules with flexible connections.
A similar observation applies to $\alpha = 0.14$, where it is interesting to see that both $\gamma_1 \approx 1.6$ and $\gamma_1 > 2.5$, combined with low values of ξ, results in minimum normalized displacements. Yet, increasing γ_1 to approximately 2.8 leads to a significant increase in the maximum bending moment, while for $\gamma_1 \approx 1.6$ the maximum bending moment stays relatively low.

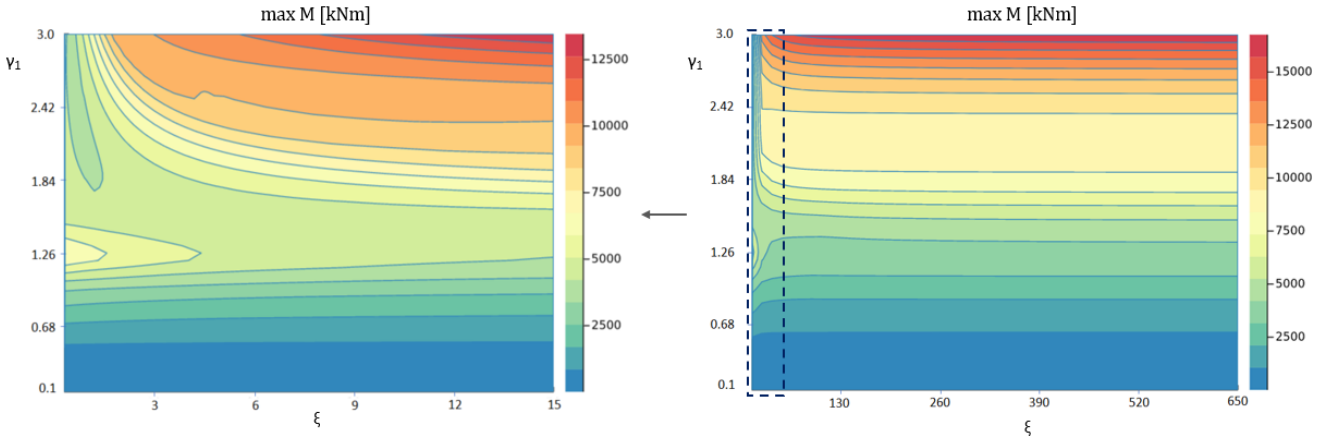

Figure 4.7: Contour plot - maximum bending moment ($\alpha = 0.28$)

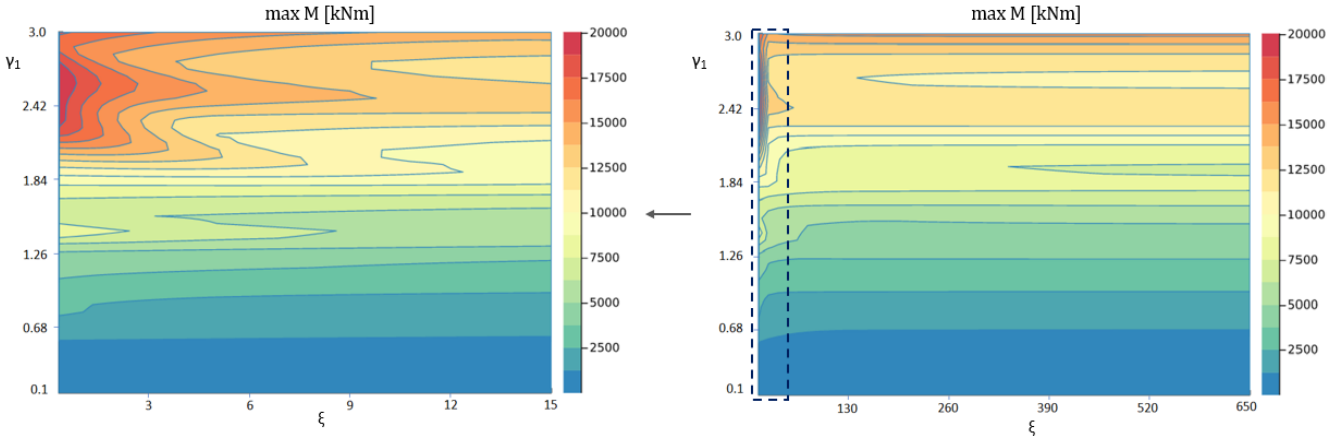

Figure 4.8: Contour plot - maximum bending moment ($\alpha = 0.14$)

4.4 Optimal Combinations of the Stiffness Parameters

Based on the contour plots as shown in figure 4.9, a bending stiffness parameter of $\gamma_1 \in [1.3, 1.7]$, combined with a value for the rotational stiffness parameter of $\xi \in [0.001, 5.0]$, results in the most optimal combinations of the stiffness quantities for both wavelength-to-structure ratios. Considering the input parameters, this is corresponds with a bending stiffness of 17.5e9 - 39.5e9 Nm, together with a rotational stiffness of 17500 - 23.7e7 Nm, depending on the structure length. Accordingly, these values would result in a maximum normalized vertical displacement amplitude of approximately 0.6, and a maximum bending moment around 7500 kNm, while the system is subject to mild wave conditions, with a corresponding wavelength of 140m.

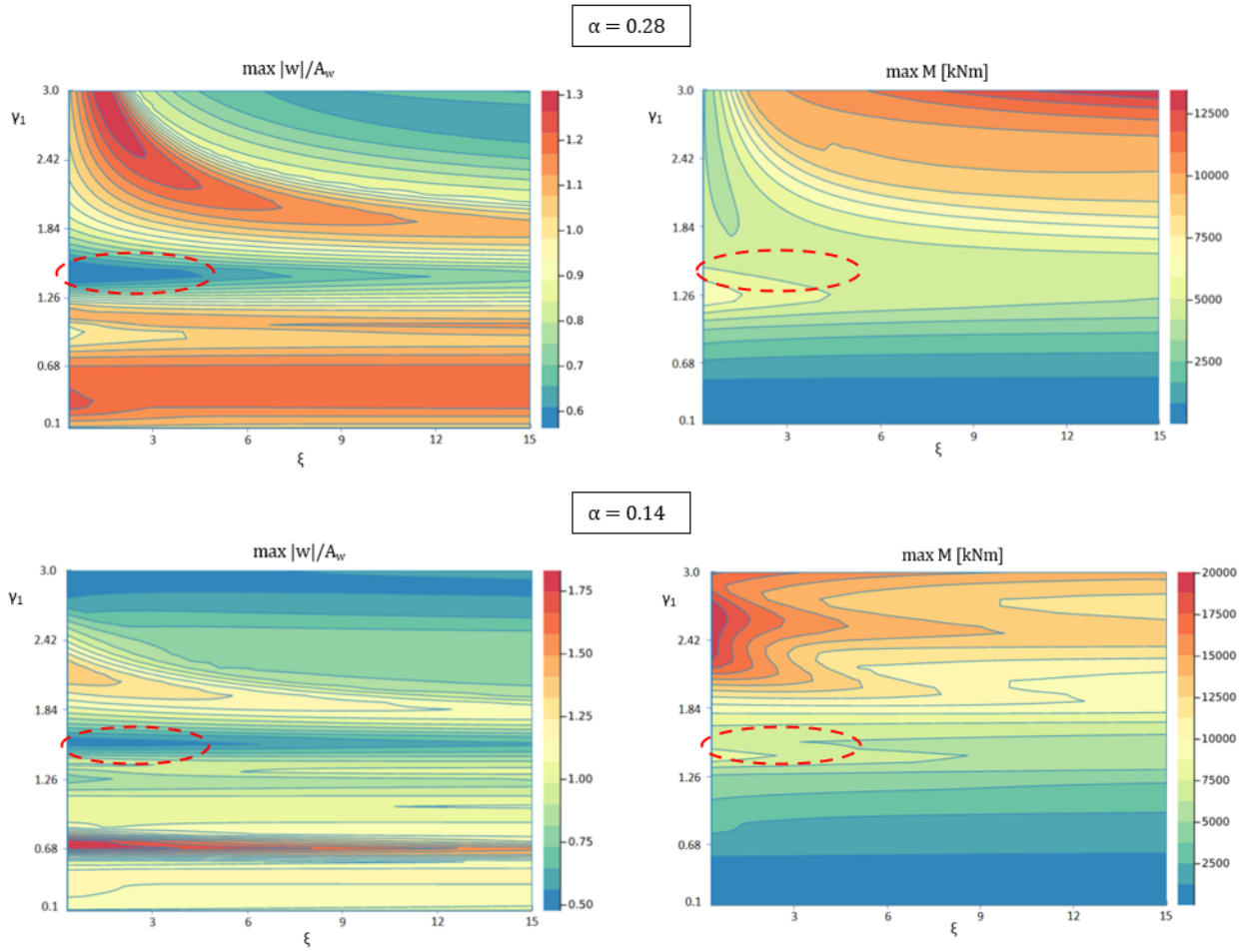

Figure 4.9: Optimal range for γ_1 and ξ

4.5 Summary of Results

The structure approaches the response of a continuous system, when the rotational stiffness increases. Increasing the beam stiffness has a (gradual) reducing effect on the maximum normalized vertical displacement amplitude, but at the same time causes an increase in the maximum bending moment. Moreover, as the wavelength becomes larger than an individual beam, the structure is more likely to behave as rigid modules, while the oscillating response becomes more significant when the wavelength is shorter than the length of a single beam.

For flexible modules, the results show that applying hinged or semi-rigid connections does not have a significant effect on minimizing the normalized vertical displacement amplitude of the structure. The maximum bending moment also stays constant when increasing the rotational stiffness. Structures with a moderate to high bending stiffness - for which the wavelength is shorter that an individual beam - the maximum bending moment is reduced when the rotational stiffness becomes larger. On the contrary, increasing the rotational stiffness leads to an increase in the maximum bending moment, for $\alpha = 0.28$, when $\gamma_1 > 1.8$.

The contour plots in figures 4.5 to 4.8 show that for $\xi > 130$, increasing the rotational stiffness has no further effect on the response of the system. However, for $\xi < 15$, the effect on the system's response for different combinations of the quantities varies widely. Based on the aspects considered in this analysis, an optimal combination was found with respect to a bending stiffness parameter of $\gamma_1 \in [1.3, 1.7]$, combined with a value for the rotational stiffness parameter of $\xi \in [0.001, 3.0]$.

5 Discussion

In this chapter, an attempt is made to explain some of the occurring phenomena and to further elaborate on the presented effects, which includes the transition between rigid-module and continuous behaviour of the structure, and the effect of applying certain type of connections. Moreover, the results show a peak in the maximum displacement for specific combinations of the material properties. The natural frequency of the system is therefore discussed, as this plays an important role in the occurrence of resonance. In addition, the applied mathematical formulation of the problem statement and the implementation of the FEM model are evaluated, where the impact of the assumptions made is discussed.

5.1 Interpretation of Numerical Results

The overall behaviour of the VLFS seems in line with initial expectations. When increasing the rotational stiffness, the structure approaches the response of a continuous system. The maximum normalized displacement is reduced when increasing the bending stiffness, but this simultaneously cause an increase in the bending moment. Moreover, as the wavelength becomes larger than an individual beam, the system is more likely to behave as rigid modules, while the local displacement becomes more significant when the wavelength is shorter than the length of a single beam.

Non-linear relation to varying material properties
Although the system is assumed to be linear, the results show that the relation between the response of the system and the varying material properties is non-linear. This can be explained by the fact that the total general solution of the dynamic response of (slender) structures consists of two parts; the particular solution and the homogeneous solution. The particular solution ensures that the response of the structure corresponds with the excitation of the external force in the steady-state. The homogeneous part of the solution determines the natural response of the system, while it satisfies the boundary conditions of the structure. The natural response and the amount of influence that the boundary conditions will have on the behaviour of the structure are determined by the material properties. For example, the results clearly show that the influence of the connections on the response is much more local for certain structures. As this dependence is non-linear, it can therefore differ greatly for specific combinations of the stiffness quantities.

Transition between rigid modules and continuous system
Figures C.3b and C.3e show some interesting results when looking at the normalized displacements along the structure. For this combination of variables, the outer beams seem to behave more like rigid modules, whereas the two beams in the center show more continuous behaviour. This 'hybrid' behaviour in one structure may be explained by the presence of the connections in combination with its semi-flexible character. It clearly demonstrates the sensitivity of the system and the fact that excluding the elasticity in the analysis can lead to inaccurate results.

Decrease in normalized vertical displacement amplitude
The phenomenon that for stiffer modules with hinged or semi-rigid connections, the normalized displacements tend to decrease towards the leeward side can be explained by the fact that it is more difficult to deform a structure with a higher bending stiffness. This causes an attenuation effect, which influences the transmitted wave as it travels along the structure. Interesting is to see that this attenuation effect also occurs for the largest flexible structures. Although this behaviour is less expected for flexible structures, similar behaviour was recently detected during another the MSc project regarding Very Flexible Floating Structures [30].

Effects of rotational stiffness on reducing bending moment
It was concluded that for (semi-)rigid modules, where the wavelength is shorter that an individual beam, the maximum bending moment is reduced when the rotational stiffness becomes larger. In general, the maximum "field" bending moment along a continuous beam is smaller when the structure is clamped on both sides, compared to a simply supported beam. Increasing ξ (i.e. shifting from a simply supported beam to a clamped-clamped beam) will therefore cause a reduction of the bending moment, when the structure mainly behaves continuously.
However, this response differs for structures which behave more as rigid modules. Hence, when α is large, combined with a larger the bending stiffness, increasing the rotational stiffness causes an increase in the moments at the connections. Accordingly, in figures C.2, C.4f and C.4i, it can be seen that the peak of the occurring moment shifts towards the connection.

The natural frequency of the system and the occurrence of resonance
Looking at the results in the left contour plot of figure 4.6, it can be seen that the maximum normalized displacement for $\alpha = 0.14$ occurs at $\gamma_1 \approx 0.68$. As this maximum appears for a quite specific range of γ_1, it may be caused by (local) resonance. Resonance occurs when the frequency of the incident wave is equal or close to a natural frequency of the VLFS, where the natural frequency of the system is determined by its mass, bending stiffness, and length. For an unsupported beam with free ends, the first natural frequency is defined by $\omega_0 = \frac{22.37}{L^2}\sqrt{\frac{EI}{\rho_b A}}$. Considering the results of $\alpha = 0.14$, for $\gamma_1 = 0.68$, the natural frequency for a single beam (with L=250) is $\omega_0 \approx 0.9$. Since the frequency of the incident wave is equal to $\omega = 0.62$, this extreme value for the maximum normalized displacement could be a result of resonance. In addition, an attempt was made to find a more accurate approximation of the system's natural frequency, using the FEM model. Unfortunately, due to limited computer power (and time), this has not led to more valuable insights.

Future implementation of results
The visualization by means of contour plots seems to be a valuable method to obtain information for optimizing the design. However, it must be taken into account that in the contour plots information about the location of the occurring values is lost. For the maximum bending moments, this is not much of a problem; as the beams are uniform and are therefore designed to the maximum required capacity, regardless of the occurring location along the structure. For the vertical displacement, however, this information is important for the design. Yet, in combination with graphs visualizing the response along the structure, these contour plots allow to obtain good interpretations regarding the most effective combinations of the stiffness for the different components.

As the results for the normalized vertical displacements are dimensionless, these results can therefore be considered in relation to different wave amplitudes, provided that the wave characteristics are still considered linear. The results for the maximum bending moment are not dimensionless and it should therefore be taken into account that these results may differ when changing the incident wave conditions.

5.2 Assumptions Mathematical Formulation

To reduce the complexity of the analysed system, it can be very useful to make certain assumptions. Yet, it is important to realize that both these simplifications and the decisions regarding the implementation of numerical methods will have an influence on the accuracy of the physical problem.

Linear wave theory
The model is based on the linear wave theory. Therefore, the quadratic, non-linear terms in the equations of motion of the fluid, the kinematic, and dynamic boundary conditions are neglected. Non-linear aspects are for instance the large-scale effects of bottom friction, very steep/breaking waves or the effects when the structure will not always be in contact with the water. Moreover, it is important that a structure is designed with extreme conditions in mind, where their probability of occurrence corresponds to a design return period. Increasing the amplitude to these extreme cases causes the input conditions for the incident wave to fall outside the validity range of the linear wave theory.

Although taking into account these non-linear effects would indeed increase the accuracy of the solution, the mathematical analysis of non-linear wave equations is far more complex and no general analytical method exists for their solution. Since the largest contribution to the complete solution is given by the first-order components of the equations and including non-linear terms is computationally costly, developing a model based on the linear wave theory seems plausible to obtain valid approximations of the hydroelastic response for preliminary designs. Also, in practice, models based on linear wave theory are frequently applied and still appear to provide a good approximation even for input values that fall outside this range.

Constant water depth
The water depth in the model is assumed to be constant. Although the magnitude of the effect also depends on the water depth considered, there are studies showing that neglecting seabed topography may have some influence on the hydroelastic response, as there may be a slight increase in plate bending due to the presence of a variable depth profile [31]. Since the numerical model developed for this thesis makes it possible to implement different water depth profiles in the analysis, it would be interesting to take this into account in future research.

2D model
Looking at the structural characteristics, the multi-module VLFS is schematized as floating beams, based on the Euler-Bernoulli beam theory. This simplification allowed the development of the numerical model in 2D. Besides the advantage of reducing the computation time, the selection of 2D made it easier to represent the results, i.e. the dependence on 3 variables, through the use of contour plots. The use of a 2D model therefore served the necessary purpose with regard to the considered research objective, where it has given better insight into the relation between the two stiffness quantities and the wavelength-to-structure ratio. However, when designing a floating structure to create artificial land, it is evident that a 3D model is required. This would also allow to analyse the response for different incident wave angles. Extending the analysis from a 2D to 3D coordinate system can be done with the developed numerical model.

Structural properties VLFS
The cross-section of the beams is assumed to have a solid rectangular shape. In practice, the platforms are more likely to be constructed by two larger load-bearing plates connected by a stabilizing web. This shape is more beneficial, as the change in the second moment of inertia allows to increase the bending stiffness of the platform, without further increasing its mass. However, the proportionally between the mass and the bending stiffness is included in the bending stiffness parameter γ_1, which is derived from the second moment of inertia for a solid rectangular shape. When considering an alternative cross-section, this proportionally should be reconsidered and appropriately adjusted with respect to γ_1. Moreover, it should be taken into account that these changes also has an effect on the natural frequency.

In addition, the structure is assumed to have a uniform cross-sectional area and homogeneous material properties. From a constructional point of view, it is more convenient to keep the dimensions and properties (with respect to the cross-sectional area) the same along the platforms, therefore these assumptions are considered plausible. Although very small variations in the material properties of a structure can never be ruled out, these effects are negligible.

Solution in the frequency domain
Due to the linearity (regarding both the fluid and the structure) the solution is solved in the frequency domain. The advantage of this approach is that by rewriting the problem in frequency dependent functions, the formulation of the EoMs and BCs/ICs ultimately results in an algebraic system of equations, which can then be solved much faster. As a consequence, the solution is only obtained for the steady-state. Hence, when the transient solution of the problem is desired or non-linear effects should be considered in the analysis, the problem needs to be solved in the time domain, at the expense of the faster computational time.

5.3 Assumptions FEM Model

The assumptions made regarding the analytical formulation will form the basis for the FEM model and thus influence the numerical approach. The selection for the Euler-Bernoulli theory results in a weak form containing second-order derivatives with respect to the displacement of the beam. Therefore, additional requirements for the shape functions are required, ensuring C1-continuity across the elements. On other option would have been to describe the behaviour of the beams by the Timoshenko theory. Unlike the Euler-Bernoulli theory, in this theory the deformation of the beam is described by the translational displacement $w(x,t)$, and the angular displacement $\varphi(x,t)$, where these two variables are independent and only mechanically coupled. Regarding its numerical implementation, the weak form based on this theory would only include first-order derivatives, hence, C0-continuity between the elements will hold. While the Timoshenko theory is more generally applicable, the formulation of this theory is also more extensive because the deformation of the beam is defined by two independent variables instead of just one, namely w. In addition, when developing a model based on Timoshenko theory, one has to take into account the occurrence of a numerical instability called shear locking, which compromises the accuracy of the results in the case of pure bending.

To account for the second-order derivatives in the weak form, the combined CG/DC approach is applied, where the C1-continuity is weakly forced between adjacent elements. To guarantee C1-continuity, also the CG approach in combination with elements, such as Hermite polynomials, could have been used. The decision to adopt the CG/DG approach is merely based on the fact that the FE packages of Gridap not yet provided these type of elements at the time.

6 Conclusion

According to the research objective, a 2D FEM model is developed to analyse the hydroelastic response of a multi-module VLFS; in order to investigate how the bending stiffness of the modules and the rotational stiffness of the connections relate to each other in terms of their influence on the response, and what their effect is on the vertical displacement and the bending moment of the system, considering different wave lengths.

The numerical results give a good approximation to the analytical formulation. When increasing the rotational stiffness, the VLFS approaches the response of a continuous system. The maximum normalized displacement is reduced by increasing the bending stiffness, but this will increase the bending moments simultaneously. Moreover, as the wavelength becomes larger than a single beam, the structure tends to behave more like rigid modules. This response shifts towards more continuous behaviour when the wavelength becomes shorter. As some results show both rigid and flexible behaviour within one structure, the assumption to exclude elasticity from the analysis may lead to inaccurate results.

The aim is to design the VLFS such that minimal vertical displacements are obtained, while the maximum bending moment does not exceed the structural capacity. In addition, it is most beneficial to design for a combination of the material properties that favors the widest range of incident wavelengths. In this regard, the most optimal combination appears to be a VLFS consisting of four semi-flexible to semi-rigid modules, combined with hinges or connections with moderate rotational stiffness, according to the aspects considered in this hydroelastic analysis.

However, the results show that the influence of different combinations of the two stiffness quantities on the hydroelastic response is highly nonlinear, where it also deviates for different wavelengths. For example, there is a significant distinction in the response when connections with low rotational stiffness are combined with semi-flexible or rigid modules, as these different combinations result in both the lowest and highest maximum displacements. A similar phenomenon appears for single values of the bending stiffness, while changing the rotational stiffness. Because the response can vary greatly due to the strong dependence on the material properties and wave conditions, it can be difficult to make accurate predictions. It can therefore be concluded that obtaining information by means of these contour plots will give valuable insight in the most optimal combinations with regard to these quantities and the trade-off between minimal displacements and maximum bending moments that occur. This also strengthen the suggestion of previous studies that optimisation of the dimensions and material properties may have great beneficial impact on the hydroelastic reponse, for which this analysis approach can be used in future designs of floating island configurations.

The numerical model copes well for different input parameters, which can be easily adjust. Moreover, the incident waves and water depth can be altered without any difficulty by changing the initial conditions for the velocity potential at the inlet of the domain, or by applying a various depth profile. Accordingly, results can be obtained for more complex (wave) conditions, such as irregular waves, or including seabed topography. The model therefore creates an opportunity to easily analyse a large variety of model setups, in a relatively short amount of time.

7 Recommendations

Based on the results and the discussion, there are aspects that would be valuable to explore more thoroughly in future research. Because the model is highly adaptable, the hydroelastic analysis can be performed for different model setups. First of all, for the design of VLFSs, it is recommended to also obtain the results from a 3D model, where a multi-platform arrangement can be implemented in both horizontal directions. Moreover, including a variable depth profile and implementing irregular wave conditions into the model could provide a more realistic representation of offshore environments.
Furthermore, the analysis is performed taking into account mild wave conditions. However, offshore structures are often designed to survive more extreme conditions, which are beyond the scope of the linear wave theory. In practice, typical non-linear wave conditions (e.g. very steep waves) are still analysed regularly with models based on the linear wave theory. Therefore, the analysis can be performed to investigate the hydroelastic behaviour under more extreme wave conditions. Comparing those results with results obtained by a model that also includes nonlinear effects, could provide valuable insight into the accuracy and scope of the linear model with respect to different (non-linear) input wave conditions.

In the analysis, the bending stiffness is considered to be equal for each individual module. Considering the application of VLFSs in the context of floating urbanisation, it may be allowed for certain areas of the structure to deflect more than others. For example, minimal displacements are desired in densely populated areas with many buildings, while in areas used for e.g. agriculture or solar panels, this requirement may be less strict. It is therefore recommended to also perform the analysis while applying different bending stiffness to the individual modules, based on the specific design criteria of structure. Moreover, for the connection only the rotational stiffness was considered. Yet, including a viscous damper in the connections may have a positive effect on the hydroelastic response and can therefore be considered in future analyses.

To identify optimum design configurations, algorithm operations can be performed to which the results and the developed model can be used. The aim of such optimization processes is to obtain the configuration that operates at a desired response level while preventing structural failure. The design variables considered for the optimal configuration can be constituted into a vector, which is defined for an admissible design space. This design space is bounded by predetermined performance criteria. Consequently, a constrained single objective optimization can be performed for specific wave characteristics; in which e.g. the vertical displacement is the objective that has to be optimized, while the constrain results from the structural capacity, determined by the maximum acceptable bending moments. To this end, genetic algorithms may be applied, which present a stochastic global search method that mimics the metaphor of natural biological evolution as it operates on a population of potential solutions applying the principle of survival of the fittest to produce better and better approximations to a solution [32]. The optimization can be performed with regard to various design variables, such as the material properties, the dimensions of the system or the number of connections.

Finally, further research can be done regarding the numerical application of the FEM model. A future FEM model may be developed using elements that ensure C1-continuity between adjacent elements, to see if this has a positive effect on numerical accuracy or the computation time.

References

[1] C. Shen et al. "Study on the cumulative impact of reclamation activities on ecosystem health in coastal waters". In: *Marine Pollution Bulletin* 103.1-2 (2016), pp. 144–150. DOI: https://doi.org/10.1016/j.marpolbul.2015.12.028.

[2] R. de Graaf. *Adaptive Urban Development - A symbiosis between cities on land and water in the 21st century*. 1st. Rotterdam University, P.O. Box 25035 3001 HA Rotterdam, The Netherlands: Rotterdam University Press of Rotterdam University of Applied Sciences, 2012.

[3] K. Smale. *UN tables floating cities as viable means to tackle global housing crisis*. URL: https://www.newcivilengineer.com/latest/un-tables-floating-cities-as-viable-means-to-tackle-global-housing-crisis-17-04-2019/ (visited on 12/11/2020).

[4] Oceanix ltd. *Oceanix, humanity's next frontier*. URL: https://oceanix.org/ (visited on 09/21/2020).

[5] E. Watanabe et al. *Very Large Floating Structures: Applications, Analysis and Design*. Centre for Offshore Research and Enigneering, National University of Singapore. Feb. 2004.

[6] C.M. Wang and Z.Y. Tay. "Very Large Floating Structures: Applications, Research and Development". In: *Procedia Engineering* 14 (2011), pp. 62–72. DOI: 10.1016/j.proeng.2011.07.007.

[7] G. Wang, Y. Goldfeld, and N. Drimer. "Expanding coastal cities - Proof of feasibility for modular floating structures (MFS)". In: *Journal of Cleaner Production* 222 (2019), pp. 520–538. DOI: https://doi.org/10.1016/j.jclepro.2019.03.007.

[8] *SPACE@SEA*. URL: https://spaceatsea-project.eu/ (visited on 09/21/2020).

[9] W. Otto et al. "On the wave induced motions of a floating mega island". In: *Proceedings of the World Conference on Floating Solutions. Singapore. April 22-23, 2019* edited by C.M. Wang, S.H. Lim and Z.Y. Tay (2019). DOI: https://doi.org/10.1007/978-981-13-8743-2_9.

[10] MARIN. *MARIN tested SPACE@SEA floating mega island*. URL: https://www.marin.nl/news/marin-tested-spacesea-floating-mega-island (visited on 11/11/2020).

[11] O.J. Waals, T.H.J.Bunnik, and W.J. Otto. "Model tests and numerical analysis for a floating island". In: *Proceedings of the ASME 2018 37th International Conference on Ocean, Offshore and Arctic Engineering. Volume 1: Offshore Technolog Madrid, Spain. June 17–22, 2018* V001T01A016. ASME. (2018). DOI: https://doi.org/10.1115/OMAE2018-78589.

[12] R.C. Ertekin et al. "Efficient Methods for Hydroelastic Analysis of Very Large Floating Structures". In: *Journal of Ship Research* 37.1 (1993), pp. 58–79. DOI: 0022-4502/93/3701-0058$00.63/0.

[13] Y. Sun et al. "A study of hydroelastic behavior of hinged VLFS". In: *International Journal of Naval Architecture and Ocean Engineering* 10 (2018), pp. 170–179. DOI: http://dx.doi.org/10.1016/j.ijnaoe.2017.05.002.

[14] J. Ding et al. "Investigation of connector loads of a 3-module VLFS using experimental and numerical methods". In: *Ocean Engineering* 195 (2020), p. 106684. DOI: https://doi.org/10.1016/j.oceaneng.2019.106684.

[15] B.W. Kim et al. "Evaluation of bending moments and shear forces at unit connections of very large floating structures using hydroelastic and rigid body analyses". In: *Ocean Engineering* 34 (2007), pp. 1668–1679. DOI: 10.1016/j.oceaneng.2006.10.018.

[16] S. Fu et al. "Hydroelastic analysis of flexible floating interconnected structures". In: *Ocean Engineering* 37 (2007), pp. 1516–1531. DOI: 10.1016/j.oceaneng.2007.01.003.

[17] R.P. Gao et al. "Hydroelastic response of very large floating structure with a flexible line connection". In: *Ocean Engineering* 38.17-18 (2011), pp. 1957–1966. DOI: 10.1016/j.oceaneng.2011.09.021.

[18] M. Riyansyah, C.M. Wang, and Y.S. Choo. "Connection design for two-floating beam system for minimum hydroelastic response". In: *Marine Structures* 23 (2010), pp. 67–87. DOI: 10.1016/j.marstruc.2010.01.001.

[19] S. Badia and F. Verdugo. "Gridap: An extensible Finite Element toolbox in Julia". In: *Journal of Open Source Software* 5.52 (2020), p. 2520. DOI: 10.21105/joss.02520. URL: https://doi.org/10.21105/joss.02520.

[20] J. Bezanson et al. "Julia: A fresh approach to numerical computing". In: *SIAM review* 59.1 (2017), pp. 65–98. URL: https://doi.org/10.1137/141000671.

[21] A. Tsouvalas. *Course CIE5260 - Structural Response to Earthquakes*. lecture notes. Faculty of Civil Engineering and Geosciences, TU Delft. Sept. 2019.

[22] L. H. Holthuijsen. *Waves in Oceanic and Coastal Waters*. 1st. Shaftesbury Road, Cambridge CB2 8BS, UK: Cambridge University Press, 2010.

[23] Alexey Andrianov. "Hydroelastic Analysis of Very Large Floating Structures". PhD thesis. Delft, NL: Delft University of Technology, Sept. 2005.

[24] M.W. Kim, W. Koo, and S.Y. Hong. "Numerical analysis of various artificial damping schemes in a three-dimensional numerical wave tank". In: *Ocean Engineering* 75 (2014), pp. 165–173. DOI: https://doi.org/10.1016/j.oceaneng.2013.10.012.

[25] J.O. Colomés et al. *A monolithic Finite Element formulation for the hydroelastic analysis of Very Large Floating Structures*. Draft. 2021.

[26] Badia et al. *Gridap Tutorials - Tutorial 6: Poisson equation (with DG)*. URL: https://gridap.github.io/Tutorials/stable/pages/t006_dg_discretization/ (visited on 08/03/2021).

[27] I. Akkerman, J.H.A. Meijer, and M.F.P. ten Eikelder. "Isogeometric analysis of linear free-surface potential flow". In: *Ocean Engineering* 201 (2020), pp. 107–114. DOI: https://doi.org/10.1016/j.oceaneng.2020.107114.

[28] T.I. Khabakhpasheva and A.A. Korobkin. "Hydroelastic behaviour of compound floating plate in waves". In: *Journal of Engineering Mathematics* 44 (2002), pp. 21–40.

[29] K. Sadeghi, G.J. Dzayi, and Z. Alothman. "An overview of generation, theories, formulas and application of sea waves". In: *Academic Research International* 8.4 (2017), pp. 57–67.

[30] S. van Hoof. "Hydroelastic wave deformation of Very Flexible Floating Structures". MA thesis. Delft, NL: Delft University of Technology, Aug. 2021.

[31] C. D. Wang and M. H. Meylan. "The linear wave response of a floating thin plate on water of variable depth". In: *Applied Ocean Research* 24 (2002), pp. 163–174. DOI: https://doi.org/10.1016/S0141-1187(02)00025-1.

[32] C. Michailides, E. Loukogeorgaki, and D. C. Angelides. "Response analysis and optimum configuration of a modular floating structure with flexible connectors". In: *Applied Ocean Research* 43 (2013), pp. 112–130. DOI: http://dx.doi.org/10.1016/j.apor.2013.07.007.

[33] G.N. Wells. *The Finite Element Method: An Introduction*. lecture notes - version 0.3. University of Cambridge and Delft University of Technology. Feb. 2020.

[34] O.C. Zienkiewicz, R.L. Taylor, and J.Z. Zhu. *The Finite Element Method: Its Basis and Fundamentals*. 6th edition. Linacre House, Jordan Hill, Oxford OX2 8DP: Elsevier Butterworth-Heinemann, 2005.

A

Mathematical Formulation of a Single Beam FSI Model

A simple way to represent a continuous floating structure includes an one-dimensional beam model, based on the Euler-Bernoulli theory, floating in a two-dimensional fluid domain. The mathematical theory that corresponds to this single floating beam will form the basis of the continuous model that represent the multi-module VLFS considered in this thesis.
First, the problem is defined based on several assumptions, related to both the structural and fluid domain. These considerations form the frame of reference for which the system is solved. Subsequently, the mathematical formulation of the Euler-Bernoulli beam-fluid model is elaborated. This results in a set of partial differential equations (PDEs), which involves the governing equations of the system including the related boundary, and interface conditions. Finally, the Fourier transform pair is introduced to provide a solution regarding the time dependency of the stated problem.

A.1 Problem Definition

As shown in figure A.1, the continuous FSI model for a single floating structure is represented by the Euler-Bernoulli beam model, floating in the fluid domain, Ω. The structure is modelled in a Cartesian coordinate system. To define the problem based on the Euler-Bernoulli beam theory, the properties of the system and the applied assumptions must first be determined.
Regarding the structural element of the system, the Euler-Bernoulli beam is schematically shown as a 1D member, with only small displacements/deflections performed in the vertical direction. Hence, the system is supposed to behave linearly [21]. Since large displacements are generally not desirable in the design of floating cities, the initial assumption that only small displacements may occur is therefore considered plausible. Furthermore, the beam is assumed to be uniform and homogeneous, which means that the dimensions and material properties are considered to be constant over the cross-section and along the length of the structure. Accordingly, EI represents the bending stiffness of the beam, ρ_b, the mass density, h_b the height, and L the total length of the beam.

The fluid is defined as an ideal fluid and is therefore assumed to be incompressible, with a constant density, ρ_w, and to have no viscosity. Since the forces involved are too small to compress the water and the distances over which variations in density and viscosity are considered, are of a much larger scale, these assumptions seem reasonable [22]. Moreover, the fluid is assumed to have irrotational flow. Because vorticity of the fluid in this case is generated by turbulence at bottom, this local effect will not disturb the main water body significantly [22].
As shown in figure A.1, the fluid domain is 2D, with a constant depth, d. The vertical boundaries of the fluid domain are defined as $\Gamma_{+/-\infty}$, where the other boundaries are described by the free water surface, Γ_{fs}, the bottom surface, Γ_b and the interface between the bottom of the beam and the fluid, Γ_{str}.

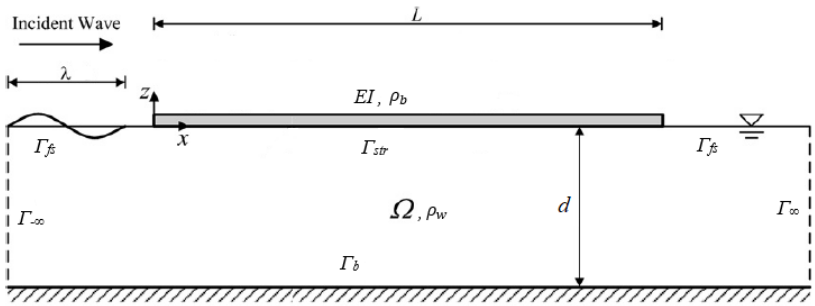

Figure A.1: FSI model - Euler-Bernoulli beam

In this model, the beam is considered to be subject to small, single frequency, head waves, with wave length λ. Because only small wave amplitudes (i.e small compared to the water depth and the wave length) are taken into account in this model, application of the Airy wave theory (also known as the linear wave theory) is valid, provided that the beam is always in contact with the fluid [18]. According to the linear wave theory, the wave frequency ω and the incident wave length λ are related through the following dispersion relation [22]:

$$gk\tanh(kd) = \omega^2 \tag{A.1}$$

Where, $k = 2\pi/\lambda$ is defined as the wave number

A.2 Governing Equations and Conditions

Due to the incoming waves, changes occur regarding the pressure and the elevation at the water surface, which causes vertical displacements of the floating structure. The motion of the water as well as the displacement of the structure are dependent on space and time where the respective behaviour is described by the so-called equation of motion. To solve these equations of motion, boundary conditions are set-up with respect to each domain. Hence, to mathematically describe the interaction of the coupled system, a system of partial differential equations (PDEs) is derived, where this set of equations includes the following components:

- equation of motion (EoM) of the fluid
- equation of motion (EoM) of the beam
- boundary conditions (BCs) for the fluid domain
- interface condition (IC) for fluid-structure interface
- boundary conditions (BCs) for the structural domain

Equation of motion of the fluid

Based on the aforementioned assumptions with respect to the fluid characteristics, the fluid can be described by the continuity equation, known as the Laplace equation. The behaviour of the fluid is expressed in terms of the complex velocity potential $\phi(x,z,t)$, which is a scalar function that represents the particle velocities in the water [22]:

$$\frac{\partial^2\phi(x,z,t)}{\partial x^2} + \frac{\partial^2\phi(x,z,t)}{\partial z^2} = 0 \quad \rightarrow \quad \nabla^2\phi = 0 \qquad \text{in } \Omega \tag{A.2}$$

Similarly, the equation of motion can be expressed in terms of the velocity potential, where the expression for the fluid pressure is derived from the momentum balance (based on the linear wave theory) and the linearized Bernoulli equation [22]:

$$\frac{\partial \phi(x,z,t)}{\partial t} + \frac{p(x,z,t)}{\rho_w} + gz = 0 \quad \rightarrow \quad p(x,z,t) = -\rho_w \frac{\partial \phi(x,z,t)}{\partial t} - \rho_w g z \tag{A.3}$$

Equation of motion of the beam

According to the Euler-Bernoulli beam theory, the equation of motion for the beam is described as follows [21]:

$$\rho_b h_b \frac{\partial^2 w(x,t)}{\partial t^2} + EI \frac{\partial^4 w(x,t)}{\partial x^4} = p(x,z,t)\big|_{\Gamma_{str}} \qquad \text{on} \quad \Gamma_{str} \tag{A.4}$$

Where $w(x,t)$ is the motion/deflection of the beam in vertical direction and $p(x,z,t)$ is the pressure of the water at the surface, which acts on the bottom of the beam (i.e. the interface of the structure and the fluid). For the floating beam system as presented here, the effects of structural damping in the system can be neglected [18].

To solve PDEs, conditions have to be determined, where the initial conditions relate to the time dependence and the boundary, and interface conditions to the spatial dependence of the problem. The required number of BCs/ICs is depending to the order of the differential equation. Here, the order of the EoM equals four, for both the beam and the fluid. So the coupled system needs two times four conditions with respect to the spatial variables. Regarding the time dependency, the system can be solved in the frequency domain due to its linear behaviour. This is further explained in section A.3.

For convenience, the space and time dependence has been omitted from the arguments below

Boundary conditions fluid domain

As shown in figure A.1, the fluid domain is bounded by the seabed, Γ_b, the water surface, which is divided into Γ_{fs} and Γ_{str}, and the vertical boundaries, described as $\Gamma_{-\infty}$ and $\Gamma_{+\infty}$. For each boundary, conditions regarding the fluid motion and/or the pressure are defined:

Seabed
At the seabed no water is allowed to flow through the bottom, hence, the vertical velocity of the water at $z = d$ should be equal to zero. Therefore, the spatial derivative of the potential ϕ, normal to the seabed is equal to zero:

$$\frac{\partial \phi}{\partial z} = 0 \qquad \text{on} \quad \Gamma_b \tag{A.5}$$

Vertical boundaries
In the model, the waves are determined to propagate from x = -∞ to x= +∞. When an incident wave interacts with the floating structure, it will partially reflect at the structure boundary and be partially transmitted. With regard to these reflected and transmitted waves, it is assumed that they will not further interfere with the structure. They must therefore fully propagate away from the system and it is not allowed for these waves to reflect at the vertical boundaries of the fluid domain. This is satisfied by applying the Sommerfeld radiation conditions for a 2D fluid domain at $\Gamma_{-\infty}$ and $\Gamma_{+\infty}$ [17]:

$$\frac{\partial \phi}{\partial x} = ik\phi \qquad \text{on} \quad \Gamma_{+\infty} \tag{A.6}$$

$$\frac{\partial \phi}{\partial x} = -ik\phi \qquad \text{on} \quad \Gamma_{-\infty} \tag{A.7}$$

Free surface
At the surface, the water should satisfy both a kinematic and a dynamic boundary condition. To this end, a function for the surface elevation of the water is introduced, where η is the elevation in water surface measured relative to the mean water level caused by free waves[1] [22].
With regard to the kinematic boundary condition at the free surface, Γ_{fs}, it should hold that water particles can not "leave" the surface. Hence, the water particle velocity in normal direction to the surface should be equal to the velocity of the surface in the same direction, $u_z = \partial\eta/\partial t$ [22]. Regarding the dynamic condition, the water pressure at the surface (see eq. A.3) should be equal to the atmospheric pressure, i.e. equal to zero.

These two aspects are combined to obtain the linearized surface condition, where the water particle velocity, u_z, can be expressed as the spatial derivative of the potential ϕ:

$$\text{kinematic:} \quad \frac{\partial\phi}{\partial z} = \frac{\partial\eta}{\partial t} \qquad \text{on} \quad \Gamma_{fs} \tag{A.8}$$

$$\text{dynamic:} \quad \frac{\partial\phi}{\partial t} + g\eta = 0 \qquad \text{on} \quad \Gamma_{fs} \tag{A.9}$$

Taking the derivative with respect to time for eq. A.9 and substituting eq. A.8 into eq. A.9 will give:

$$\frac{\partial^2\phi}{\partial t^2} + g\frac{\partial\phi}{\partial z} = 0 \qquad \text{on} \quad \Gamma_{fs}$$

Fluid-structure interface
As stated in the problem definition, the structure is always in contact with the water surface. Therefore, the kinematic condition at the interface requires that the elevation of the water surface is equal to the displacement of the beam. Furthermore, the dynamic boundary condition implies that the water pressure at the interface acts as an external distributed load on the bottom of the structure. Hence, the water pressure at the fluid-structure interface is equal to the EoM of the beam:

$$\text{kinematic:} \quad \frac{\partial w}{\partial t} = \frac{\partial\eta}{\partial t} \quad \rightarrow \quad \frac{\partial w}{\partial t} = \vec{n}\cdot\nabla\phi \qquad \text{on} \quad \Gamma_{str} \tag{A.10}$$

$$\text{dynamic:} \quad \rho_b h_b \frac{\partial^2 w}{\partial t^2} + EI\frac{\partial^4 w}{\partial x^4} = -\rho_w\frac{\partial\phi}{\partial t} - \rho_w g\eta \qquad \text{on} \quad \Gamma_{str} \tag{A.11}$$

Boundary conditions structural domain

Finally, it is assumed that the VLFS is not connected to any mooring system. Therefore, no transfer of forces is possible at the outer boundaries of the structure, hence, the moments and shear forces at these locations should be equal to zero. Since the bending moment of the structure is determined by the second derivative with respect to x and the shear force by the third derivative with respect to x, the following four BCs must be satisfied:

$$\frac{\partial^2 w}{\partial x^2} = \frac{\partial^3 w}{\partial x^3} = 0 \qquad \text{at} \quad x = 0 \tag{A.12}$$

$$\frac{\partial^2 w}{\partial x^2} = \frac{\partial^3 w}{\partial x^3} = 0 \qquad \text{at} \quad x = L \tag{A.13}$$

A.3 Transformation into the Frequency Domain

The dynamic response and excitation of the system is determined by variables related to space (x, z) and time (t). In the solution, the dependence related to space is defined by the boundary and interface

[1] waves that are only subject to gravity

conditions. As mentioned earlier, initial conditions are required to solve the derivatives with respect to their time dependence. Since the system is linear, the governing equations can be transformed from the time domain to the frequency domain, in which all quantities can be written as a complex quantity whose time dependence is $e^{-i\omega t}$. The complete system can be transformed to the frequency domain, using the following Fourier transform pair [21]:

$$\tilde{G}(\omega) = \int_{-\infty}^{\infty} g(t)\, e^{-i\omega t}\; dt \qquad \text{and} \qquad g(t) = \frac{1}{2\pi} \int_{-\infty}^{\infty} \tilde{G}(\omega)\, e^{i\omega t}\; d\omega \tag{A.14}$$

By applying the Fourier transform integration, the complete problem as stated above can be expressed in terms of their space dependence in the frequency domain, where all quantities are complex-valued and are frequency dependent [21].

B

Application of the Finite Element Method

The Finite Element Method (FEM) is applied to solve the system of equations representing the VLFS model. In this appendix the general steps for the FEM approach are explained, where a schematized overview of the whole process is illustrated in figure B.1.

B.1 Introduction to Finite Element Methods

The Finite Element Method is a numerical method used for solving partial differential equations (PDEs), where the application of this method ultimately leads to (often very large) systems of linear equations (matrices) which can be solved with a computer [33].

PDEs are continuous functions, which means that they have an infinite number of degrees of freedom (DoFs) or 'unknowns'. However, to solve the problem numerically the model must have finite quantities. In FEM models the domain of the continuous problem is therefore divided into a mesh of small finite elements, reducing the number of DoFs from infinite to finite; where the (for example) unknown displacements of the whole system are described by the displacements of these finite elements. As shown in figure B.1, the elements are arranged by means of boundaries/facets and a discrete number of nodal points. According to FEM, it is assumed that the state of displacement within each finite element and on its boundaries can be defined in terms of so-called shape functions, and the nodal displacements [34] (see section B.3). Because the shape functions are predetermined polynomials, the nodal displacements will be the basic unknown parameters of the problem. The expression obtained for the unknown parameters is then substituted into the governing equations of the considered problem, which are formulated in their weak form (see section B.2). Ultimately, the continuous problem can be approached by a discrete analysis; where the unknown displacements are solved by means of the resulting system of linear equations.
Due to the discretization, the solution can only be found approximately. In FEM, the sum of the element contributions is assumed to be equal to the whole system. Therefore, the calculations are performed 'elementwise'. First, the set of shape functions is determined for a single FE, after which the functions for the individual elements are assembled and the total set of equations solved as a whole to find the displacements at the nodes of the separated elements.

B.2 Weak Form

Prior to performing the spatial discretization as described above, the equations formulating the physical problem must be defined in the so-called 'variational' or 'weak' form. In contrast, the analytical formulations derived in chapter 2 are described in their 'strong form'. This means that the equations must be satisfied for any point (i.e. x,z coordinate) in the continuous domain. Yet, this requirement is inconvenient regarding the discrete analysis of the finite elements. An essential step in the FEM process is therefore casting the considered equations in their 'weak form'. Accordingly, an equation is 'weakened'

by allowing the equation in its weak form not to satisfy in every point, but only in a global, average sense (through integration). To do this, the strong form is multiplied by a weight function (also referred as test function) and integrated over the domain. Subsequently, integration by parts is performed to the resulting expression, which reduces the order of the derivatives appearing in the equation and leads to a form which is convenient for later numerical solution [33]. To show the required steps to obtain the weak form, the derivation for the Laplace equation is elaborated here below.

B.2.1 Deriving the weak form for the Laplace equation

Using the same notation as introduced in chapter 2 and Appendix A, the Laplace equation for a 2D fluid domain is given by:

$$\nabla^2 \phi = 0 \qquad \text{in} \quad \Omega \tag{B.1}$$

Where a general expression for the associated boundary condition(s) is given by:

$$\vec{n} \cdot \nabla \phi = f \qquad \text{on} \quad \Gamma \tag{B.2}$$

To derive the weak form, the equation is multiplied by a weight function $v \in \mathcal{V}$, where $v \in \mathcal{V}$ means that v comes from the appropriately defined solution space $\mathcal{V}$ [33]. Subsequently integrating the expression over the domain will give:

$$\int_\Omega v \cdot \nabla^2 \phi \, d\Omega \; = \; 0 \qquad \forall \; v \in \mathcal{V} \tag{B.3}$$

Next, the equation is integrated by parts. This is a method to find the integral of products, where one function is considered as the derivative of the other which subsequently reduces the order of the derivative. As a result, the integral can be rewritten into two separate terms; including an integral over the domain and one over the boundary, in which the derivative of ϕ is an order lower:

$$\int_\Omega v \cdot \nabla^2 \phi \, d\Omega \; = \; - \int_\Omega \nabla v \cdot \nabla \phi \, d\Omega \; + \; \int_\Gamma v \cdot (\vec{n} \cdot \nabla \phi) \, d\Gamma \; = \; 0 \tag{B.4}$$

This shows that integrating by parts leads to a form which is convenient, as it results in an expression which includes a formulation for the boundary condition. Hence, substituting the expression B.2 into equation B.4 will give:

$$- \int_\Omega \nabla v \cdot \nabla \phi \, d\Omega \; + \; \int_\Gamma v \cdot f \, d\Gamma \; = \; 0 \tag{B.5}$$

Ultimately, the weak form is derived to find the solution for $\phi \in \mathcal{V}$ such that $B(\phi, v) = l(v) \; \forall \; v \in \mathcal{V}$. The formulations can therefore be expressed in the bilinear function $B(\phi, v)$ and the linear function $l(v)$, where:

$$B(\phi, v) = \int_\Omega \nabla v \cdot \nabla \phi \, d\Omega \tag{B.6}$$

and

$$l(v) = \int_\Gamma v \cdot f \, d\Gamma \tag{B.7}$$

B.3 Spatial Discretization & Shape Functions

Once the governing equations are defined in their weak form and a mesh is generated to divide the domain into finite elements, an approximated solution for the displacements within each element and on its boundaries is formulated. To this end, the Galerkin Method is applied. As shown in figure B.1, this method assumes that the approximated solution $\hat{u}_i(x, y)$ can be described in terms of the sum of predefined shape functions, N_i, and the displacements at the nodal points, $\hat{u}_i$, of the respective element:

$$\hat{u}(x, y) = \sum_{i=1}^{n} N_i \hat{u}_i$$

Subsequently, this assumed expression for the displacement is substituted into the weak form, which ultimately results in a linear system of equations that can be solved.

Important here is that the shape functions are known. This allows to define an aprior interpolation of the solution between the nodal points, where the shape functions are then used to define the influence of point i over the element domain. There are many different shapes functions that can be applied in defining the finite elements. The simplest shape functions of an element involve linear interpolation between two nodes. Higher-order polynomial interpolation can be achieved by using elements that have more nodes. Also the shape of each element can differ from triangular or quadrilateral considering 2D-problems, to tetrahedral and brick shapes elements when looking at 3D meshes. Selecting the appropriate elements is therefore of paramount importance and the degree of accuracy for the approximate solution is highly dependent on these choices [34].

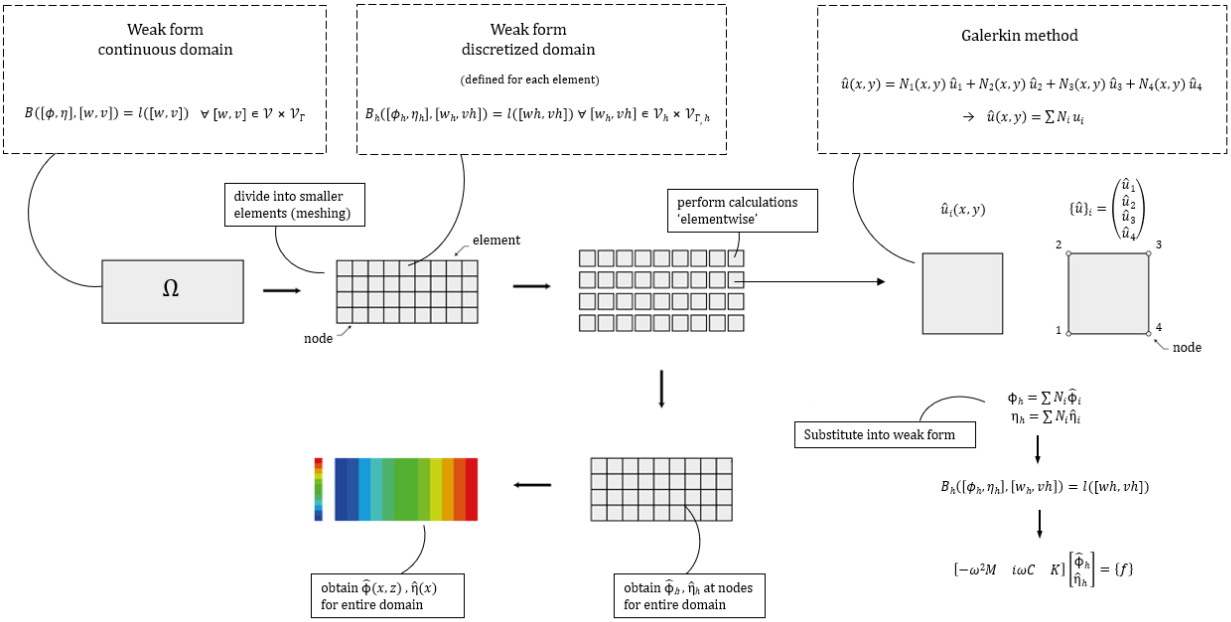

Figure B.1: FEM process

B.4 Isoparametric Elements

According to the Galerkin Method, the approximated solution can be described by the sum of assumed known shape functions and the displacements at the nodal points. Hence, in theory, the respective shape

functions for each individual element needs to be determined. Nevertheless, a FEM model usually consists of a large number of elements for which different shapes and shape functions may be applied; making it rather time consuming to derive the different shape functions for each individual element.

In practice, isoparametric elements are therefore used in finite element software. Detailed derivations to show the implementation of isoparametric elements are not discussed here, but essentially the shape functions are derived for a simple element configuration (usually elements with a unit length side and with sides aligned with the coordinate system and with a convenient origin) [33]. Using isoparametric mapping as shown in figure B.2, this element operates as a 'reference element' and it therefore requires programming only one function to evaluate the shape functions of all the elements within the domain, regardless of the element's exact shape.

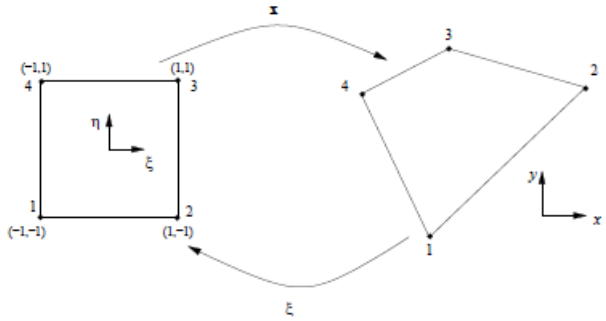

Figure B.2: Isoparametric mapping [33]

C
Numerical Results of Hydroelastic Analysis

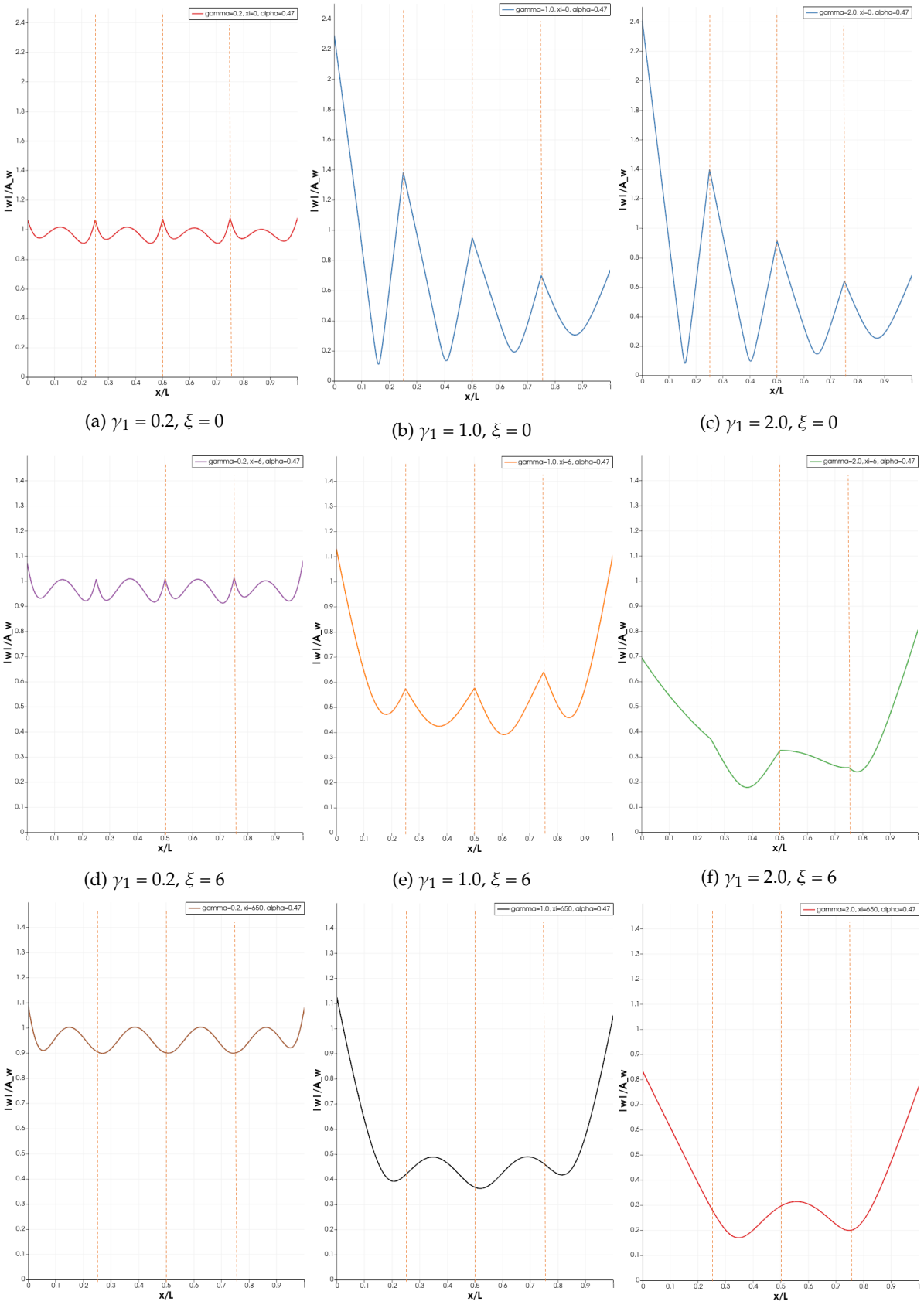

(a) $\gamma_1 = 0.2$, $\xi = 0$ (b) $\gamma_1 = 1.0$, $\xi = 0$ (c) $\gamma_1 = 2.0$, $\xi = 0$

(d) $\gamma_1 = 0.2$, $\xi = 6$ (e) $\gamma_1 = 1.0$, $\xi = 6$ (f) $\gamma_1 = 2.0$, $\xi = 6$

(g) $\gamma_1 = 0.2$, $\xi = 650$ (h) $\gamma_1 = 1.0$, $\xi = 650$ (i) $\gamma_1 = 2.0$, $\xi = 650$

Figure C.1: Normalized displacements for $\alpha = 0.47$

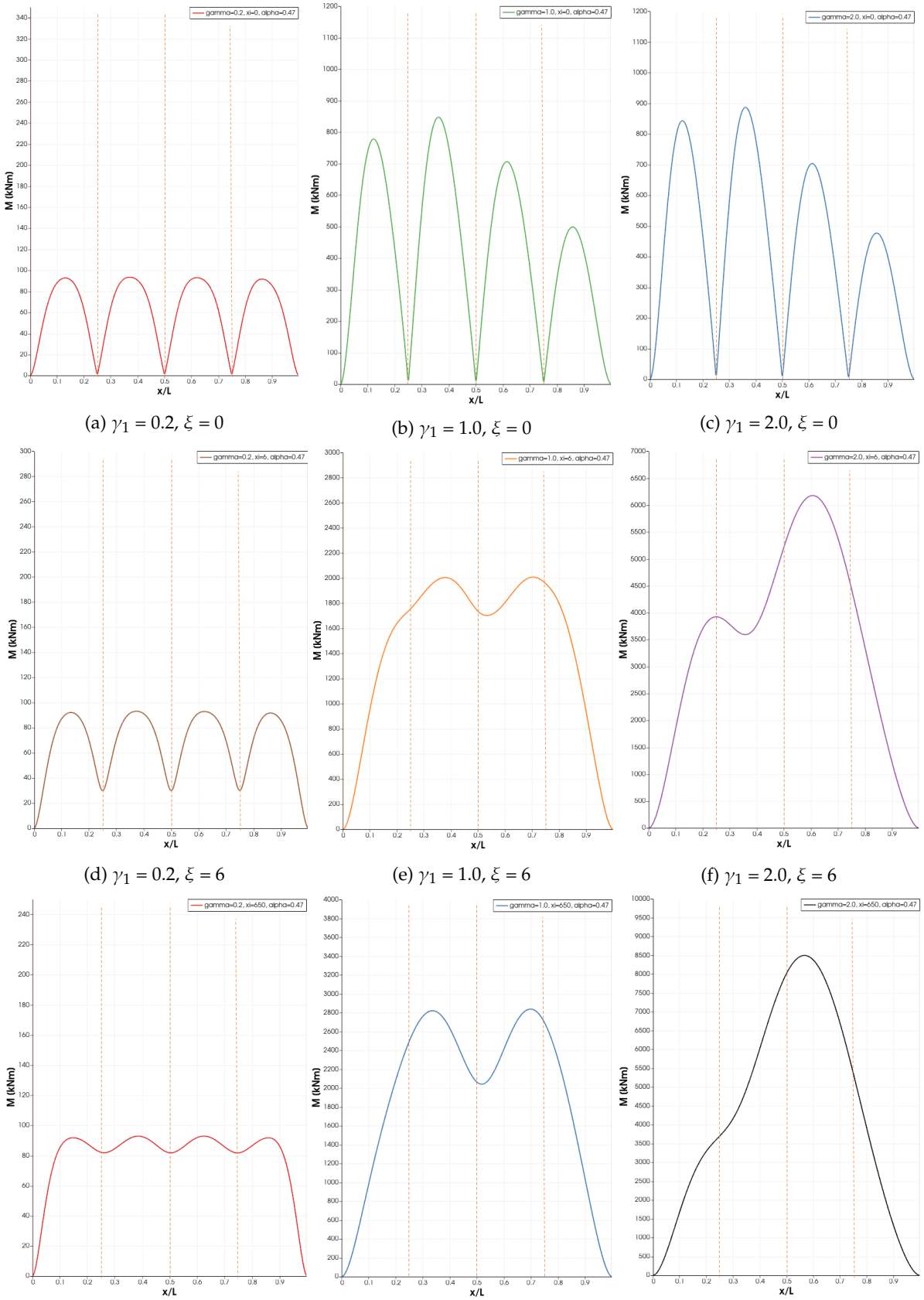

(a) $\gamma_1 = 0.2$, $\xi = 0$ (b) $\gamma_1 = 1.0$, $\xi = 0$ (c) $\gamma_1 = 2.0$, $\xi = 0$

(d) $\gamma_1 = 0.2$, $\xi = 6$ (e) $\gamma_1 = 1.0$, $\xi = 6$ (f) $\gamma_1 = 2.0$, $\xi = 6$

(g) $\gamma_1 = 0.2$, $\xi = 650$ (h) $\gamma_1 = 1.0$, $\xi = 650$ (i) $\gamma_1 = 2.0$, $\xi = 650$

Figure C.2: Moment distribution for $\alpha = 0.47$

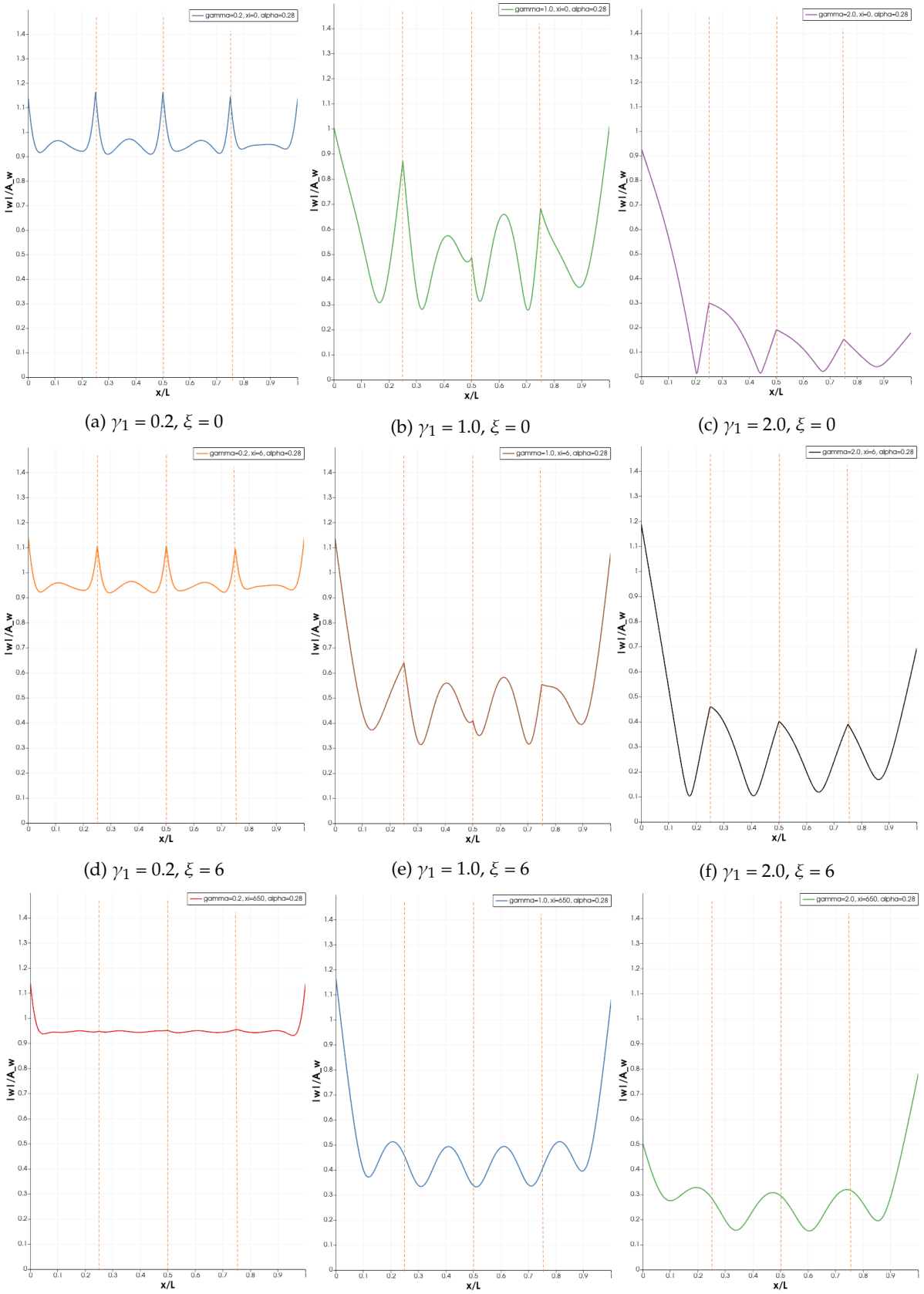

(a) $\gamma_1 = 0.2$, $\xi = 0$ (b) $\gamma_1 = 1.0$, $\xi = 0$ (c) $\gamma_1 = 2.0$, $\xi = 0$

(d) $\gamma_1 = 0.2$, $\xi = 6$ (e) $\gamma_1 = 1.0$, $\xi = 6$ (f) $\gamma_1 = 2.0$, $\xi = 6$

(g) $\gamma_1 = 0.2$, $\xi = 650$ (h) $\gamma_1 = 1.0$, $\xi = 650$ (i) $\gamma_1 = 2.0$, $\xi = 650$

Figure C.3: Normalized displacements for $\alpha = 0.28$

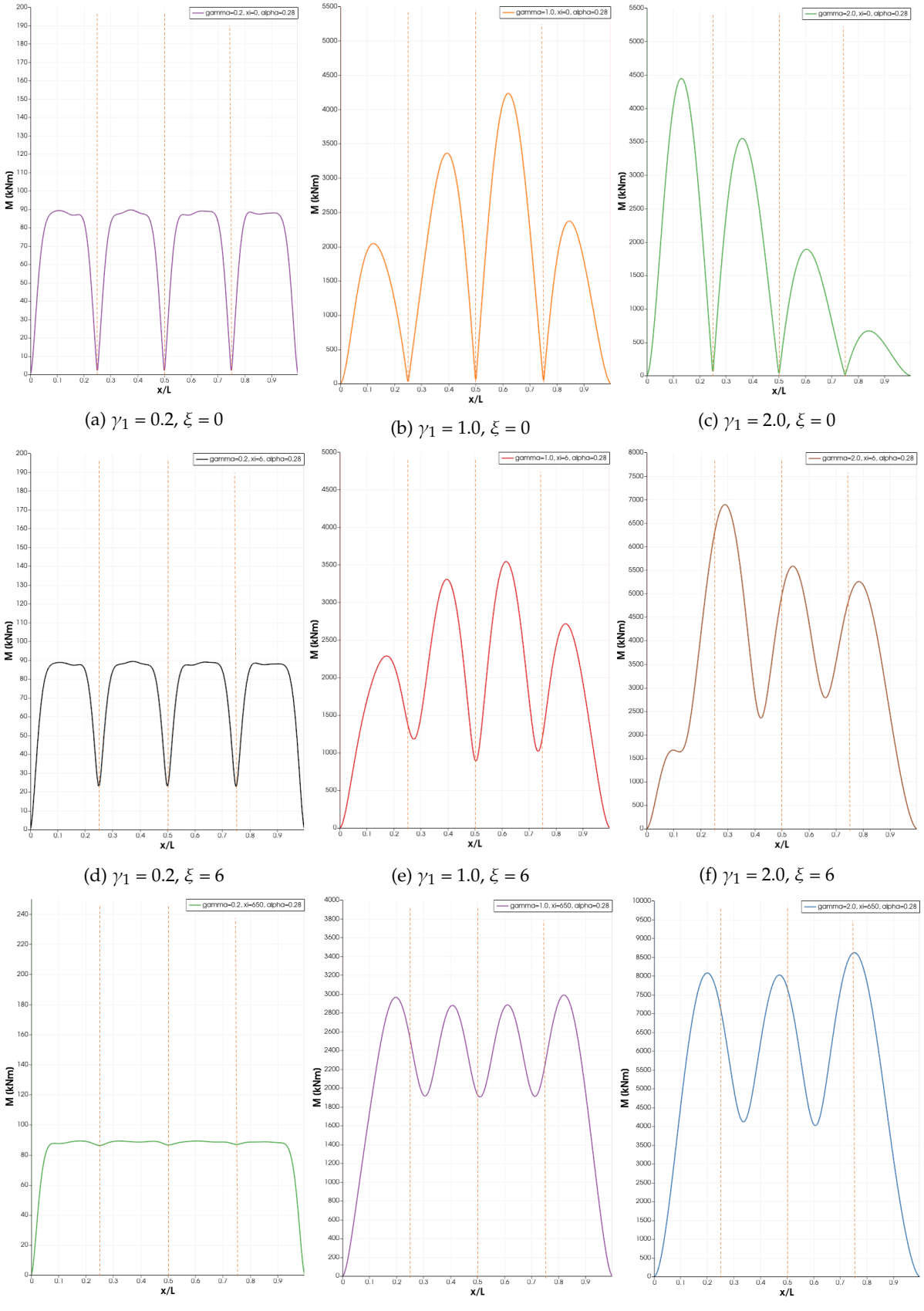

(a) $\gamma_1 = 0.2$, $\xi = 0$ (b) $\gamma_1 = 1.0$, $\xi = 0$ (c) $\gamma_1 = 2.0$, $\xi = 0$

(d) $\gamma_1 = 0.2$, $\xi = 6$ (e) $\gamma_1 = 1.0$, $\xi = 6$ (f) $\gamma_1 = 2.0$, $\xi = 6$

(g) $\gamma_1 = 0.2$, $\xi = 650$ (h) $\gamma_1 = 1.0$, $\xi = 650$ (i) $\gamma_1 = 2.0$, $\xi = 650$

Figure C.4: Moment distribution for $\alpha = 0.28$

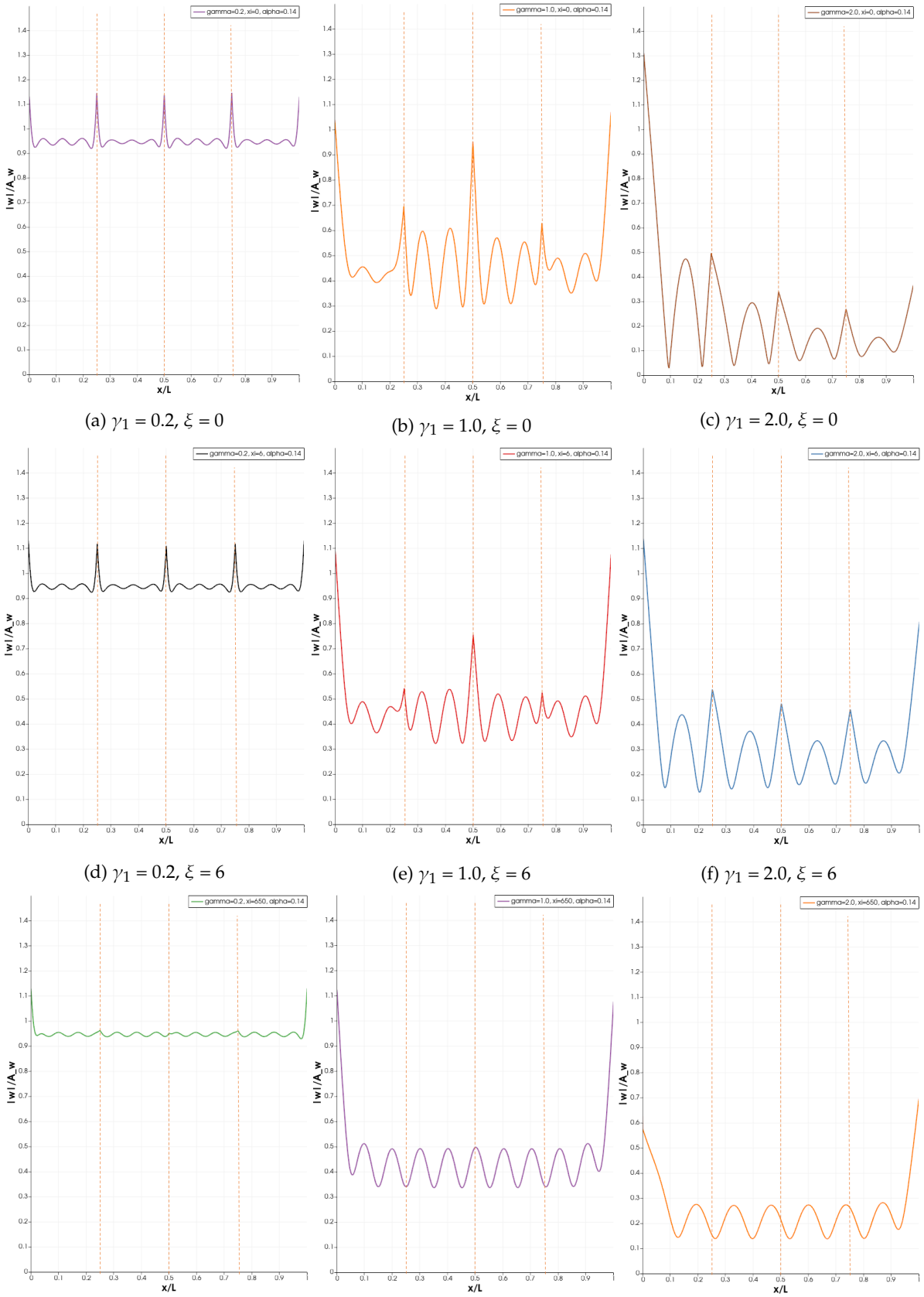

(a) $\gamma_1 = 0.2$, $\xi = 0$ (b) $\gamma_1 = 1.0$, $\xi = 0$ (c) $\gamma_1 = 2.0$, $\xi = 0$

(d) $\gamma_1 = 0.2$, $\xi = 6$ (e) $\gamma_1 = 1.0$, $\xi = 6$ (f) $\gamma_1 = 2.0$, $\xi = 6$

(g) $\gamma_1 = 0.2$, $\xi = 650$ (h) $\gamma_1 = 1.0$, $\xi = 650$ (i) $\gamma_1 = 2.0$, $\xi = 650$

Figure C.5: Normalized displacements for $\alpha = 0.14$

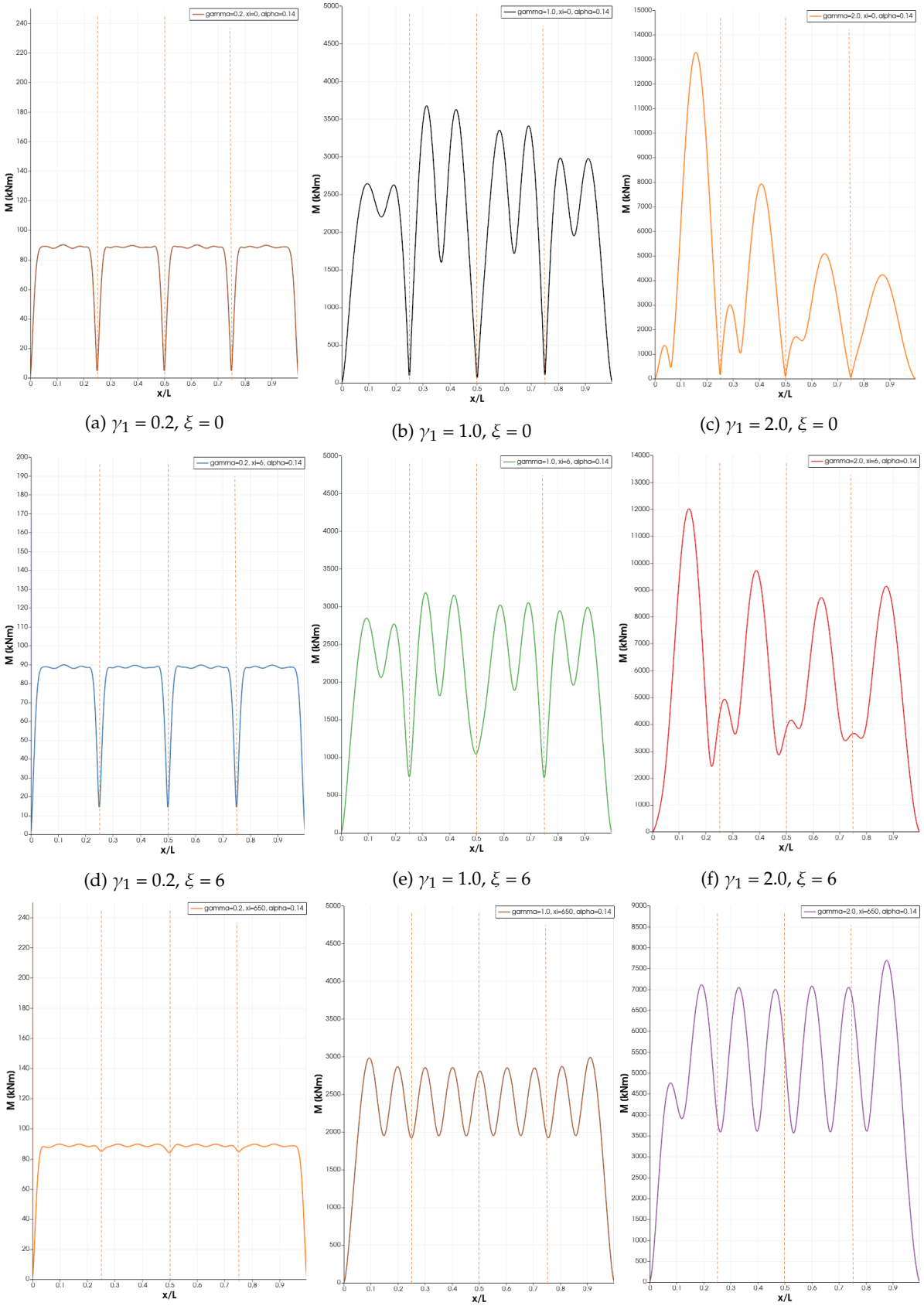

(a) $\gamma_1 = 0.2$, $\xi = 0$ (b) $\gamma_1 = 1.0$, $\xi = 0$ (c) $\gamma_1 = 2.0$, $\xi = 0$

(d) $\gamma_1 = 0.2$, $\xi = 6$ (e) $\gamma_1 = 1.0$, $\xi = 6$ (f) $\gamma_1 = 2.0$, $\xi = 6$

(g) $\gamma_1 = 0.2$, $\xi = 650$ (h) $\gamma_1 = 1.0$, $\xi = 650$ (i) $\gamma_1 = 2.0$, $\xi = 650$

Figure C.6: Moment distribution for $\alpha = 0.14$

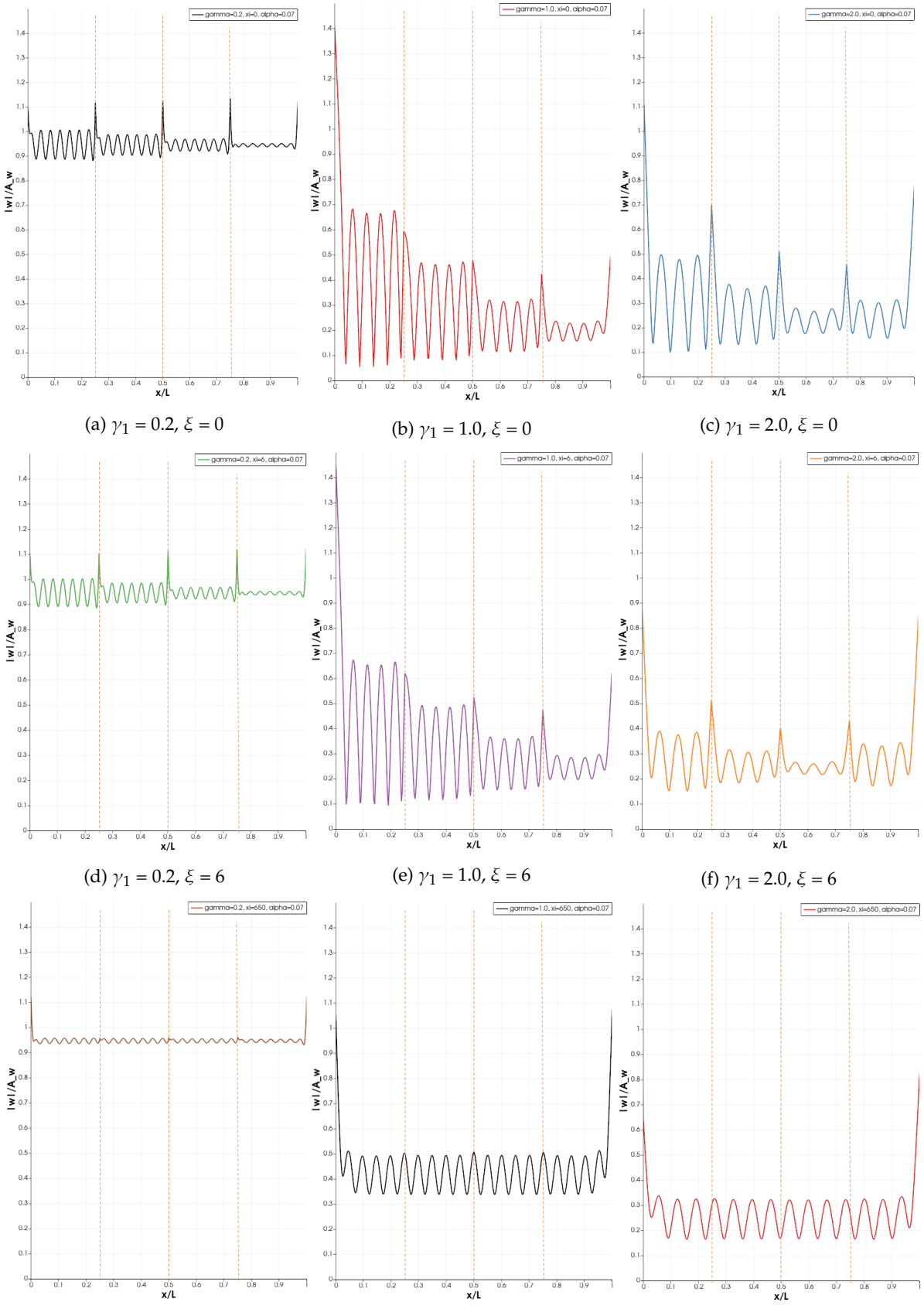

(a) $\gamma_1 = 0.2$, $\xi = 0$ (b) $\gamma_1 = 1.0$, $\xi = 0$ (c) $\gamma_1 = 2.0$, $\xi = 0$

(d) $\gamma_1 = 0.2$, $\xi = 6$ (e) $\gamma_1 = 1.0$, $\xi = 6$ (f) $\gamma_1 = 2.0$, $\xi = 6$

(g) $\gamma_1 = 0.2$, $\xi = 650$ (h) $\gamma_1 = 1.0$, $\xi = 650$ (i) $\gamma_1 = 2.0$, $\xi = 650$

Figure C.7: Normalized displacements for $\alpha = 0.07$

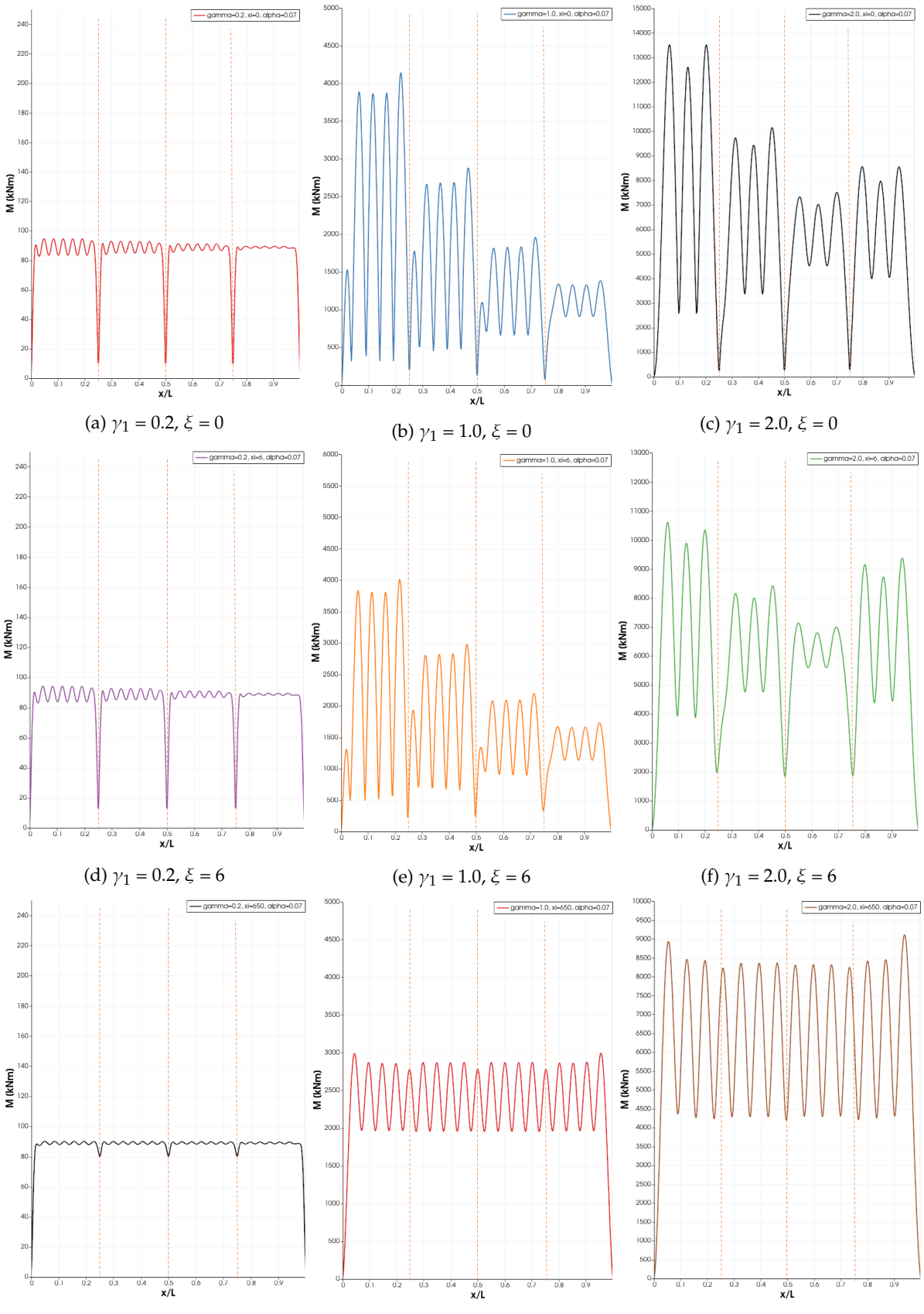

(a) $\gamma_1 = 0.2$, $\xi = 0$ (b) $\gamma_1 = 1.0$, $\xi = 0$ (c) $\gamma_1 = 2.0$, $\xi = 0$

(d) $\gamma_1 = 0.2$, $\xi = 6$ (e) $\gamma_1 = 1.0$, $\xi = 6$ (f) $\gamma_1 = 2.0$, $\xi = 6$

(g) $\gamma_1 = 0.2$, $\xi = 650$ (h) $\gamma_1 = 1.0$, $\xi = 650$ (i) $\gamma_1 = 2.0$, $\xi = 650$

Figure C.8: Moment distribution for $\alpha = 0.07$

D
Tutorial

Very Large Floating Structure (VLFS)

Authors: Dorette Regout and Oriol Colomés Gené

Published: October 2021

This tutorial shows how to solve a Fluid Structure Interaction (FSI) problem using Gridap and provides the instructions to build a 2D model considering a multi-module VLFS, solved in the frequency domain.

Problem statement

As shown in the figure below, the multi-module VLFS is represented by four floating one-dimensional beams, interconnected by rotational springs, where the structure is located on top of a two-dimensional fluid domain. The dynamic response of the structure is described by the Euler-Bernoulli beam theory and it is assumed that the beams will only perform small displacements in vertical direction. As the structure is subject to small, single frequency, incident head waves (with a wavelength λ), the linear (Airy) wave theory is therefore assumed to be valid, provided that the beams are always in contact with the fluid.

The total length of the VLFS is denoted by L, where the beams have a uniform and homogeneous cross-section along the structure. The bending stiffness, the mass density, the height, and the length of each beam element are denoted by EI, ρ_b, h_b, and βL, respectively. The rotational stiffness for each connection is defined by $k_r = \xi EI/L$, where ξ is the rotational stiffness parameter. The 2D fluid domain, denoted as Ω, has a constant depth, d, with a constant density, ρ_w. The boundaries of the domain are defined by the seabed, Γ_b, the free water surface, Γ_{fs}, the

fluid-structure interface, Γ_{str}, and two vertical boundaries, Γ_L and Γ_R, on the left and right side of the domain. The fluid is considered to be inviscid, incompressible, and has irrotational flow. As a result, the fluid is expressed by the velocity potential, which is a scalar function that represents the velocity field of the water in terms of spatial derivatives of the scalar function ϕ.

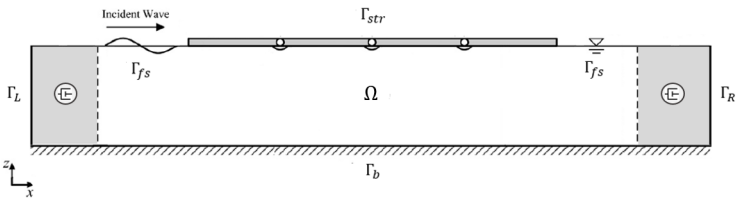

VLFS model

Transformation to the frequency domain

Due to the excitation of the waves, the water pressure and the elevation at the water surface will change, causing vertical displacements of the floating beams. This interaction between the motion of the water and the displacement of the structure is mathematically described by partial differential equations (PDEs) that initially depend on space and time. Accordingly, initial conditions (with respect to time) and boundary/interface conditions (with respect to space) have to be determined to solve the problem. In another tutorial called "Very Flexible Floating Structure", it is demonstrated how to solve the FSI problem for a single floating 1D beam in the time-domain.

However, solving these type of FSI problems in the time domain may be computationally intensive and it is therefore more convenient to solve the problem in the frequency domain. In general, time dependent PDEs can be transformed to the corresponding frequency domain by applying the following Fourier transform pair:

$$\tilde{G}(\omega) = \int_{-\infty}^{\infty} g(t)\, e^{-i\omega t}\, dt \qquad \text{and} \qquad g(t) = \frac{1}{2\pi} \int_{-\infty}^{\infty} \tilde{G}(\omega)\, e^{i\omega t}\, d\omega \tag{1}$$

Due to the linearity of the system, this approach may be applied and each quantity in the time domain is rewritten in its respective term in the frequency domain. Hence, all equations for this model are expressed in terms of their space dependence in the frequency domain, where all quantities are complex-valued and are frequency dependent. Consequently, the solution to the problem will be solved regarding the steady-state solution.

Mathematical formulation

To build the FSI model, first, the mathematical formulation to describe the interaction of the coupled system is discussed. This results a system of PDEs, where this set of equations will include the following components:

- equation of motion (EoM) of the fluid
- equation of motion (EoM) of the structure
- boundary/interface conditions (BCs/ICs) for the fluid domain
- boundary/interface conditions (BCs/ICs) for the structural domain

EoM fluid

Based on the aforementioned fluid characteristics, the divergence of the fluid velocity is considered to be zero. This results in the velocity potential ϕ to satisfy the Laplace equation. Similarly, the fluid pressure can be expressed in terms of the velocity potential, where the equation for the pressure is derived from the momentum balance and the linearized Bernoulli equation (based on the linear wave theory):

$$\begin{cases} \nabla \cdot \vec{u} = 0 \\ \nabla \phi = \vec{u} \end{cases} \Leftrightarrow \nabla \cdot (\nabla \phi) = \Delta \phi = 0 \quad \text{in} \quad \Omega \tag{2}$$

$$
\begin{aligned}
&-i\omega\phi + \frac{p}{\rho_w} + gz = 0 \qquad\qquad \text{in} \quad \Omega \\
\rightarrow \quad & p = -\rho_w g z + i\omega\rho_w\phi
\end{aligned} \tag{3}
$$

EoM VLFS

According to the Euler-Bernoulli beam theory, the equation of motion of the VLFS is described as follows:

$$
-\omega^2 \rho_b h_b w + EI\frac{\partial^4 w}{\partial x^4} = p\,|_{\Gamma_{str}} \qquad \text{on} \quad \Gamma_{str} \tag{4}
$$

Where w is the vertical displacement of the VLFS in z-direction and p is the pressure at the water surface, acting as a distributed load on the bottom of the VLFS, i.e. the interface of the structure and the fluid.

To solve the problem, the following boundary conditions for both the fluid and the VLFS structure are determined:

Sea bed boundary

The impermeability condition holds at the seabed, which means that no water is allowed to flow through the bottom. Therefore, the flow velocity normal to the seabed is equal to zero. As the velocity field of the water can be expressed in terms of spatial derivatives of the scalar function ϕ, this results in:

$$
\vec{n}\cdot\nabla\phi = 0 \qquad \text{on} \quad \Gamma_b \tag{5}
$$

Free surface

At the free surface, the water should satisfy both a kinematic and a dynamic boundary condition. To this end, a function for the surface elevation of the water is introduced; where η is the elevation in water surface, measured relative to the mean water level.

For the kinematic boundary condition holds that the water particles cannot 'leave' the water surface. Therefore, the flow velocity in normal direction to the surface should be equal to the velocity of the surface elevation. Regarding the dynamic condition, the water pressure at the surface should be equal to the atmospheric pressure, i.e. equal to zero:

$$
\begin{aligned}
\text{kinematic:} \qquad & \vec{n}\cdot\nabla\phi = -i\omega\eta \quad \text{on} \quad \Gamma_{fs} \\
\text{dynamic:} \qquad & -i\omega\phi + g\eta = 0 \quad \text{on} \quad \Gamma_{fs}
\end{aligned} \tag{6}
$$

Vertical boundaries - damping zone

In the model, the waves propagate from left to right. When an incident wave interacts with the floating structure, it will partially reflect at the structure boundary and be partially transmitted. It is assumed that these reflected, and transmitted waves will not further interfere with the structure. They must therefore fully propagate away from the system and it is not allowed for these waves to reflect at the vertical boundaries of the fluid domain.

Hence, the boundary condition at the inlet of the domain is determined by the predefined expression for the incident wave, ϕ_{inc}, where the BC at the outlet is set to zero:

$$
\begin{aligned}
&\vec{n}\cdot\nabla\phi = 0 \qquad\qquad \text{on} \quad \Gamma_R \\
&\vec{n}\cdot\nabla\phi = \vec{n}\cdot\nabla\phi_{\text{inc}} \quad \text{on} \quad \Gamma_L
\end{aligned} \tag{7}
$$

To assure energy dissipation such that these conditions at the vertical boundaries are satisfied, two damping zones (at both the inlet and the outlet) are constructed in the model. To this end, a method by Kim Woo Min is used, who introduced two additional terms for the kinematic boundary condition which dissipate the wave energy. This results in the following alteration for the kinematic condition at the free surface:

$$-i\omega\eta - \vec{n}\cdot\nabla\phi + \mu_1(\eta - \eta_{\text{inc}}) + \frac{\mu_2}{g}(\phi - \phi_{\text{inc}}) = 0 \qquad \text{on} \quad \Gamma_{fs} \tag{8}$$

Where η_{inc} and ϕ_{inc} (defined by the incident wave expression) are the reference values when the computational domain is not disturbed by any structure during the wave propagation. μ_1 and μ_2 are the damping coefficients, which are dependent on each other to ensure that no dispersion occurs:

$$\mu_1(x) = \mu_0 \left[1 - \sin\left\{\frac{\pi}{2}\left(\frac{x}{L_{d,in}}\right)\right\}\right] + \mu_0 \left[1 - \cos\left\{\frac{\pi}{2}\left(\frac{x - x_d}{L_{d,out}}\right)\right\}\right] \tag{9}$$

$$\mu_2(x) = -\frac{\mu_1(x)^2}{4} \tag{10}$$

Where $L_{d,in}$ and $L_{d,out}$ are the total lengths of the respective damping zone. x_d is starting point of the damping zone at the oulet. The input value, μ_0, is selected on a trial and error basis, depending on the wave characteristics.

Fluid-structure interface

Also at the fluid-structure interface both a kinematic and a dynamic condition is defined. For the kinematic condition, the elevation of the water surface is equal to the displacement of VLFS. For the dynamic boundary condition, the water pressure at the surface acts as a distributed load at the bottom of the structure. Hence, the expression for the water pressure is substituted in the EoM of the VLFS.

Since the equation of motion for the structure is substituted as a complex boundary condition of the fluid domain, it is more convenience to rewrite the vertical displacement of the structure - previously indicated with w - in terms of the surface elevation η. Therefore, the boundary conditions at the fluid-structure interface yield:

$$\begin{aligned} \text{kinematic:} \qquad & -i\omega\eta = \vec{n}\cdot\nabla\phi && \text{on} \quad \Gamma_{str} \\ \text{dynamic:} \qquad & -\omega^2\alpha_{b1}\eta + \alpha_{b2}\frac{\partial^4\eta}{\partial x^4} - i\omega\phi + g\eta = 0 && \text{on} \quad \Gamma_{str} \end{aligned} \tag{11}$$

Where $\alpha_{b1} = \frac{\rho_b h_b}{\rho_w}$, and $\alpha_{b2} = \frac{EI}{\rho_w}$.

Structural domain

The moments and shear forces at the free ends of the VLFS should be equal to zero. Consequently, for the first and the last beam element, the following four dynamic BCs must be satisfied:

$$\begin{aligned} \frac{\partial^2\eta}{\partial x^2} = \frac{\partial^3\eta}{\partial x^3} = 0 \qquad & \text{at} \quad x = 0 \quad \text{on} \quad \Gamma_{str} \\ \frac{\partial^2\eta}{\partial x^2} = \frac{\partial^3\eta}{\partial x^3} = 0 \qquad & \text{at} \quad x = L \quad \text{on} \quad \Gamma_{str} \end{aligned} \tag{12}$$

Finally, some conditions at the connection points of the VLFS are determined. At each connection, the kinematic conditions (i.e. continuity in displacement and rotation), and the dynamic boundary conditions (i.e. force equilibrium) are satisfied. At each connection location x_j the following 4 ICs should hold:

$$\begin{aligned} \eta\big|_{x_j^-} &= \eta\big|_{x_j^+} \\ \frac{\partial\eta}{\partial x}\big|_{x_j^-} &= \frac{\partial\eta}{\partial x}\big|_{x_j^+} \\ EI\frac{\partial^2\eta}{\partial x^2}\big|_{x_j^-} = EI\frac{\partial^2\eta}{\partial x^2}\big|_{x_j^+} &= k_r\left(\frac{\partial\eta}{\partial x}\big|_{x_j^-} - \frac{\partial\eta}{\partial x}\big|_{x_j^+}\right) \\ EI\frac{\partial^3\eta}{\partial x^3}\big|_{x_j^-} &= EI\frac{\partial^3\eta}{\partial x^3}\big|_{x_j^+} \end{aligned} \tag{13}$$

To conclude, the motion of the fluid is described by the Laplace equation within the fluid domain, where the equation of motion for the structure is substituted as a complex boundary condition for the fluid-structure interface. Together with the other boundary conditions as defined above, this results in a well-posed problem, which can now be solved.

Expressions of the incident wave

According to the linear wave theory, the potential of the incident wave ϕ_{inc} for perpendicular waves and considering water of finite depth, is written in the following form:

$$\phi_{\text{inc}} = \frac{gA_w}{i\omega} \frac{\cosh k(z+d)}{\cosh kd} \mathrm{e}^{ikx} \tag{14}$$

Where A_w is the wave amplitude of the incident wave. The incident wave number k, the wave frequency ω, and the incident wavelength λ, are related through the dispersion relation:

$$gk \tanh(kd) = \omega^2 \tag{15}$$

Where, $k = 2\pi/\lambda$ is defined as the wave number

Consequently, the expressions for the surface elevation of the incident wave η_{inc} and the velocity of the fluid in x-direction over the boundary Γ_L are formulated as follows:

$$\begin{aligned} \frac{\partial \phi_{\text{inc}}}{\partial z} = -i\omega\eta_{\text{inc}} \quad &\rightarrow \quad \eta_{\text{inc}} = \frac{gA_w k}{\omega^2} \frac{\sinh k(z+d)}{\cosh kd} \mathrm{e}^{ikx} \\ \vec{n} \cdot \nabla \phi_{\text{inc}}\big|_{\Gamma_L} \quad &\rightarrow \quad \frac{\partial \phi_{\text{inc}}}{\partial x} = \frac{gA_w k}{\omega} \frac{\cosh k(z+d)}{\cosh kd} \mathrm{e}^{ikx} \end{aligned} \tag{16}$$

Numerical model

Now that the mathematical formulation behind the model has been described, the system of equations can be rewritten into the weak formulation and inserted into the numerical model. However, in order to do so, the input parameters regarding the incident wave and material properties are defined first, afterwhich the numerical model is set up.

Input parameters

Material Properties

For this tutorial it is assumed that the VLFS has a solid rectangular cross-section with a height of 2m. The type of connection can be determined by varying the rotational stiffness parameter, where $\xi = 0$ corresponds to a hinged connection, and $\xi = 650$ to a rigid connection. In this tutorial a value of $\xi = 0$ is applied.

Finally, the length of the separated modules can be altered by changing the locations of the connections with the connection location parameter β. Here, it is assumed that the four modules all have the same length, i.e. $\beta = 0.25$.

```
ρ_b = 250               # mass density VLFS [kg m^-3]
h_b = 2                 # height VLFS [m]
L = 1000                # total length VLFS [m]
I = 1/12*h_b^3          # second moment of inertia per unit meter width (I/b)
E = 12e9                # Youngs modulus [N/m^2]
EI_b = E*I              # bending stiffness VLFS per unit meter width [Nm/m]
ξ = 0                   # rotational stiffness parameter
k_r = ξ*EI_b/L          # rotational stiffness connection [Nm]
β = 0.25                # connection location parameter

α1_b = ρ_b*h_b/ρ_w
α2_b = EI_b/ρ_w
```

Fluid domain and incident wave

The fluid characteristics, the dimensions of the fluid domain, and the conditions for the incident wave are described here below; where the input parameters correspond to mild wave conditions.

```
g = 9.81                    # gravitational constant
ρ_w = 1025                  # water density [kg m^-3]
d = 30                      # water depth [m]
L_fd = 2*L                  # total length fluid domain [m]

λ = 140                     # incident wave length [m]
k = 2*π / λ                 # wave number
ω = sqrt(g*k*tanh(k*d))     # dispersion relation
A_w = 0.75                  # amplitude of incident wave
```

```
φ_in(x) = (g*A_w/(1im*ω))*(cosh(k*x[2]) / cosh(k*d))*exp(1im*k*x[1])          # expression flow potential
u_in(x) = (g*A_w*k/ω)*(cosh(k*x[2]) / cosh(k*d))*exp(1im*k*x[1])             # expression flow velocity
η_in(x) = (g*A_w*k/ω^2)*(sinh(k*x[2]) / cosh(k*d))*exp(1im*k*x[1])           # expression of the surface
```

Domain

Next, the numerical domain is defined using the `Gridap` library, for which the different zones are specified. This includes the inlet damping zone, the free surface zone in front of the VLFS, the VLFS, the free surface zone behind the structure, and the outlet damping zone. For this tutorial, both damping zones, and the VLFS are set equal to L, while the free surface zones are equal to 1/2 L.

```
using Gridap
using Gridap.Geometry
using Gridap.CellData
using Gridap.FESpaces
```

```
Ld_in  = 1L                                                    # Inlet damping zone length
Lb     = L                                                     # VLFS length
Ld_out = 1L                                                    # Outlet damping zone length
LΓ = Ld_in+L_fd+Ld_out                                         # length fluid domain inc. damping zones
domain = (0,LΓ,0,d)                                            # fluid domain

x_in = Ld_in                                                    # x-coordinate end frontal damping zone
xb_o = Ld_in + 0.5(L_fd-L)                                      # x-coordinate start of VLFS
xb_1 = xb_o + Lb                                                # x-coordinate end of VLFS
xd = xb_1 + 0.5(L_fd-L)                                         # x-coordinate initial outlet damping zone poi
xj = [(xb_o + β*Lb), (xb_o + 2*β*Lb), (xb_o + 3*β*Lb)]          # x-coordinates that correspond with locations
```

Damping zone

The functions regarding the damping coefficients are defined with the expressions below, where the initial damping is set to $\mu_o = 10$.

```
μ_o = 10

μ_1(x::VectorValue) = μ_o* (1.0 - cos(π/2*(x[1]-xd)/Ld_out)) * (x[1] > xd) + μ_o*(1.0 - sin(π/2*x[1]/Ld_in)) *
μ_2(x::VectorValue) = -(μ_1(x)^2)/4

ηd = x -> μ_1(x)*η_in(x)*(x[1]<x_in)
φd = x -> μ_2(x)*φ_in(x)*(x[1]<x_in)
```

Construct the discrete model of the full domain

To construct the discrete model of the full domain, a partition is defined. The resolution of the horizontal axis should be high enough to obtain an accurate approximation of the propagating wave in x-direction. With respect to the vertical axis, the main interest is focused on the top layer of the fluid domain, near the surface; as the vertical velocity profile converts to zero at the bottom boundary. Therefore, a function is written to force an uneven distribution of the cell spaces in z-direction, such that the resolution is fine at the free surface and becomes coarser towards the bottom of the domain. For this tutorial, $nx = 80$ and $nz = 20$ are used regarding the partition in x-direction and z-direction, respectively.

Furthermore, to impose the conditions defined at the connections, it is important that the locations of the respective connections, xj, coincides with one the nodes of the finite elements. Hence, this is obtained by defining the distribution of the cells as a multiplication of connection location parameter β.

Accordingly, the discrete model of the fluid domain Ω is constructed using the function `CartesianDiscreteModel`. The function `simplexify` is used to change the mesh to an affine reference map, which is necessary to have the mapping work.

```
nx = 80
nz = 20
partition = (Int(4/β)*nx,nz)

function f_z(x)                # function to redistribute refinement of elements in z-direction
```

```
  if x == d
      return d
  end
  i = x / (d/nz)
  return d-d/(2^i)
end

map(x) = VectorValue(x[1], f_z(x[2]))
model_Ω=simplexify(CartesianDiscreteModel(domain,partition,map=map))
```

Boundaries

Now that the discrete fluid domain `model_Ω` has been constructed, the corresponding boundaries of the discrete domain are obtained. First, the initial boundaries of the fluid domain are mapped to their corresponding entity of the fluid domain and labeled using the function `add_tag_from_tags!`.

```
# Define surfaces that can be created without masks (only valid when using rectangular shape and a Cartesia
labels_Ω = get_face_labeling(model_Ω)
add_tag_from_tags!(labels_Ω,"surface",[3,4,6])   # assign the label "surface" to the entity 3,4 and 6 (top
add_tag_from_tags!(labels_Ω,"bottom",[1,2,5])    # assign the label "bottom" to the entity 1,2 and 5 (botto
add_tag_from_tags!(labels_Ω,"inlet",[7])         # assign the label "inlet" to the entity 7 (left side)
add_tag_from_tags!(labels_Ω,"outlet",[8])        # assign the label "outlet" to the entity 8 (right side)
add_tag_from_tags!(labels_Ω, "water", [9])       # assign the label "water" to the entity 9 (interior)
```

The different zones of the surface boundary are then defined using a `mask`. First, a mask is created for the complete surface boundary of the fluid domain, afterwhich a separated discrete model is created, i.e. `model_Γ`.

```
# Masks in Ω
# ==========
# From all the entities of dimension 1 in Ω (edges in the full domain),
# set to True all the edges that are in Γ and False otherwise.
Γ_mask_in_Ω = get_face_mask(labels_Ω,"surface",1)
# Create a list of indices that have value=True in the mask of active edges in Omega.
Γ_to_Ω_dim1 = findall(Γ_mask_in_Ω)

# Discrete model on the boundary (to construct a FE space only on the boundary Γ)
model_Γ = BoundaryDiscreteModel(Polytope{1},model_Ω,Γ_to_Ω_dim1)
```

Next, auxiliar functions are defined; to check if the elements are either located in one of the damping zones, at the free surface, within the structure, at the boundary of the structure, or at a connection.

```
# Auxiliar functions
# ==================
# Check if an element is inside the beam
function is_beam(coords)
    n = length(coords)
    x = (1/n)*sum(coords)
    (xb₀ <= x[1] <= xb₁ ) * ( x[2] ≈ d )
end

# Check if an element is inside the inlet damping zone
function is_inlet_damping(xs)
  # xs is a vector of points with the coordinates of a given element of dimension "d"
  n = length(xs) # number of points in each element (in an edge there will be two points)
  x = (1/n)*sum(xs) # take the average (centre of the element)
  (x[1] <= Ld_in ) * ( x[2] ≈ d ) # check if the centre is in the inlet damping zone and on the surface
end

# Check if an element is inside the outlet damping zone
function is_outlet_damping(xs)
  # xs is a vector of points with the coordinates of a given element of dimension "d"
  n = length(xs) # number of points in each element (in an edge there will be two points)
  x = (1/n)*sum(xs) # take the average (centre of the element)
  ( (LΓ - Ld_out) <= x[1] ) * ( x[2] ≈ d ) # check if the centre is in the inlet damping zone and on the su
end

# Check if an element is on the beam boundary
function is_beam_boundary(xs)
  is_on_xb₀ = [x[1]≈xb₀ for x in xs] # array of booleans of size the number of points in an element (for po
  is_on_xb₁ = [x[1]≈xb₁ for x in xs]
  element_on_xb₀ = minimum(is_on_xb₀) # Boolean with "true" if at least one entry is true, "false" otherwis
  element_on_xb₁ = minimum(is_on_xb₁)
  element_on_xb₀ | element_on_xb₁ # Return "true" if any of the two cases is true
end
```

```
# Check if an element is a joint
function is_a_joint(xs)
  is_on_xj = Array{Bool,1}(UndefInitializer(),length(xs))
  is_on_xj .= false
  for xi in xj
    is_on_xj = is_on_xj .| [x[1]≈xi for x in xs] # array of booleans of size the number of points in an ele
  end
  element_on_xj = minimum(is_on_xj) # Boolean with "true" if at least one entry is true, "false" otherwise.
  element_on_xj
end
```

The separated zones of the surface boundary are constructed, for which different masks are created with regard to the structure, the connection points, and the free surface. Accordingly, the entities that belong to the respective part of the surface boundary are identified and assigned to a new label.

```
# Masks in Γ
# ==========
labels_Γ = get_face_labeling(model_Γ) # get the face labeling of model_Γ
topo = get_grid_topology(model_Γ) # get the topology of model_Γ (the information about how the model is def
D = num_cell_dims(model_Γ) # spatial dimension of the model_Γ

# Construct the mask for the beam
entity_tag_beam = num_entities(labels_Γ) + 1 # create a new tag for the beam
for d in 0:D # loop over dimensions
  grid_Γ_dim_d = Grid(ReferenceFE{d},model_Γ) # construct a grid from the entities of dimension "d" in Γ
  coords_grid_Γ_dim_d = get_cell_coordinates(grid_Γ_dim_d) # get the coordinates of entities of dimension "
  beam_mask_in_grid_Γ_dim_d = lazy_map(is_beam,coords_grid_Γ_dim_d) # beam mask with the entities of dimens
  beam_boundary_mask_in_grid_Γ_dim_d = lazy_map(is_beam_boundary,coords_grid_Γ_dim_d) # beam boundary mask
  joint_mask_in_grid_Γ_dim_d = lazy_map(is_a_joint,coords_grid_Γ_dim_d) # joint mask with the entities of a
  # Create a list of indices that have value=True in the mask of active entities of dimension "d" in Gamma.
  beam_to_Γ_dim_d = findall( beam_mask_in_grid_Γ_dim_d .&
                             .!beam_boundary_mask_in_grid_Γ_dim_d .&
                             .!joint_mask_in_grid_Γ_dim_d)
  # Tag the faces of dimension "d" (all the faces indexed in beam_to_Γ_dim_d)
  for face in beam_to_Γ_dim_d
    labels_Γ.d_to_dface_to_entity[d+1][face] = entity_tag_beam
  end
end

# Add a name to the tag in labels_Γ
add_tag!(labels_Γ,"beam",[entity_tag_beam])


# Construct the mask for the joint
entity_tag_joint = entity_tag_beam + 1
# Here we don't loop because we'll only have entities of dimension 0 (points)
grid_Γ_dim_0 = Grid(ReferenceFE{0},model_Γ)
coords_grid_Γ_dim_0 = get_cell_coordinates(grid_Γ_dim_0)
joint_mask_in_grid_Γ_dim_0 = lazy_map(is_a_joint,coords_grid_Γ_dim_0)
# Create a list of indices of points in Γ that are joint
joint_to_Γ_dim_0 = findall( joint_mask_in_grid_Γ_dim_0)
# Tag the points (all the points indexed in joint_to_Γ_dim_0)
for point in joint_to_Γ_dim_0
  labels_Γ.d_to_dface_to_entity[1][point] = entity_tag_joint
end
# Add a name to the tag in labels_Γ
add_tag!(labels_Γ,"joint",[entity_tag_joint])
```

Next, the masks of edges in Ω, and the masks of points in Γ are obtained, which will be used to construct the triangulations for the floating structure, the free surface, and the set of internal points of the structure (skeleton).

```
# Mask of edges only in Ω
Γ_mask_in_Ω_dim_1 = get_face_mask(labels_Ω,"surface",1)        # get the mask of edges in Ω that are on Γ
Γ_to_Ω_dim_1 = findall(Γ_mask_in_Ω_dim_1)                      # Get indices of edges of Ω that are on Γ
Γstr_mask_in_Γ_dim_1 = get_face_mask(labels_Γ,"beam",1)        # get the mask of edges in Γ that are on th
Γstr_to_Γ_dim_1 = findall(Γstr_mask_in_Γ_dim_1)                # get indices of edges of Γ that are in the
Γfs_to_Γ_dim_1 = findall(!,Γstr_mask_in_Γ_dim_1)               # get indices of edges of Γ that are in the
Γstr_to_Ω_dim_1 = view(Γ_to_Ω_dim_1,Γstr_to_Γ_dim_1)           # get indices of edges of Ω that are in the
Γfs_to_Ω_dim_1 = view(Γ_to_Ω_dim_1,Γfs_to_Γ_dim_1)             # Idem for the free surface

# Mask of points only in Γ
Λb_mask_in_Γ_dim_0 = get_face_mask(labels_Γ,"beam",0)
Λj_mask_in_Γ_dim_0 = get_face_mask(labels_Γ,"joint",0)
```

Triangulations

Accordingly, the triangulations for the domain, the boundaries, and the interior points of the structure can be easily obtained

```
Ω = Triangulation(model_Ω) # triangulation of the full domain
Γ = Triangulation(model_Γ) # triangulation of the boundary (free_surface + beam)

# Now we can construct sub-triangulations
Γstr = BoundaryTriangulation(model_Ω,Γstr_to_Ω_dim_1)
Γfs = BoundaryTriangulation(model_Ω,Γfs_to_Ω_dim_1)
Γin = BoundaryTriangulation(model_Ω, tags = ["inlet"])

# Now construct a skeleton triangulation for the beam and joint
Λb = SkeletonTriangulation(model_Γ,Λb_mask_in_Γ_dim_0)
Λj = SkeletonTriangulation(model_Γ,Λj_mask_in_Γ_dim_0)
```

Quadratures

Finally, the quadratures are specified for the domain, the boundaries, and interior points of the structure

```
order = 2
dΩ = Measure(Ω,2*order)
dΓ_str = Measure(Γstr,2*order)
dΓ_fs = Measure(Γfs,2*order)
dΓ_in = Measure(Γin,2*order)
nΛb = get_normal_vector(Λb)
dΛb = Measure(Λb,2*order)
nΛj = get_normal_vector(Λj)
dΛj = Measure(Λj,2*order)
```

FE spaces

As the numerical domain, and the specific boundaries have been defined, the test spaces can be constructed. To this end, two spaces are built with regard to the internal domain `model_Ω` and the surface `model_Γ`, for which linear lagrangian shape functions are used as reference element. Subsequently, the trial spaces are obtained from the test spaces. The separated spaces are then combined for the full numerical domain using the function `MultiFieldFESpace`.

```
reffe = ReferenceFE(lagrangian,Float64,order)
  V_Ω = TestFESpace(model_Ω,reffe, vector_type=Vector{ComplexF64}  )
  V_Γ = TestFESpace(model_Γ,reffe, vector_type=Vector{ComplexF64}  )
  U_Ω = TrialFESpace(V_Ω)
  U_Γ = TrialFESpace(V_Γ)
  Y = MultiFieldFESpace([V_Ω,V_Γ])
  X = MultiFieldFESpace([U_Ω,U_Γ])
```

Weak form & CG/DG approach

The final step to solve the FSI problem with Gridap is to obtain the bilinear form of the mathematical formulation, $a((\phi,\eta),(w,v))$ (see below). The bilinear form contains both first, and second order derivatives. The finite element spaces therefore require continuous gradients between elements, i.e. C1 continuity across elements. As proposed by Colomés et al., this can be achieved by applying the Continuous Galerkin / Discontinuous Galerkin (CG/DG) approach for fourth order operators, where the discrete functions are continuous at the element nodes, but the gradient is discontinuous. Therefore, linear Lagrangian elements can be applied, while continuity of the gradient over adjacent elements is weakly enforced by means of an interior penalty approach.

To obtain the bilinear form, the following steps are applied:

- The first row is obtained by multiplying the Laplace equation by the test function, w, after which it is integrated over the domain Ω and then integrated by parts.
- The normal velocity at the boundaries is replaced by the respective kinematic boundary condition of the free surface Γ_{fs}, see second row, where the conditions at the seabed Γ_b, and the vertical boundary Γ_R are canceled out as they go to zero.
- The third row includes the dynamic boundary condition on the free surface. According to the monolithic approach described by Akkerman et al., here the dynamic condition is multiplied by

a modified test function, $v + \alpha_{fs} w$, and integrating over the free surface boundary Γ_{fs}, where the term $\alpha_{fs} w$ is added to the test function v to guarantee coercivity of the system.

- The fourth row includes the dynamic boundary condition on the beam surface, multiplied by test function v, integrated over the fluid-structure interface Γ_{str}. In this case, however, the fourth order term is integrated by parts twice, where the resulting integrals over the structure boundaries are canceled out again, as it was assumed that the conditions at the free ends of the VLFS are equal to zero.
- Implementing the interior penalty approach in a similar way as discussed in the Gridap tutorial Poisson equation (with DG), the third, and second last row weakly forces continuity of the surface elevation gradients between structural elements.
- Ultimately, the approach to weakly force conditions between adjacent elements is also used to impose the interface condition regarding the bending moment at the connections, as can be seen in the final row.

weak form

Hence, the complete bilinear form is described below, where the linear form involves the boundary conditions which are defined by the known expressions for ϕ_{inc}, and η_{inc}.

```
const h = β*Lb/nx
const γ_m = 1.0e2*order*(order+1)
const αh = -1im
const βh_fs = 0.5
αh_fs = αh*ω/g*(1-βh_fs)/βh_fs
```

```
a((φ,η),(w,v)) =      ∫(  ∇(w)⋅∇(φ) )dΩ   +
                      ∫(  (1im*ω*w*η)  - μ₁*η*w - μ₂*φ*w/g )dΓ_fs   +
                      ∫(  βh_fs*(v + αh_fs*w)*g*η  +   βh_fs*(-1im*ω)*(v + αh_fs*w)*φ )dΓ_fs   +
                      ∫(  (-ω^2*α1_b + g)*v*η +  Δ(v)*(α2_b*Δ(η)) +  (-1im*ω*v*φ)   +   (1im*ω*w*η)  )dΓ_st
                      ∫(   - (jump(∇(v)⋅nΛb) * mean(α2_b*Δ(η))) - (mean(Δ(v)) * jump(α2_b*∇(η)⋅nΛb))  +
                          γ_m/h*( jump(∇(v)⋅nΛb) * jump(α2_b*∇(η)⋅nΛb))  )dΛb +
                      ∫(  (1/ρ_w)*(jump(∇(v)⋅nΛj) * k_r * jump(∇(η)⋅nΛj)) )dΛj


l((w,v)) =            ∫( w*u_in )dΓ_in - ∫( w*ηd + w*φd/g )dΓ_fs
```

Solver

Ultimately, with the function `AffineFEOperator`, the equations are assembled into a matrix, where the numerical solver `Gridap.solve` is used to find the approximated solution for `φh`, and `ηh`.

The bending moment of the VLFS is defined by the second derivative of the displacement with respect to x, multiplied by the bending stiffness EI. Accordingly, the moment distribution along the structure can be obtained from the solution for `ηh`; using `interpolate_everywhere` over the surface boundary, `V_Γ`.

```
op = AffineFEOperator(a, l, X, Y)

φh , ηh = Gridap.solve(op)
Moment = interpolate_everywhere(EI_b*Δ(ηh),V_Γ)
```

Visualisation

The results can be inspected by writing it into a `vtk file`, which will generate a file that contains the real and imaginay part of the problem solutions.

```
writevtk(Ω, "FSI_multiVLFS_phi", cellfields=["phi_re"=>real(φh), "phi_im"=>imag(φh)])
writevtk(Γ, "FSI_multiVLFS_eta", cellfields=["eta_re"=>real(ηh), "eta_im"=>imag(ηh)])
writevtk(Γ, "FSI_multiVLFS_moment_distribution", cellfields=["M_re"=>real(Moment), "M_im"=>imag(Moment)])
```

© Oriol Colomés. Last modified: October 21, 2021. Website built with Franklin.jl and the Julia programming language.